The Thermodynamics of Information in Nanoscale Systems

Jonathan Dexter
St. Catherine's College
University of Oxford

A thesis submitted for the degree of
Doctor of Philosophy
Michaelmas 2025

Acknowledgements

The work presented in this thesis could not have been completed without the help, support, and encouragement of many people. My primary thanks go to my supervisors, Natalia Ares and Andrew Briggs. My thanks go to Natalia for her support and guidance during my research as well as providing me with access to excellent laboratory facilities, without which the research presented here would not have been possible. I am grateful to Andrew for his continued encouragement, invaluable insight, and for his thoughtful questioning, which always helped to clarify my thinking.

Outside of Oxford, I would especially like to thank Mark Mitchison of King's College London and Gerard Milburn of the University or Sussex for being incredibly generous with their time in answering my questions and providing thoughtful guidance on theoretical matters.

The research presented here has also been made possible by the support of outstanding colleagues, both within the Oxford group and beyond. In particular, I would like to thank Yikai Yang for his help with device fabrication and the experimental work of Chapters 4 and 5. I am also indebted to Joseph Hickie, without whose expertise and dedication the work in Chapter 4 could not have been achieved. From the University of Exeter, I would like to thank Federico Cerisola and Joe Dunlop for their invaluable theoretical contributions to Chapter 4.

I am grateful to the members of the FQXi consortium: Juliette Monsel, Joe Dunlop, Sofia Sevitz, Lea Bresque, Jorge Tabanera, Alexia Auffèves, Juan Parrondo, and Janet Anders for insightful discussion and useful theoretical contributions. I also wish to acknowledge Georgios Katsaros of the Institute of Science and Technology Austria for generously providing the device used in Chapter 4.

More broadly, it has been a privilege to work among the talented researchers, past and present, of the Natalia Ares group. I would particularly like to thank Pranav Vaidhyanathan for being an excellent travel companion, brilliant host, and a constant source of American optimism. I am also grateful to the following group members for their friendship, scientific insight, and support: Kushagra Aggarwal, Cornelius Carlsson, David Craig, Federico Fedele, Path Girdhar, Sonali Goel, Prasanta Kumbhakar, Vincent Michal, Sebastian Orbell, Marek Rychetsky, Jonas Schuff, Brandon Severin, Lucas Schorling, Nico Alvez, Barnaby van Straaten, Vivek Wadhia.

Lastly, I would like to thank my family and friends. To my London friends, Paul, Chris, Tom, and Iittu, I am always grateful for their friendship and for always providing me with a place to stay whenever I was in town. During my time in Oxford I have met many wonderful and interesting people, but I would particularly like to thank Mia, Max and Alice for making it a time I will look back on with great fondness. To my family, my brother, my dad, and Irene, thank you for your encouragement and belief in me. And last of all, to my mum, who may not have been able to read this, but who I'm certain would have been proud of my achievement.

Abstract

The study of nanoscale systems opens up exciting new opportunities for exploring the fundamental limits of thermodynamics. Recent theoretical and experimental progress has considerably advanced our understanding of the thermodynamics of small systems. In this thesis I build on this work by using semiconducting quantum dots (QD) devices to examine the nanoscale thermodynamics of two fundamental physical processes: timekeeping and information processing. The primary contribution of this thesis is an investigation of the thermodynamics of information erasure in a QD defined in a Ge/SiGe heterostructure. Landauer's principle sets a fundamental lower bound on the energy required to erase a single bit of information, achieved only in the quasistatic limit and in the context of a single thermal reservoir. I show that this bound can be approached in the QD system in the absence of an applied bias and when the erasure process is carried out sufficiently slowly. I then go on to investigate how the cost of erasure is modified as the idealised constraints (quasistatic driving and a single thermal reservoir) underlying Landauer's bound are relaxed. My results reveal that under finite-time driving and in the presence of an applied bias, intrinsic properties of the system, such as spin degeneracy and tunnelling rates, introduce asymmetries in the work required to erase to logical one versus logical zero. This work is the first experimental investigation of the thermodynamics of information erasure in a multi-reservoir system. Given that transistors, the fundamental building blocks of modern information-processing technology, require a bias to operate, this represents an important step toward understanding the thermodynamic limits of real-world information processing devices. This thesis also makes progress towards the realisation of a platform to study the thermodynamics of timekeeping in a nanoelectromechanical device. Like all physical processes, timekeeping is governed by thermodynamic constraints. Recent theoretical work has shown how the accuracy with which we are able to measure time can only be increased at the expense of greater entropy production. I focus on a device comprising of a QD defined within a suspended carbon nanotube (CNT). The QD-CNT system functions as a clock, with the mechanical oscillations of the CNT generating ticks. Single-electron transport through the QD enables readout of these ticks whilst simultaneously exerting a back-action force on the CNT, giving rise to self-sustained oscillations. The result is a fully autonomous nanomechanical clock driven, in part, by quantum noise. I experimentally characterise this system, develop a theoretical analysis of the measured signal that accounts for the amplifier chain coupled to the clock, and establish an experimental framework that enables measurement of the entropy production as a function of the clock's accuracy. My work paves the way for future experiments by providing a clear methodology for the first experimental investigation of the thermodynamics of a fully autonomous nanomechanical clock.

Table of Contents

List of Abbreviations

CIM constant interaction model.

CNT carbon nanotube.

CNTQD carbon nanotube quantum dot.

CVD chemical vapour deposition.

DUT device under test.

EBL electron beam lithography.

i.i.d independent and identically distributed.

JE Jarzynski equality.

LB Landauer bound.

LE Landauer erasure.

MLE maximum likelihood estimation.

PCB printed circuit board.

QD quantum dot.

QOR quantum of resistance.

SEM scanning electron microscope.

SHO simple harmonic oscillator.

SNR signal to noise raito.

SQL standard quantum limit.

SQUID super conducting quantum interference device.

WTD waiting time distribution.

1

Introduction and Overview

The theory of thermodynamics stands as one of the supreme achievements of the scientific endeavour. From its humble origins during the industrial revolution, when the first glimpse of the theory was provided by engineers seeking to understand the factors limiting the efficiency of steam engines, the scope of thermodynamics has expanded considerably, now finding applications across physics, chemistry, biology and beyond. The second law, which states that the entropy of a closed system can never decrease, provides a breadth of explanatory power that far exceeds our most powerful physical theories. Whereas the theories of quantum mechanics and general relativity are restricted to their respective domains, the second law applies equally at the largest and smallest scales, governing the collective behaviour of subatomic particles, the evolution of galaxies and everything in between. Despite its enormous success, thermodynamics remains an enigmatic theory. The dynamical laws governing the microscopic constituents of matter are time-reversal symmetric, yet the second law is time-reversal asymmetric: entropy always increases into the future. The question of how, in a world governed by time-symmetric microscopic laws, the time-asymmetric laws of thermodynamics emerge remains a topic of debate for physicists and philosophers alike [19]. Insight has recently come from extending the theory's scope. Thermodynamics is traditionally a theory of systems with vast number of degrees of freedom (a gas in a box being the canonical example); however, in the past few decades thermodynamics has been extended to encompass systems with only a few degrees of freedom [58]. In such small systems, fluctuations play a significant role and violations of the second law are possible [16, 22, 58].

The two processes studied in this thesis, information processing and timekeeping, are of fundamental importance to our everyday lives. Like all physical processes they are governed by the laws of thermodynamics, and it has been shown that the efficiency with which we are able to process information and the accuracy that we can keep time are limited by the second law [71, 79]. The work detailed in this thesis uses semiconducting nanoscale devices to probe the thermodynamics of these two processes. Typically, a device is classified as nanoscale if its dimensions lie between 1 nm and 1 μm. Devices at this scale may also be referred to a mesoscopic. Meso is the Greek word for 'in the middle', emphasising the fact that these devices operate in an intermediate regime between the atomic, where quantum mechanics dominates, and the macroscopic, where classical physics applies. The devices used in this thesis, a Ge/SiGe heterostructure and a suspended carbon nanotube (CNT), lie firmly within this regime. The semiconducting nature of these devices combined with their small size allows for the formation of quantum dots, which, as we shall see, play an integral part in the experimental realisation of the small, controllable systems necessary for the study of thermodynamics at this scale.

Chapter 2 describes the thermodynamic background relevant to the experiments presented later in the thesis, with particular emphasis on the thermodynamics of information processing and on the thermodynamics of clocks and timekeeping. In Chapter 3, the experimental methods used in this thesis are described. The chapter begins with an overview of single-electron transport through quantum dots, followed by a description of the experimental devices and the techniques used to manipulate and measure them. An account of the fabrication process for CNT devices is also included (with detailed recipes provided in the Appendix). In Chapter 4, a Ge/SiGe device is used to study the thermodynamics of information erasure. A single bit of information is encoded in the charge occupancy of a single quantum dot (QD) and the work cost associated with erasing this information measured. Traditionally, erasure has been studied in systems coupled to a single thermodynamic reservoir. In this study, the effect of adding a second reservoir is investigated, representing an advance on previous experimental work. In Chapter 5, the focus shifts to the thermodynamics of timekeeping, with a suspended CNT device proposed as a novel experimental platform. The system is characterised, and a framework is developed for extracting metrics of the clock's performance from measured signals, accounting for noise introduced by the measurement chain. This chapter lays the groundwork for a full experimental realisation in future work. Finally, Chapter 6 summarises the work presented.

2

Thermodynamic Background

Contents

Originally developed to optimise the efficiency of steam engines, thermodynamics was conceived as a macroscopic theory to describe the collective behaviour of systems with vast numbers of degrees of freedom [6]. It is only recently, however, that theoretical and experimental advances have allowed for a more detailed understanding of the thermodynamics of microscopic systems [58]. In this chapter, we provide a brief overview of the thermodynamic background relevant to the experiments presented in Chapters 4 and 5.

2.1 Stochastic Thermodynamics

To illustrate how the thermodynamics of microscopic systems can differ from that of macroscopic systems, consider the example, taken from Ref. [58], of a gas in a cylinder with a piston. The system is macroscopic such that the gas contains of order $N \sim 10^{23}$ particles. We imagine quickly pushing the piston into the cylinder and compressing the gas. If this process is carried out adiabatically the internal energy of the gas will increase. The first law then gives

$$W > 0, \tag{2.1}$$

where W is the work done by the piston on the gas. This inequality is not mandated by the underlying dynamics, there exist physically viable N-particle trajectories for which $W < 0$. However, for a macroscopic number of particles, the chances of observing these trajectories is vanishingly small. By contrast, for a gas consisting of only a few particles, although Eq. 2.1 holds on average the chance of observing a trajectory for which $W < 0$ is no longer negligible. The above example illustrates how, as the size of a system is reduced, fluctuations become increasingly important. It is temping to dismiss these fluctuations as noise; however, one of the key results of stochastic thermodynamics is that fluctuations associated with the response of a system driven away from equilibrium encode information concerning the equilibrium states of the system [58].

To make this distinction between macroscopic and microscopic thermodynamics more explicit consider a system with a discrete set of microstates each with energy E_i. The Gibbs entropy of the system is given by

$$S_G(t) = -k_B \sum_i p_i(t) \ln p_i(t), \tag{2.2}$$

where $p_i(t)$ is the probability of observing the system in the ith microstate at time t. The Gibbs entropy is a property of the ensemble of microstates that can be adopted by the system. It quantifies our uncertainty concerning which microstate the system is adopting at a given time. Now consider the expression

$$\Delta s_{\text{tot}} = k_B \ln \frac{p[\Gamma]}{\tilde{p}[\tilde{\Gamma}]}, \tag{2.3}$$

where Γ is the trajectory taken by a system as it undergoes some kind of spontaneous or driven evolution and $\tilde{\Gamma}$ its time reversed counterpart. $p[\Gamma]$ and $\tilde{p}[\tilde{\Gamma}]$ are then the probabilities of observing these two trajectories. The quantity Δs_{tot} is known as the stochastic entropy production, and, in contrast to the Gibbs entropy, it is a property of an individual trajectory taken by the system rather than an ensemble of microstates. The stochastic entropy production can be shown to satisfy

$$\langle e^{-\Delta s_{\text{tot}}/k_B} \rangle = 1, \tag{2.4}$$

known as the integral fluctuation theorem [104], from which it follows that

$$\langle \Delta s_{\text{tot}} \rangle \geq 0, \tag{2.5}$$

an expression of the second law. The stochastic entropy production is interpreted as being the total entropy production associated with the trajectory Γ. Macroscopically, the second law tells us that the total entropy always increases; however, Eq. 2.3 can be negative. Taken together Eqs. 2.3 and 2.5 show that at the second law can be violated for individual trajectories of a system but never on average.

Equation 2.4 recasts a thermodynamic inequality (the second law) as an equality. A further example of this inequality to equality transformation is provided by the Jarzynski equality (JE) [57]. Consider performing work on a system by manipulating some externally controlled parameter according to a set protocol. If the initial and final states of the system are in equilibrium with an environment at temperature T the work performed during this process is bound by the inequality

$$W \geq \Delta F, \tag{2.6}$$

where ΔF is the change in free energy between the initial and final states of the system. The JE translates this inequality into the equality

$$\left\langle e^{-W/k_B T} \right\rangle = e^{-\Delta F/k_B T}, \tag{2.7}$$

where T is the initial temperature of the system and the average is over all possible realisations of the protocol. As long as the system is initially prepared in equilibrium, the JE holds regardless of how far the system is driven from equilibrium and for arbitrary driving protocols. Its significance lies in the fact that equilibrium free energy changes of a system can be recovered from measurements of non-equilibrium work.

Equations 2.4 and 2.7 are examples of *fluctuation theorems* [26, 39, 45, 56, 57], a set of relations concerned with the statistical fluctuations of quantities associated with thermodynamic processes [104]. As well as constraining these fluctuations to satisfy specific requirements, and providing some of the few analytical expressions with which to describe non-equilibrium systems [101], fluctuation theorems also shed light on the longstanding conceptual puzzle at the heart of thermodynamics: the emergence of an arrow of time in a theory whose underlying dynamics are time-reversal symmetric [18]. Light is shed on this paradox, which has been debated since the time of Boltzmann and Loschmidt [19], by showing that time-reversed trajectories do occur, but that their probability becomes vanishingly small for macroscopic systems.

This work details the experimental realisation of systems whose size is small enough for fluctuations to become important. In particular, we will be examining the thermodynamics of information processing in a nanoscale system where macroscopic bounds on the work cost required to erase information can be broken. We therefore take as our next topic the thermodynamics of information.

2.2 The Thermodynamics of Information

In 1961 Rolf Landauer showed that the logical irreversible manipulation of information is a dissipative process. In particular, he showed that the logically irreversible RESET TO ONE operation is necessarily accompanied by the dissipation of at least $k_BT\ln 2$ of heat, where k_B is Boltzmann's constant and T the temperature of the environment into which the heat is dissipated [71]. The process of performing RESET TO ONE (or equivalently RESET TO ZERO) so as to dissipate the minimum possible heat has come to be known as Landauer erasure (LE), and $k_B T \ln 2$ the Landauer bound (LB). Landauer's work demonstrated a profound connection between the two previously unconnected disciplines of information theory and thermodynamics. Landauer showed that information is physical [72], and in doing so demonstrated that the processing and manipulation of information are governed by the laws of physics.

An understanding of the concept of information is often taken for granted in discussions of Landauer's work. However, its definition is subtle with confusions often arising in the literature [2]. Before we examine Landauer's result, we therefore briefly discuss the concept of information in a more general sense.

Consider a system consisting of a particle in a partitioned box. In the context of LE it is important that we quantify how much information is contained within this system. In understanding what it means for a system to contain information, it is important to realise that information is not an intrinsic property of the system, it is subjective, depending on the observer's state of knowledge of the system [2]. The concept of Shannon entropy provides a quantitative way to formalise this idea. It is defined as

$$H(X) = -\sum_{i=1}^{N} p_i \log p_i, \tag{2.8}$$

where X is a random variable that can take N possible values, each occurring with probability p_i. The Shannon entropy quantifies our uncertainty about the state of a system. It tells us how much it is possible to know about the system and can be interpreted as a measure of 'potential information' [2]. If nothing is known about the state of the system we assume all states are equally likely, our uncertainty is maximised and Eq. 2.8 becomes

$$H_{\max}(X) = \log N. \tag{2.9}$$

When the logarithm is taken to base 2, the Shannon entropy is measured in bits. For a system with two states, such as the partitioned box, the maximum uncertainty is therefore 1 bit. Conversely, if we are certain of the state of the system, our uncertainty is minimised and the Shannon entropy reduces to zero. If the Shannon entropy quantifies our uncertainty regarding the state of a system, information quantifies how much we know about the state of a system. Consider the following expression, which defines the information content of a random variable X [2]

$$I(X) = H_{\max} - H(X). \tag{2.10}$$

Intuitively, this expression makes sense: as our uncertainty regarding the state of a system decreases from its maximum value, our information about the system increases. When we know nothing about the state of the system we have $H(X) = H_{\max}$ giving $I(X) = 0$. We can only learn more about the system, and from our perspective the amount of information contained within the system is then maximised. On the other hand, when we are certain of the state of the system we have $H(X) = 0$ giving $I(X) = H_{\max}$. We cannot learn anything further about the system, meaning, from our perspective, its information content is zero. To erase information contained in a system we must therefore reduce our uncertainty regarding its state. This reduction in uncertainty is accompanied by a gain of information regarding the state of the system. The information gained is not, however, the information initially stored in the system. This information is irreversibly lost in the erasure process.

To see why this is the case we proceed by examining a physical realisation of the RESET TO ONE (ZERO) operation. We take as our starting point the partitioned box and particle system described above. We encode information in the system by associating the particle being in the left and right hand sides of the box with logical zero and logical one respectively. A piston is added to the right hand side of the box and the whole system is coupled to an environment with temperature T. Initially, no information is available concerning the location of the particle such that one bit of information is encoded in the system. Erasure proceeds by removing the partition then quasistatically compressing the piston, forcing the particle to the left hand side of the box. The partition is then reinserted, trapping the particle in the left hand side of the box. The idea is illustrated in Fig. 2.1. Crucially, the particle ends up in the left hand side of the box regardless of which side it initially occupied making the process is logically irreversible. At the

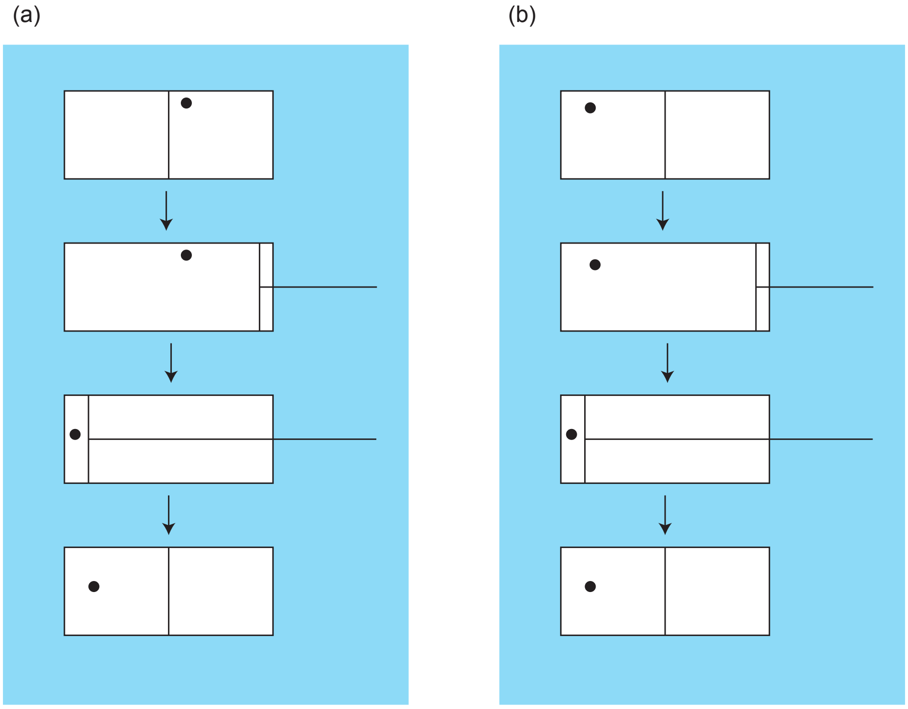

Figure 2.1: Schematic representation of LE. (a) The particle is initiated in the right hand side of the box, the partition is removed and the piston quasistatically pushes the particle to the left hand side of the box. The partition is then reinserted trapping the particle in the left hand side of the box. (b) Same as (a), but now the particle is initiated in the left hand side of the box. The final state of the system is the same as (a), demonstrating that the erasure process results in the same final state regardless of the unital state of the system.

end of the process we know the location of the particle with complete certainty, and the information initially encoded in the system has been erased.

We can use simple thermodynamic arguments to compute the work cost associated with this process. We assume that the energy of the system is the same regardless of which side of the box the particle is located. The internal energy of the system at the conclusion of the erasure process is then equal to its initial value. The first law then allows us to write

$$\Delta W = -\Delta Q = -T\Delta S, \tag{2.11}$$

where ΔW is the work done on the system and ΔS is the change in entropy of the system. Using the expression for Gibbs entropy given by Eq. 2.2 we have

$$\Delta S = S_f - S_i = -k_B \ln 2, \tag{2.12}$$

where S_i and S_f are the initial and final entropies of the system. We therefore have

$$\Delta W = k_B T \ln 2. \tag{2.13}$$

Since the erasure process is carried out quasistatically, this is the minium amount of work required to perform the protocol and erase a bit of information. From Eq. 2.11 we see that this work is accompanied by an equivalent amount of heat dissipated into the environment. We can now understand what has happened to the information initially encoded in the system. As heat is dissipated into the environment, information concerning the position of the particle is dispersed amongst the vast number of environmental degrees of freedom. In principle, an all-knowing entity who could time-reverse the combined box-environment system could establish the initial location of the particle once erasure has concluded; however, the impracticability of such a scheme means that the information initially stored in the box is irretrievably lost.

Landauer's work shows how thermodynamics constrains the manipulation of information. In the next section, we see how thermodynamics constrains a similarly fundamental physical process: timekeeping.

2.3 The Thermodynamics of Clocks and Timekeeping

The ability to keep time is an essential part of every day life. Clocks, the tools that allow us to do this, are physical systems and, as such, are bound by the laws of physics. As well as being relied upon by all of us to carry out our daily lives, clocks, as both practical instruments and as conceptual elements in physical theories, are of fundamental importance to the physical sciences. Understanding their physical limitations is therefore a problem of deep significance. Much work has been achieved in this regard, particularly in relation to the thermodynamics of timekeeping [28,38,77,79,86,117] . In this section we will briefly review the main results of this work.

We begin by answering the seemingly simple question: what is a clock? One answer to this question might be simply that a clock is a device for measuring time. However, this just kicks the can down the road. We now need to answer the question: what is time? Rather than attempting to resolve a question that has puzzled scientists and philosophers for thousands of years [37], we follow Ref. [79] and define a clock as “a physical device used to coordinate local coincidences of physical events”. An alternative way of stating this definition is that clocks are devices that enable us to keep appointments. For example, consider a case where Bob has agreed to meet Alice at the train station when her train arrives at 2 pm. In order to achieve this Bob, who is in possession of a clock, adjusts his location in order to ensure that his arrival on the platform and his clock reading 2 pm happen simultaneously. In other words he has adjusted his location in order to coordinate a local coincidence of a specific state of his clock with the arrival of Alice’s train. Of course, the meeting could only take place if Alice and the train operator were also in possession of clocks. This highlights an often overlooked aspect of clocks and timekeeping, namely, that the act of keeping time is relational. A single clock is only useful to the extent that its readings can be synchronised and compared with other clocks [5].

In the above example, in order for Bob to successfully meet Alice at the station, it is important that the clocks carried by all parties are accurate. Intuitively, we tend to think of an accurate clock as one that allows us to keep appointments. We can make this intuition more precise by adopting the following definition for the accuracy N of a ticking clock [28, 38, 86]

$$N = \frac{\mu^2}{\sigma^2}, \tag{2.14}$$

where μ is the average time between ticks of the clock, and σ is the standard deviation of this interval. The expression for N represents the expected number of ticks that occur before the clock's reading is off by one tick. To see this we model the waiting time between ticks of the clocks as a random variable with mean μ and standard deviation σ. In simple models of ticking clocks it is generally assumed that the waiting times between ticks are independent and identically distributed (i.i.d) [28]. If the time between the ith and $(i+1)$th tick is τ_i, then after n ticks a total time $t_n = \sum_i^n \tau_i$ has elapsed. The mean and standard deviation of this interval are $\mathbb{E}[t_n] = n\mu$ and $\Delta t_n = \sqrt{n}\sigma$ respectively, where the expression Δt_n follows from the i.i.d assumption. The clock is off by one tick when the typical timing error is equal to the average time between ticks. In our notation this gives $\Delta t_n = \mu$, from which we obtain the expression for the accuracy given by Eq. 2.14. In positing this definition, we are implicitly assuming the existence of a secondary clock whose accuracy is far greater than that of the clock whose accuracy we wish to quantify, an example of the relational nature of timekeeping.

It is tempting to think that any time dependent dynamical system can function as a clock. However, this is not the case; for a clock to be of practical use it must continually provide a time reference to an external observer [38]. This leads to the concept of clocks as bipartite systems consisting of two distinct parts: a clockwork and a register [28, 38, 90, 123]. The clockwork is a non-equilibrium system whose dynamics are dictated by the passage of time, while the register stores information concerning the evolution of the clockwork, providing the external time reference. Ideally, the mechanism by which information is transferred from the clockwork to the register should not affect the dynamics of the clockwork [123]. For a classical system this is typically achievable.

However, a measurement of a quantum system necessarily disturbs its state, placing fundamental limits on the accuracy of quantum clocks [90].

Thermodynamically, a clock is an irreversible system pushed away from equilibrium. A clock seeks to establish equilibrium with its environment with the resulting dynamics used to mark the passage of time. Once a clock has established equilibrium its state becomes independent of time and it is no longer useful. Therefore, in order to ensure a clock continually provides a time reference, it must have access to a supply of free energy given by

$$\Delta F = \Delta U - T\Delta S, \tag{2.15}$$

where ΔU is a change in the internal energy of the clock, ΔS a change in its entropy and T the temperature of the environment to which it is coupled. Eq. 2.15 shows that there are two ways to drive a clock: by performing work on it to increase its internal energy, or by performing measurements to decrease its entropy. An example of the first is provided by a pendulum clock with a falling mass, where an escapement mechanism delivers a continual series of kicks to the pendulum preventing it from coming to rest [79]. An example of the second is the thermal clock discussed in Ref. [86], where the normal mode of a membrane, excited by thermal fluctuations in the environment, is continuously measured to extract a signal that can be used to mark the passage of time.

The process of a system attempting to establish equilibrium with its environment is necessarily accompanied by a dissipation of heat into the environment [52, 99]. The operation of a clock is therefore associated with the production of entropy. Indeed, for a clock the production of entropy is essential to ensure that forward transitions of the clockwork are biased in favour reverse transitions - we do not want our clocks to tick backwards [38]. A number of theoretical [28, 38, 77, 79] and experimental [86, 117] studies have related the entropy production associated with a clock's operation with its accuracy. A consistent outcome of these studies is that increasing the accuracy of a clock can only be achieved at the expense of increased entropy production. Unlike the case of information erasure detailed above, no relation currently exists to quantify this relationship in general terms. However, the idea that increased accuracy requires increased entropy production has become a well established principle in the study of the thermodynamics of clocks and timekeeping.

3

Experimental Methods

Contents

In this chapter we provide an outline of the methods used to perform the experiments detailed in chapters 4 and 5 of this work. We begin with a general theoretical overview of electron transport through QDs before proceeding with a description of the devices used in the work: a Ge/SiGe heterostructure and a suspended CNT device. This is followed by a discussion of the techniques used to perform the measurements presented in this thesis. Finally, we give a detailed description of the fabrication process used to create suspended CNT devices.

3.1 Quantum Dots

The experiments described in this work utilise the transport properties of electrostatically defined QDs to investigate the thermodynamics of timekeeping and information erasure at the nanoscale. Specifically, the thermodynamics of timekeeping is studied in a one dimensional CNT system, where use is made of the coupling between the the mechanical motion of the CNT and single electron transport through a QD defined along its length. Information erasure, on the other hand, is studied in a Ge/SiGe heterostructure device in which a QD is formed through the electrostatic confinement of a two-dimensional hole gas (2DHG). In this section we provide a brief overview of QDs and their transport properties in a general, device-independent way. In Section 3.1.5, we present more detailed overviews of the QDs in the specific platforms used in this work.

3.1.1 Single quantum dots

Fig. 3.1 shows a typical energy space representation of a single QD. A QD with electrochemical potential μ is coupled to source and drain electrodes with electrochemical potentials μ_S and μ_D. We define the difference between source and drain electrochemical

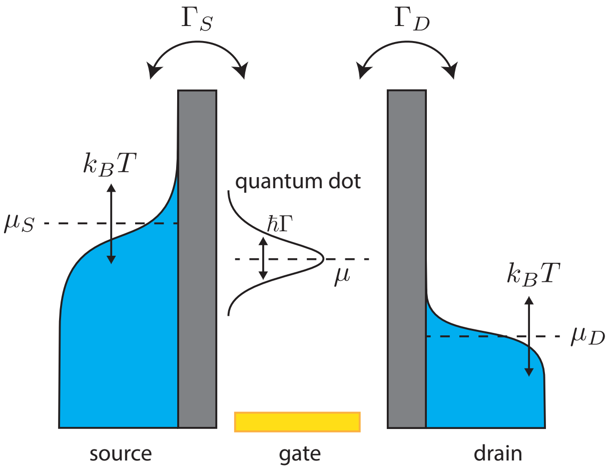

Figure 3.1: Energy space schematic of a single QD with electrochemical potential μ. The dot is coupled to source and drain electrodes with electrochemical potentials μ_S and μ_D and temperature T. The dot exchanges electrons with the source and drain at rates Γ_S and Γ_D. Broadening of the dot level due to coupling to the leads is characterized by a width $\hbar\Gamma$, where $\Gamma = \Gamma_S + \Gamma_D$.

potentials $\Delta\mu_{S,D} = \mu_S - \mu_D$. The electrochemical potential of the dot can be manipulated by applying a voltage, V_G, to a gate electrode. The source and drain electrodes serve as electron reservoirs with electronic occupation given by the Fermi-Dirac distribution

$$f_{S,D}(E) = \frac{1}{1 + e^{(E-\mu_{S,D})/k_BT}}, \tag{3.1}$$

where k_B is Boltzmann's constant and T the temperature of the electrons of the reservoir. It is assumed for the remainder of this work that the temperatures of the source and drain electrodes are equal. The dot exchanges electrons with the source and drain electrodes. The rate at which this exchange occurs is dictated by the strength of the coupling between the dot and the electrodes, which, in turn, is quantified by the intrinsic tunnelling rates Γ_S and Γ_D. The coupling of the QD to the source and drain electrodes causes a broadening of the energy level of the dot whose origin can be traced to the energy-time uncertainty relation. The broadening is characterised by a width $\hbar\Gamma$, where $\Gamma = \Gamma_S + \Gamma_D$ [109]. A QD for which $k_BT \gg \hbar\Gamma$ is said to be thermally broadened, and the effects of lifetime broadening can be ignored when studying transport through the dot. Conversely, when $\hbar\Gamma \gg k_BT$ the dot is said to be lifetime broadened and the effects of lifetime broadening must be taken into account.

An important quantity in the characterisation of QDs is the charging energy given by

$$E_C = \frac{e^2}{2C}, \tag{3.2}$$

where C is the total capacitance of the dot. The charging energy is an entirely classical concept and quantifies the energetic cost of adding an additional electron to the dot in the presence of Coulomb repulsion. Specifically, the energy required to add the Nth electron given by [83]

$$E_{N\text{th}} = E_C(2N-1). \tag{3.3}$$

A necessary condition for the formation of a QD is

$$E_C \gg k_B T, \hbar\Gamma. \tag{3.4}$$

Eq. 3.4 ensures that thermal fluctuations do not cause random transitions of electrons between the source and drain and that the broadening of the dot's energy level is small enough to ensure that individual energy levels are well separated. A further restriction on the formation of a QD can be derived by considering the energy-time uncertainty relation

$$\Delta t \Delta E > h. \tag{3.5}$$

Charging a dot with capacitance C takes a time $\Delta t = RC$, where R is the tunnelling resistance of the dot. If we wish to resolve the charging energy of the dot we have

$$RC\frac{e^2}{2C} > h, \tag{3.6}$$

which leads to the condition

$$R > \frac{h}{e^2}, \tag{3.7}$$

which implies that in order to resolve discrete charging events the resistance of the tunnel barriers should be greater than the quantum of resistance (QOR) h/e^2.

Given that the capacitance of a QD scales with its physical size, the inequality of Eq.

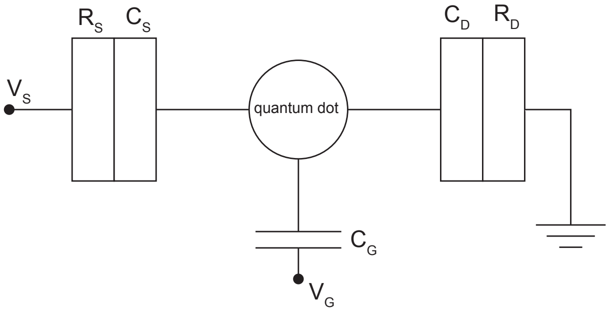

Figure 3.2: Schematic representation of the CIM for a QD. The dot is tunnel-coupled to source and drain electrodes and capacitively coupled to a gate electrode.

3.4 demonstrates the need for small devices and low temperatures if single electron effects are to be resolved experimentally. For example, the charging energy of a metallic island with diameter 100 nm is of the order of 1 meV, which corresponds to a temperature of roughly 12 K [83]. In this work, the creation of QDs with dimensions on the order of tens of nanometres is achieved electrostatically by applying voltages to gate electrodes incorporated into the device architecture. In Section 3.1.5, we will examine the mechanisms used to achieve this in the experimental platforms employed in this thesis.

We note briefly that QDs can be combined in series to create chains of double, triple or more dots [113]. Although the physics of these multiple QD systems is rich, this work makes exclusive use of single QDs and we do not discuss the multiple dot case further.

3.1.2 Constant interaction model

An approximate description of the electronic state of a QD of the type shown in Fig. 3.1 is provided by the constant interaction model (CIM) [67, 68]. The model is based on two assumptions. First, the Coulomb interactions between an electron on the dot and all other electrons both on and off the dot can be parametrised by a single capacitance C. Second, the single particle energy level structure of the electrons on the dot is unaffected by interactions between electrons. The CIM models the dot as an island capacitively coupled to a gate electrodes and tunnel coupled to source and drain electrodes. The idea is illustrated in Fig. 3.2. Source and drain tunnel junctions are parametrised by resistances $R_{S,D}$ and capacitances $C_{S,D}$, and the capacitive coupling to the gate by a capacitance C_G. With the drain grounded, voltages V_S and V_G can be applied to the source and gate electrodes. Simple electrostatic arguments then lead to the following expression for the electrostatic energy of the island

$$U(N) = \frac{(Ne)^2}{2C} - NeV_{\text{ext}} + \sum_{n=1}^{N} E_n, \tag{3.8}$$

where $C = C_S + C_D + C_G$ is the total capacitance, N is the number of electrons on the island and E_n the energy of the nth single particle energy. V_{ext} is an effective external potential given by

$$V_{\text{ext}} = (C_S V_S + C_D V_D + C_G V_G)/C. \tag{3.9}$$

The electrochemical potential of the dot $\mu(N)$ is defined to be the energy required to add the Nth electron to the dot. If the dot initially contains $N-1$ electrons, $\mu(N)$ is given by

$$\mu(N) = U(N) - U(N-1) = E_C\,(2N+1) - eV_{\text{ext}} + E_N. \tag{3.10}$$

Thermodynamically the electrochemical potential dictates the flow of particles in or out of a system. A difference in electrochemical potential between two coupled systems will drive in an exchange of particles until equilibrium is established and the combined system can be characterised by a single electrochemical potential. As will be discussed in Section 3.1.3, in the context of electron transport through a quantum dot, the definition of the electrochemical potential provided by Eq. 3.10 fulfils this role.

However, this definition, although widely used in the mesoscopic transport literature [49,54,68,83], is not identical to the chemical potential in the strict thermodynamic sense,

$$\mu = (\partial U/\partial N)_{S,V},$$

since, for a small system N is discrete and the derivative is defined for a continuous variable. A common resolution is to define a finite-difference chemical potential in terms of the Helmholtz free energy [64],

$$\mu(T,V,N) = F(T,V,N) - F(T,V,N-1). \tag{3.11}$$

However, given the free energy of a system is defined as

$$F = U - TS,$$

the definition given by Eq 3.10. is only compatible with Eq. 3.11 if neither the temperature or entropy of a quantum dot are changed by the addition or removal of a single electron. However, in Ref [89] it is argued that changing the number of electrons on the dot necessarily changes its entropy. To account for this Ref [89] consider the mean population of the dot $\bar{N}$ defined as

$$\bar{N} = N + n,$$

where N is the base population of the dot, which remains unchanged, and n the average excess population of the dot, which varies smoothly between 0 and 1. The mean free energy of the dot is then given by

$$\bar{F} = U(N) + \varepsilon n - TS,$$

where ε is referred to as the dot's single particle energy level defined according to Eq. 3.10. From these definition the following expression is derived

$$\epsilon - \mu = T \left(\frac{\partial S}{\partial n} \right)_T,$$

which makes explicit the entropic contribution to the chemical potential. Although this definition is more thermodynamically rigorous than the one provided by Eq. 3.10, in this work we will use the definition provided by Eq. 3.10 since, by dictating the flow of electrons through the dot, it fulfils the role required for analysis presented here.

3.1.3 Electron transport through quantum dots

With the drain grounded, applying a bias voltage V_S to the source shifts μ_S relative to μ_D resulting in a non-zero value of $\Delta\mu_{S,D}$ resulting in the flow of current through the dot. This current can be understood as the source and drain electrodes attempting to bring the dot into diffusive equilibrium with themselves [33]. For $\mu_S > \mu > \mu_D$ the source seeks to bring the dot into equilibrium with itself by adding electrons to the dot. Equilibrium is never achieved, however, since the drain simultaneously removes electrons from the dot in its own attempt to establish equilibrium. The dot is driven into a non-equilibrium steady state and a net current flows from source to drain. For $k_BT \gg \hbar\Gamma$ this current is given by [33]

$$I = e\frac{\Gamma_S\Gamma_D}{\Gamma_S + \Gamma_D}\left(f_S(\mu) - f_D(\mu)\right). \tag{3.12}$$

From Eq. 3.12 we see that when μ is above the source $f_S(\mu) = f_D(\mu) = 0$ and no current flows. Similarly, no current flows when μ is below the drain and $f_S(\mu) = f_D(\mu) = 1$. Current does flow when $f_S(\mu) \neq f_D(\mu)$. The values of μ for which $\mu_S > \mu > \mu_D$ is known as the *bias window*.

A transition between N and $N{+}1$ electrons represents a channel through which current can flow. These charge transitions constitute a ladder of transport channels separated by an *addition energy* given by

$$E_{\text{add}} = \mu(N) - \mu(N-1) = \frac{e^2}{C} + (E_{N+1} - E_N). \tag{3.13}$$

This ladder of transport channels can be shifted up or down by adjusting the gate voltage V_G. If the bias across the device is small such that $\Delta\mu_{S,D} < E_{\text{add}}$ then no more than one transport channel can fit in the bias window. Sweeping V_G and measuring the current through the dot then results in a series of *Coulomb peaks*. The idea is illustrated in Fig. 3.3. Each Coulomb peak corresponds to a given transport channel moving through the bias window. In the regions of zero current between the peaks the number of electrons on the dot is fixed and the dot is said to be in *Coulomb blockade*.

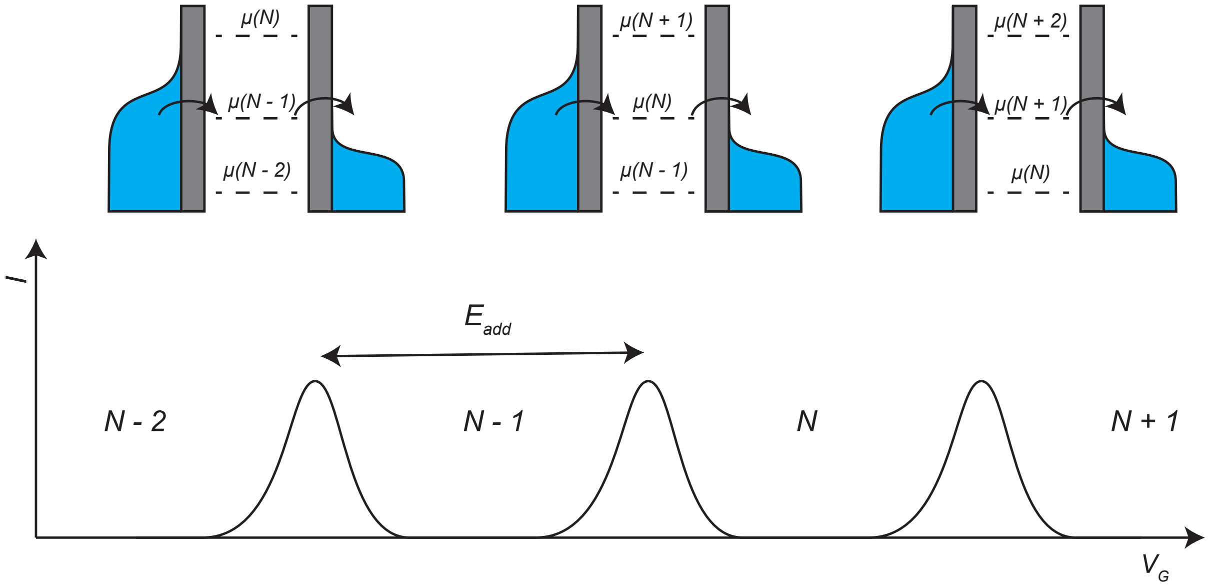

Figure 3.3: Current through a QD as a function of gate voltage. Current only flows when a transport channel resides in the bias window resulting in a series of peaks between which the number of electrons on the dot is fixed.

A measurement of the current through the dot as a function of V_G and V_{SD} results in the diamond pattern shown in Fig. 3.4.

The grey regions of this plot, known as *Coulomb diamonds*, represent combinations of bias and gate voltage for which the dot is in Coulomb blockade. The red and blue edges of the diamonds correspond to the electrochemical potential of the dot being aligned with the source and drain respectively.

Eq. 3.12 applies in the case that $k_BT \gg \hbar\Gamma$. When $\hbar\Gamma \gg k_BT$ the effects of lifetime broadening must be taken into account and the expression for the current becomes

$$I = e\frac{\Gamma_S\Gamma_D}{\Gamma_S + \Gamma_D}\int_{-\infty}^{+\infty} dE D(E)[f_S(E) - f_D(E)]. \tag{3.14}$$

Here $D(E)$, typically a Lorentzian with width $\hbar\Gamma$ [33, 75, 116], is a normalized density of states describing the lifetime-broadened energy level of the dot as a function of electron energy E.

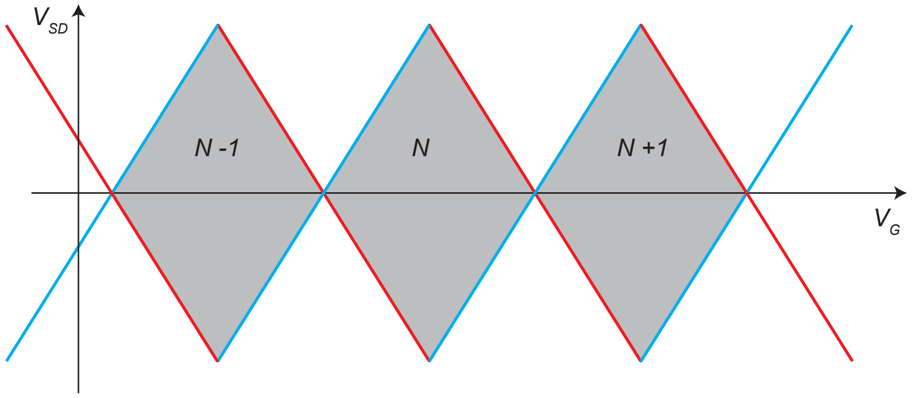

Figure 3.4: Current through the QD as function of V_G and V_{SD}. In the grey diamonds transport is blocked and the number of electrons on the dot is fixed. Outside of the diamonds current flows. The red and blue edges of the diamonds correspond the electrochemical potential of the dot being aligned with the source and drain respectively.

3.1.4 Classical master equations for single electron transport

For small source-drain bias, such that only one transport channel sits within the bias window, Coulomb blockade dictates that electrons tunnel through the dot one at a time. In Chapter 4 we assume the dynamics of this single electron transport to be Markovian and model them using a set of classical master equations. Given that the quantum dot system is inherently quantum mechanical a complete description of its dynamics would require a quantum master equation governing the evolution of its reduced density matrix. Adopting a classical approach therefore requires us to make additional assumptions regrading the transport process.

Firstly, we assume that the coherence time of any superposition of empty and occupied states of the dot is extremely short compared to the tunnelling rates of the dot. As a result, we can describe the occupation of the quantum dot in terms of classical probabilities rather than a reduced density matrix.

Secondly, we treat the source and drain reservoirs as macroscopic particle reservoirs with an effectively infinite number of degrees of freedom and and correlation times that are extremely short compared to the tunnelling rates of the dot. The result of this is that electron tunnelling events can be treated as being effectively memoryless, once the dot becomes empty or occupied, the probability per unit time for a tunnelling event to occur depends only on the instantaneous state of the dot and not its history. Taken together, these assumptions.

As we shall see in Chapter 4, these assumptions are borne out by the close agreement between the experimental data and the theoretical predictions obtained using a classical master equation framework.

3.1.5 Experimental platforms

In this section, we provide a brief overview of the two experimental platforms studied in this work: a gate defined QD in a Ge/SiGe heterostructure and a suspended CNT device. Although the analysis of Section 3.1 applies to both systems, they differ in a number of important ways. At a superficial level the semiconducting host material in which QDs are defined differs between the two systems, as does the device architecture. At a more fundamental level, while both devices use a gate architecture to facilitate electrostatic confinement and create QDs, the physical mechanism responsible for this confinement differs between the devices. Charge carriers in CNTs can be tuned via the application of appropriate gate voltages to be either electrons or holes [69]; however, in the Ge/SiGe device studied in this work transport was exclusively hole based. Throughout this work we are primarily concerned with transport through QDs in the so-called *sequential tunnelling* regime [42, 48], where charge moves through QDs one-by-one via a series of discrete tunnelling events between the source, drain and dot.

3.1.6 Gate defined quantum dot devices in Ge/SiGe

In recent years germanium has emerged as a leading platform for the realisation of high-quality QDs. A high hole mobility results in ultra-clean tunable devices, while a low hole effective mass relaxes fabrication constraints resulting in QDs with large energy level spacing [95]. The specific platform utilised in this work consisted of a Ge/SiGe heterostructure a schematic of which is shown in Fig. 3.10. A 20 nm layer of Ge is sandwiched between layers of SiGe. Valence band offsets at the interfaces between the Ge and SiGe layers confine holes to a narrow region just below the surface of the Ge layer [95]. While holes are free to move in the in-plane directions, they are tightly confined

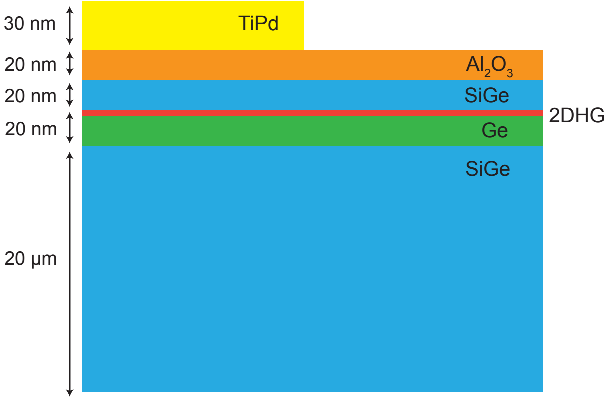

Figure 3.5: Schematic of the gate defined QD Ge/SiGe heterostructure device used in this work. A 2DHG forms just below the surface of the Ge layer. Positive voltages applied to TiPd gates control the potential landscape within the 2DHG and allow for the formation of QDs.

in the growth direction, resulting in the formation of a so-called *two-dimensional hole gas* (2DHG). The Ge/SiGe heterostructure is capped by a 20 nm layer of Al_2O_3 acting as a gate dielectric. Metallic gates are then patterned on the surface using a combination of electron beam lithography (EBL) and thermal evaporation. Figure 3.6 shows a scanning electron microscope (SEM) image of the device used in this work. The gate architecture defines two arrays of QDs, two in the top half of the device and five in the lower half. An account of how the gate architecture is used to define and measure QDs is given in Section 3.2 below. The device used in this work was fabricated in the Nanofabrication Facility at IST Austria by the Katsaros Group. A full description of the fabrication process can be found in Ref. [60].

3.1.7 Suspended carbon nanotube devices

The electronic properties of CNTs are favourable to the formation of electrostatically defined QDs. They exhibit semiconducting behaviour [69], support ballistic transport over micrometer scales [85,129], and, when incorporated into a device with a gate architecture, allow for a high degree of control over the electrostatic potential responsible for confining electrons and holes in QDs [9]. In addition they exhibit remarkable mechanical properties. A combination of low mass, high tensile strength and high elastic modulus [40] mean CNTs make excellent nanomechanical resonators, with quality factors as high as 5

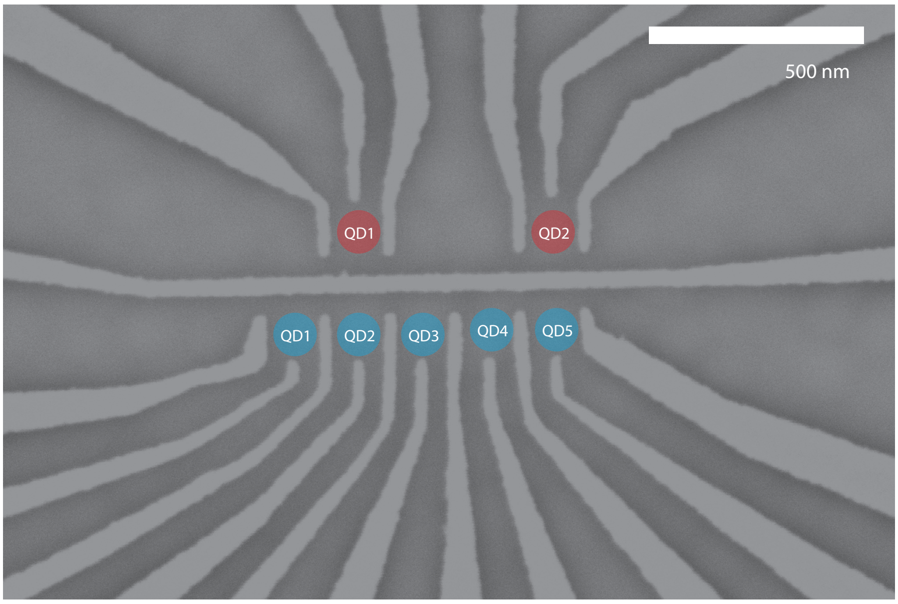

Figure 3.6: An SEM of the Ge/SiGe device used in this work showing the gate architecture. Five QDs can be formed in the lower half of the device and two in the upper half.

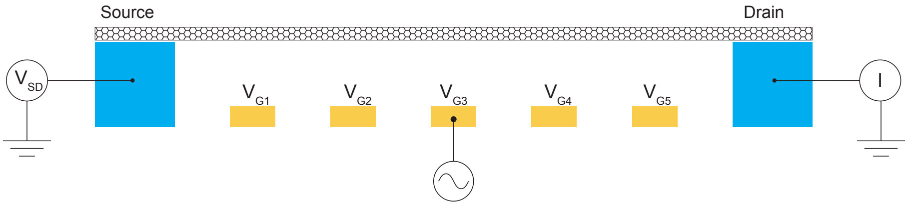

Figure 3.7: Schematic of the CNT device used in this work. A CNT is suspended between source and gate electrodes and above five gate electrodes. A voltage V_{SD} applied at the source results in a current through the CNT which can be measured at the drain. An ac voltage can be applied to a gate electrode to drive the mechanical motion of the CNT.

million being reported [80].

Figure 3.7. shows a schematic of the suspended CNT device used in this work. A CNT is suspended between metallic source and drain electrodes and above five gate electrodes. A bias can be applied across the CNT via the application of a voltage V_{SD} to the source with the resulting current measured at the drain.

Suspended CNT devices of the kind shown in Fig. 3.7 have been shown to demonstrate coupling between single electron transport through a QD defined within the CNT and its mechanical motion [9, 53, 73, 75, 105, 116]. Specifically, a modulation in the position of the CNT changes the capacitance between the gate and the CNT, which via Eq. 3.10 modulates the electrochemical potential of the dot. This, in turn, has the effect of modulating the current through the dot as we will now show. The CNT can be driven into motion by applying an oscillating voltage to a gate below the CNT at its mechanical resonance frequency ω_0. The resulting oscillation of the CNT is described by

$$u(t) = u_0 \cos(\omega_0 t), \tag{3.15}$$

where u is the displacement of the CNT from it equilibrium position and u_0 the amplitude of the oscillations. A change in the position of the CNT du changes the capacitance between the gate and QD, C_G, by an amount dC_G such that

$$C_{\text{tot}} = C_G + dC_G, \tag{3.16}$$

where C_{tot} is the total gate capacitance. For small u_0 the capacitance oscillates at ω_0 with amplitdue

$$\Delta C_G = \frac{dC_G}{du} u_0. \tag{3.17}$$

The capacitive coupling between the dot and gate allows us to write

$$dq = d(C_G V_G) = C_G dV_G + dC_G V_G, \tag{3.18}$$

where q is the charge on the dot. The first term of Eq. 3.18 occurs at all frequencies and represents a change in the charge on the dot due to a change in the gate voltage. Here we are interested in the current through the CNT as a result of its mechanical motion, we therefore ignore this term. The second term is non-zero only when the CNT is oscillating and the capacitance is periodically modulated. The change in the induced charge on the CNT due to mechanical motion alone is therefore

$$dq = dC_G V_G. \tag{3.19}$$

The change in the induced charge on the CNT as a result of the change in the capacitance can be imagined to be the result of an effective change in the gate voltage V_G^{eff} allowing us to write

$$dV_G^{\mathrm{eff}} = \frac{dq}{C_G} = \frac{dC_G V_G}{C_G}. \tag{3.20}$$

The effective gate voltage oscillates at ω_0 with amplitude

$$\Delta V_G^{\mathrm{eff}} = \frac{\Delta C_G V_G}{C_G} = \frac{V_G}{C_G}\frac{dC_G}{du}u_0, \tag{3.21}$$

such that

$$V_G^{\mathrm{eff}}(t) = \Delta V_G^{\mathrm{eff}} \cos(\omega t). \tag{3.22}$$

The dc current through the CNT is a function of V_G (see Fig. 3.3), which is now modified by $V_G^{\mathrm{eff}}(t)$. Taylor expanding gives

$$\begin{aligned} I\Big(V_G + V_G^{\mathrm{eff}}(t)\Big) = I(V_G) &+ \frac{\partial I}{\partial V_G}\,\Delta V_G^{\mathrm{eff}} \cos(\omega_0 t) \\ &+ \frac{1}{2}\frac{\partial^2 I}{\partial V_G^2}\Big(\Delta V_G^{\mathrm{eff}} \cos(\omega_0 t)\Big)^2 \\ &+ \frac{1}{6}\frac{\partial^3 I}{\partial V_G^3}\Big(\Delta V_G^{\mathrm{eff}} \cos(\omega_0 t)\Big)^3 + O(u_0^4). \end{aligned} \tag{3.23}$$

Low pass filtering in the cryogenic lines carrying the current from the CNT to the measurement apparatus averages out all periodic terms in the expansion giving and average measured current $\bar{I}$

$$\bar{I}(u_0, V_G) = I(V_G) + \frac{u_0^2}{4}\left(\frac{V_G}{C_G}\frac{dC_G}{du}\right)^2 \frac{\partial^2 I}{\partial V_G^2} + O(u^4). \tag{3.24}$$

We see that the mechanical motion of the CNT modifies the measured DC current through the dot, adding a correction proportional to u_0^2 that depends on the second derivative of the current with respect to gate voltage.

Further signatures of the electromechanical coupling in carbon nanotube quantum dot (CNTQD) devices are a softening of the mechanical resonance frequency of the CNT as the electrochemical potential of the dot is swept through a Coulomb peak and a modification of the mechanical resonance frequency with gate voltage. The first of these is the result of an additional position dependent force experienced by the CNT caused by average number of electrons on the dot changing with its position. This additional force results in a modification of the CNT's spring constant and a decrease in the mechanical resonance frequency [73, 105, 116]. The second results from a gradual tensioning of the CNT as the gate voltage is swept and the electrostatic force on the dot changed. Examples of these two phenomena will be given in Section 5.5.2.

Of particular importance to this work is the ability of a CNTQD system to support self sustained oscillations [122]. The origin of these oscillations can be traced to back-action forces on the CNT from electron tunnelling events perturbing its motion. Despite the stochastic nature of these forces, in the right regime they give rise to the formation of a limit cycle where the energy lost to dissipation over the course of a single oscillation period is balanced by injections of energy into the CNT system by the back action forces [122]. In Appendix D we describe this mechanism in more detail including a theoretical description due to Ref. [28].

Two mechanisms are responsible for the creation of single QDs in semiconducting CNT devices. Firstly, Schottky barriers form at the interface between a semiconducting CNT and the metal source-drain contacts [13] spatially confining electrons along the length of the CNT. Secondly, gate electrodes can be used to electrostatically dope the CNT [9, 69, 118]. The idea is illustrated in Fig. 3.8, where the region of the CNT above the gate electrodes has been n-doped through the application of positive gate voltages. The flow of current through a QD is determined by the availability of states around the dot's electrochemical potential [33]. Electrostatic doping of the CNT therefore allows the conductance of the QD to be controlled via the application of gate voltages.

3.2 Measurement and readout

3.2.1 Tuning quantum dots

In order to establish the configuration shown in Fig. 3.1 in a real device, it is necessary to tune gate voltages to bring the device into a regime where a QD can form. A simplified schematic of one of the QDs shown in Fig 3.6 is given in Fig. 3.9. Three gates (two

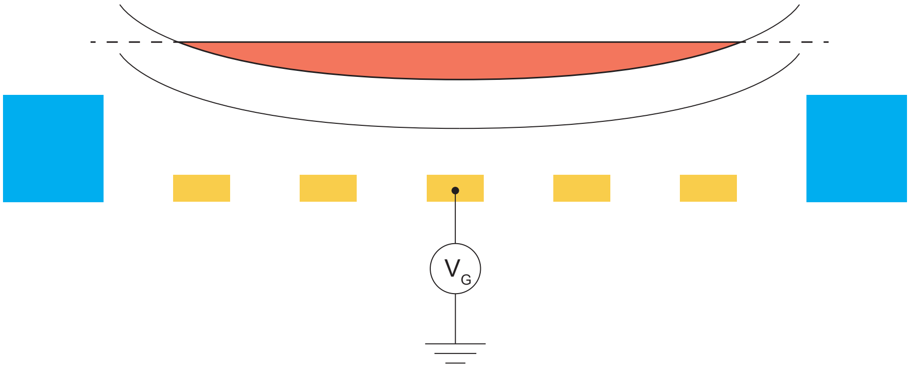

Figure 3.8: Schematic showing the band diagram of a CNT and the formation of a QD in a suspended CNT device. A positive voltage V_G applied to a gate electrode bends the valence and conduction bands, causing the region above the gate electrodes to become n-doped.

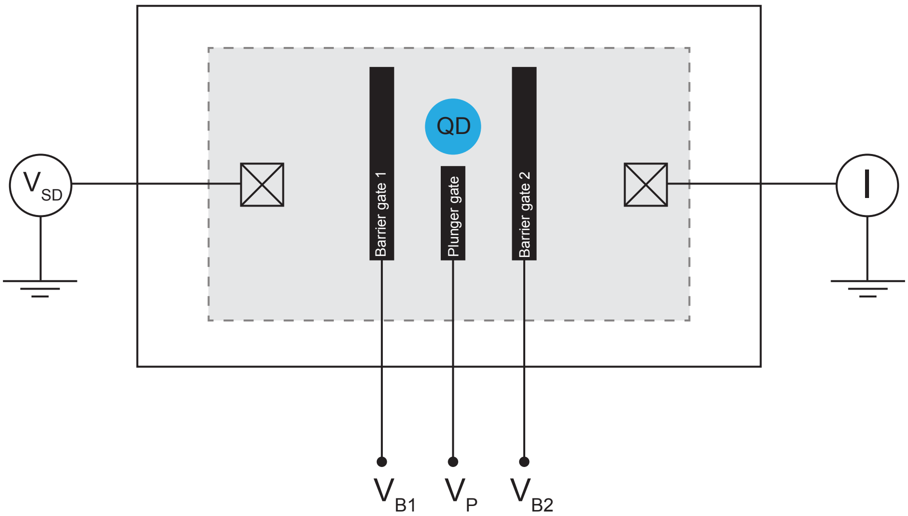

Figure 3.9: Simplified schematic of one of the QDs shown in Fig. 3.6. Voltages V_{B1}, V_{B2} and V_P can be applied to two barrier gates and a plunger gate to form a QD. A bias V_{SD} can be applied across the device and the current through the QD measured.

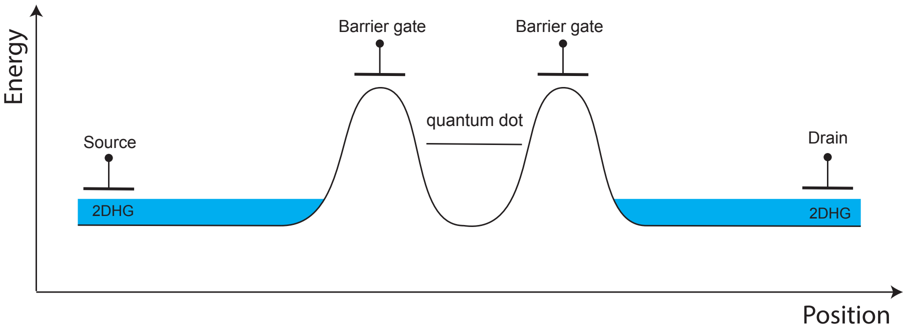

Figure 3.10: Schematic showing the use of gates to create a QD within a 2DHG. Positive voltages applied to barrier gates deplete the 2DHG and create potential barriers that confine holes and create a QD.

barrier gates and a plunger gate) are available to tune the electrostatic landscape of the 2DHG and create a QD. The primary role of the barrier gates is to create and tune the tunnel barriers that confine the dot. The idea is illustrated in Fig 3.10. When no external voltage is applied to gates the device's 2DHG is undisturbed and current can flow freely. Applying positive voltages to the barrier gates depletes the region of the 2DHG below the gates creating potential barriers, which, when appropriately resistive (see Eq. 3.7) form a QD. Ideally, once a QD is formed the plunger gate can be used to control the electrochemical potential of the dot. However, the electric field generated by the gates is not confined to the regions below the gates, meaning barrier gates can affect the electrochemical potential and the plunger gate the width of the barriers, a phenomenon known as *crosstalk*. Together, the voltages applied to the gates define a three-dimensional voltage space. The process of tuning a QD then involves finding a region within this space where a well defined dot can form. Fig. 3.11 shows a measurement of current through the dot as a function of the two barrier for two different plunger gate voltages. The data was taken using the Ge/SiGe device described in Section 3.1.6. In the lower left regions of these so called *charge stability diagrams* the resistance of the tunnel barriers is low such that the condition given by Eq. 3.7 is not met and the QD is not well defined. Current flows freely and the device is said to be open. In the black regions the resistance of one, other or both of the tunnel barriers is too high for a measurable current to flow, and the device is said to be closed. Between Fig. 3.11a and Fig 3.11b we raise the plunger gate from 0.4 V to 0.5 V. In doing so we move the device into a region of gate voltage space

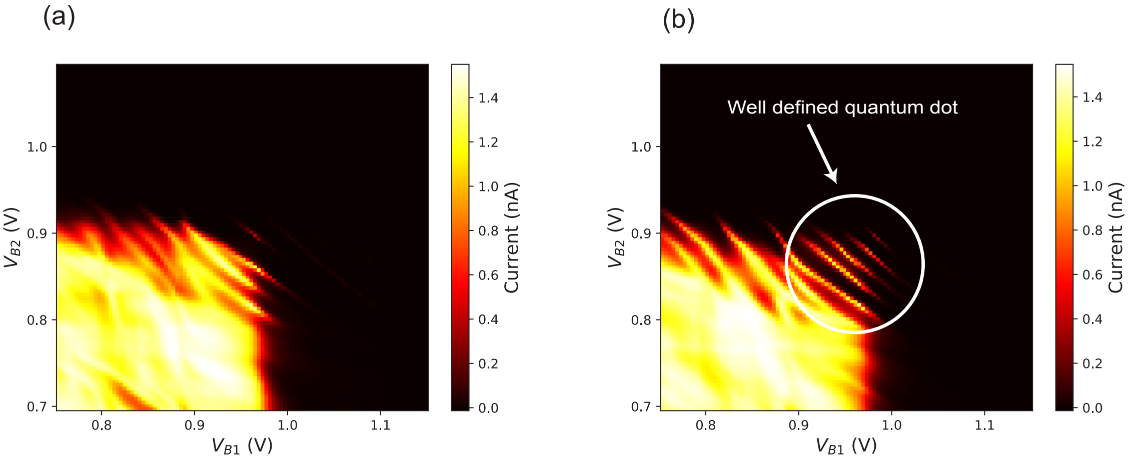

Figure 3.11: Example charge stability diagrams measured in a Ge/SiGe device showing current through the device as a function of barrier gate voltages. A bias of 0.1 mV was applied across the device. Between (a) and (b) the plunger gate of the device was increased from 0.4 V to 0.5 V revealing periodic peaks characteristic of a QD.

favourable to the formation of a QD. The emergence of a series of parallel peaks in the current signifies the formation of the dot, as crosstalk from the two barrier gates sweeps the dot's electrochemical potential through the bias window.

3.2.2 DC and rf readout of quantum dots

The experiments presented in this work were carried out at millikelvin temperatures in a dilution refrigerator, using a combination of dc and rf measurement techniques. Dc transport measurements were performed by routing the current from the device under test (DUT) through dedicated dc lines in the fridge to a room-temperature current amplifier. A dc setup is well suited to measuring features such a Coulomb peaks and Coulomb diamonds, where time-averaged measurements are sufficient to resolve the features of interest. However, the bandwidth of a standard dc transport setup is limited by the RC low-pass filter formed by the resistance of the DUT and current amplifier and the capacitance of the dc lines connecting the DUT to the room temperature measurement instruments [115]. Quantum devices typically have a resistance of the order of the QOR $h/e^2 \approx 25.8\,\mathrm{k}\Omega$, with the capacitance of the cables between ranging between 0.1 and 1 nF, leading to a typical bandwidth of a few kilohertz [115]. As a result, rf techniques are required to measure phenomena occurring on timescales shorter than a few milliseconds.

In this work we study two such processes, namely the mechanical oscillations of a suspended CNT and the real-time tunnelling of electrons through a QD. The first of these is measured via a transmission measurement the details of which are explained in Section 5.3.1. The second is measured using rf-reflectometry. Here we give a brief overview of the principles of rf-reflectometry. A full schematic of the measurement setup used to implement the technique is provided in Section 4.3.1.

Reflectometry working principles

RF reflectometry is based on the principle that a portion of a signal propagating along a transmission line will be reflected if it encounters an impedance mismatch [96, 115]. Therefore, in principle, information regarding the impedance of a DUT can be obtained by placing it at the end of a transmission line and measuring the reflected signal. Consider a DUT with a load impedance Z_{load}, connected to a transmission line with characteristic impedance Z_0. The reflection coefficient, corresponding to the fraction of the input signal reflected at the impedance mismatch, is given by

$$\Gamma = \frac{Z_{\text{load}} - Z_0}{Z_{\text{load}} + Z_0}. \tag{3.25}$$

In Fig. 3.12 we plot the magnitude of Γ as a function of Z_{load}/Z_0. As Z_{load} increases the dependence of $|\Gamma|$ on Z_{load} decreases. For $|Z_{\text{load}}| \gg Z_0$ the dependence is minimal. Given QOR $\gg Z_0$, simply placing the DUT at the end of a transmission line does not provide sufficient sensitivity to variations in the device impedance. The solution to this problem is to embed the DUT into an LC circuit resulting in a matching circuit whose overall impedance can be adjusted to be close to Z_0.

Impedance matching

Fig. 3.13a shows a schematic of the matching circuit used to perform reflectometry in this work.

The DUT, with resistance R_S, is embedded within an LC circuit comprising an inductor of inductance L, and capacitors with capacitances C_D and C_S. The impedance of

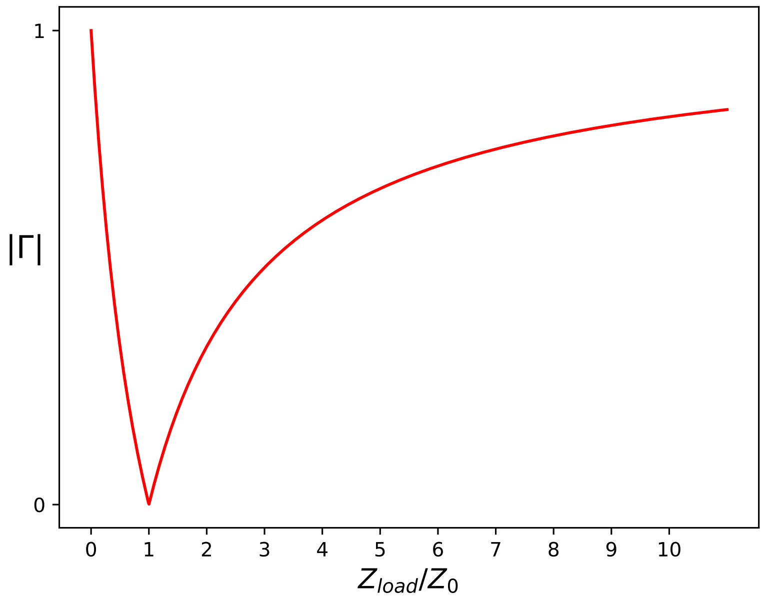

Figure 3.12: Magnitude of the reflection coefficient $|\Gamma|$ plotted as a function of Z_{load}/Z_0

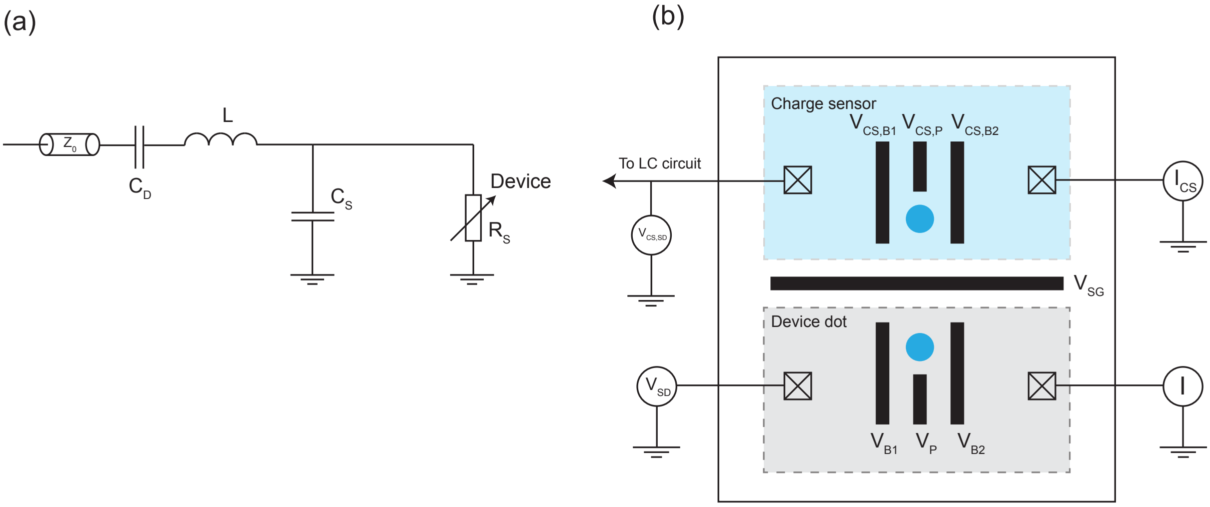

Figure 3.13: (a) Schematic of the matching circuit described in Section 3.2.2. The device with a resistance R_S is incorporated into an LC circuit consisting of an inductor L and capacitors C_S and C_D. The circuit is coupled to a transmission line with characteristic impedance Z_0. (b) Schematic of a charge sensing setup. Device and sensor dots can be tuned using using a combination of barrier and plunger gate voltages. Capacitive coupling between the dots is controlled by applying a voltage V_{SP} to a splitter gate. The device dot can be biased with a voltage V_{SD} and the sensor dot with a voltage $V_{CS,SD}$. The sensor dot is incorporated into and LC circuit for impedance matching.

the circuit is given by

$$Z_{\text{load}} = \frac{1}{j\omega C_D} + j\omega L + \frac{R_S}{1 + j\omega C_S R_S}. \tag{3.26}$$

For the circuit used in this work we have $C_D \gg C_S$ and $R_S \gg 1$ such that we can drop the first term of Eq. 3.26 giving

$$Z_{\text{load}} = j\omega L + \frac{R_S}{1 + j\omega C_S R_S}. \tag{3.27}$$

In the limit of $\omega R_S C \gg 1$, which is true for the circuit used in this work, the angular resonance frequency of the circuit is given by

$$\omega_0 = \frac{1}{\sqrt{LC_S}}. \tag{3.28}$$

As shown in Appendix A, on resonance the impedance of the circuit then simplifies to that of a series LCR circuit with impedance

$$Z_{\text{load}} \approx R_{\text{eff}} + j\omega L + \frac{1}{j\omega C_S}, \tag{3.29}$$

where R_{eff} is an effective resistance given by

$$R_{\text{eff}} = \frac{L}{R_S C_S}. \tag{3.30}$$

Matching is then achieved by choosing L and C_S such that $R_{\text{eff}} = Z_0$, with maximum sensitivity achieved by driving the circuit at its resonance frequency ω_0 such that its impedance is reduced to R_{eff} and matching is perfect. For the circuit used in this work we have $L = 220\,\text{nH}$, $C_D = 82\,\text{pF}$ and $C_S = 10\,\text{pF}$.

RF charge sensing

For the experiment detailed in Chapter 4 of this work it was necessary to measure the real-time occupation of a QD. A well established technique for carrying out such a mea-

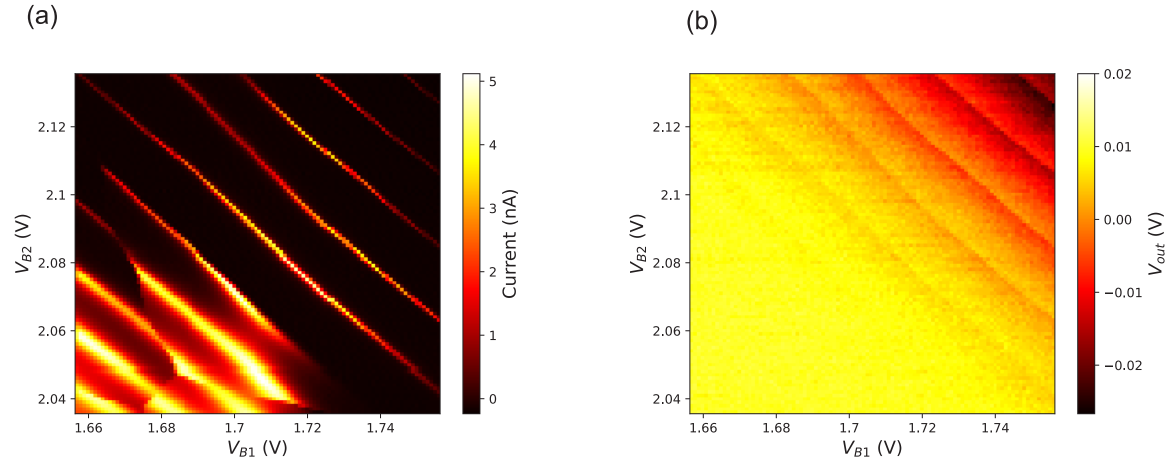

Figure 3.14: Comparison of charge stability diagrams measured using DC transport and rf charge sensing. (a) DC current through the device as a function of the barrier gate voltages. (b) Reflected voltage V_{out} measured via rf charge sensing, plotted against the same gate voltages. The data was acquired using the Ge/SiGe device described in Section 3.1.6 with both the device and sensor dots biased at 0.1 mV.

surement is rf charge sensing [3,51,66,93,117]. In a charge sensing measurement a sensor is capacitively coupled to the QD of interest such that its impedance depends sensitively on the charge state of the QD. Typically, the sensor is either a quantum point contact [41,91] or a second QD [82, 127]. In this work we employed a QD charge sensor. A simplified schematic of the charge sensing setup is shown in Fig. 3.13b. The device and sensor dots are positioned in close proximity to one another and can be tuned using a combination of barrier and plunger gates. Capacitive coupling between the dots is controlled by a voltage V_{SG} applied to a splitter gate. Due to this coupling, a change in the charge state of the device dot induces a shift in the electrostatic potential environment felt by the sensor dot, which acts as an effective change in its gate voltage. The gate voltage of the sensor dot is biased to the edge of a Coulomb peak where its impedance is most sensitive to changes in gate voltage. By embedding the sensor dot in a matching circuit, changes in its impedance can be measured using rf charge sensing. In Fig. 3.14 we show the same charge stability diagram measured using dc current through the device dot (Fig. 3.14a) and reflectometry of a sensor dot (3.14b). When measured in dc, Coulomb peaks are visible as sharp peaks in the current. When measured using rf charge sensing, Coulomb peaks show up as abrupt changes in the reflected signal. The gradual background shift observed in Fig. 3.14b is caused by the barrier gate voltages of the device affecting the

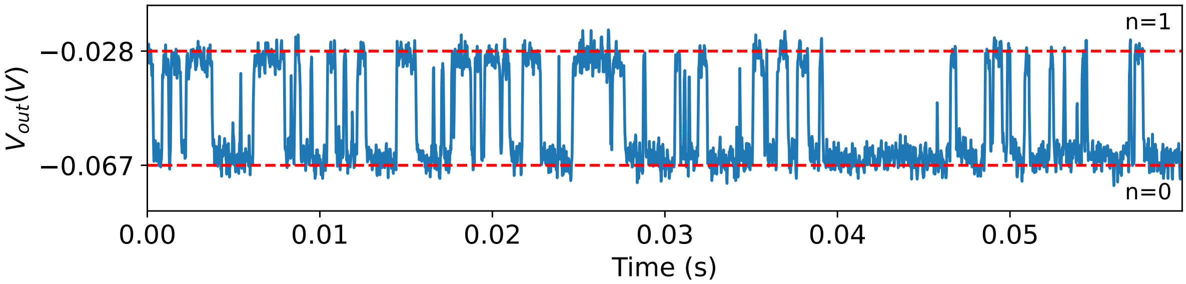

Figure 3.15: Real-time measurement of the reflected signal V_{out} obtained using charge sensing reflectometry of a QD. The two discrete levels, labeled $n = 0$ and $n = 1$, correspond to the absence and presence of an additional electron on the dot, respectively. The data was acquired using the Ge/SiGe device described in Section 3.1.6.

electrostatic environment of the sensor dot. A further example of cross-talk, this effect can be understood as the barrier gates contributing to the effective gate voltage of the sensor dot, causing the position of the sensor's Coulomb peak to shift in response to changes in the voltages applied to the device dot.

If transport through the device dot is sufficiently slow, such that changes in the occupation of the dot happen on a time scale that is longer than the response time of the dc measurement circuit, charge sensing can be performed using a dc setup, with the current through the sensor dot reflecting the occupation of the device dot [117]. In this thesis, transport was too fast to be resolved by a DC measurement setup. We therefore employed reflectometry to measure changes in the impedance of the sensor resulting from the changes in the charge state of the device dot. An example of such a measurement is shown in Fig 3.15 , which shows a real-time measurement of the signal V_{out} reflected from the matching circuit. As an electron tunnels on or off the device dot, the impedance of the matching circuit changes, giving rise to a noisy random telegraph signal. In the figure, the two levels labelled $n = 0$ and $n = 1$ correspond to the absence and presence of an additional electron on the dot, respectively.

3.3 Carbon Nanotube Fabrication

3.3.1 Introduction

The development of techniques for the fabrication of QD devices is motivated by two guiding principles. Firstly, devices should be clean, meaning that the potential landscape within which the QDs are formed is free of disorder and environmental interference. Secondly, the potential landscape used to create and manipulate the QDs should be precisely and predictably controllable - they should be tunable. The fabrication of clean and tunable CNT devices is particularly challenging. Unlike heterostructure devices, such as the one introduced in Section 3.1.6, where charge carriers are isolated from the device's surface by an atomically clean buffer layer, charge carriers in CNTs reside on the surface on the nanotube. As a result, the fabrication process can easily introduce disorder [69].

Three main fabrication methods exist for the creation of CNT devices. In the simplest of these, top gating, gates are patterned using EBL on top of CNTs. Early single electron transistors [15] as well as the first double QDs [74] were fabricated in this way. However, exposing CNTs to the fabrication process renders devices fabricated using top gating particularly susceptible to disorder. An alternative approach is bottom gating, where CNTs are grown over a prefabricated gate architecture [20, 108]. Although this method offers improved tunability and reduced disorder compared to top gating, it requires exposing the device to the high temperatures necessary for CNT growth (approximately 900°C), imposing constraints on material and design choices. Mechanical transfer techniques overcome this limitation by growing CNTs on a separate chip and subsequently transferring them onto a device chip that has been independently fabricated with the desired gate architecture. The most straightforward form of transfer, and the one used in this thesis, is known as *stamping* [124]. In this method, the CNT growth chip and the device chip are brought into close proximity, causing the CNTs to adhere to the device chip at points of contact (typically source and drain electrodes). A more sophisticated variant of this method involves precisely aligning and contacting the growth and

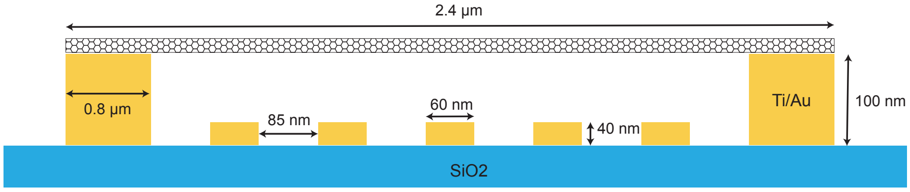

Figure 3.16: Schematic of a suspended CNT device. Source, drain, and gate electrodes are patterned onto a SiO_2 substrate using a combination of optical lithography and EBL. A CNT spans the source and drain electrodes and is integrated into the device using the stamping technique.

device chips using piezoelectric motors, followed by the application of a large current to sever the CNTs [27, 118]. This process can be performed under vacuum and at cryogenic temperatures, allowing the electronic cleanliness of the devices to be tested *in situ*.

The following sections outline the fabrication process used to create the suspended CNT devices described in Section 3.1.7. The procedure follows the stamping method, with recipes and techniques adapted and optimized from Ref. [120] to suit the specific capabilities of the available fabrication facilities. The stamping method had been successfully employed within our group over several years to fabricate CNT-based devices [116, 122]. However, by the time this work was carried out, fabrication within the group had paused. The following therefore reflects the efforts of myself and postdoctoral researcher Dr. Yikai Yang to re-establish a CNT fabrication pipeline within the group. The work presented in this chapter marks a significant step forward in the realisation of the experiments detailed in Section 5 of this thesis.

Fig. 3.16 shows a schematic of the device. Gold source, drain and gate electrodes are patterned on a SiO_2 substrate with a CNT suspended between the source and drain. The fabrication process for this device proceeds in three stages. Firstly, a device chip is fabricated, incorporating source, drain and gate electrodes. Secondly, CNTs are grown on a separate quartz chip, suspended between pairs of pillars. Finally, the CNTs are transferred to the base chip using the stamping technique. Each of these stages will be discussed in detail below.

Fig. 3.17 provides an overview of the nanofabrication equipment used throughout the fabrication process described in this section.

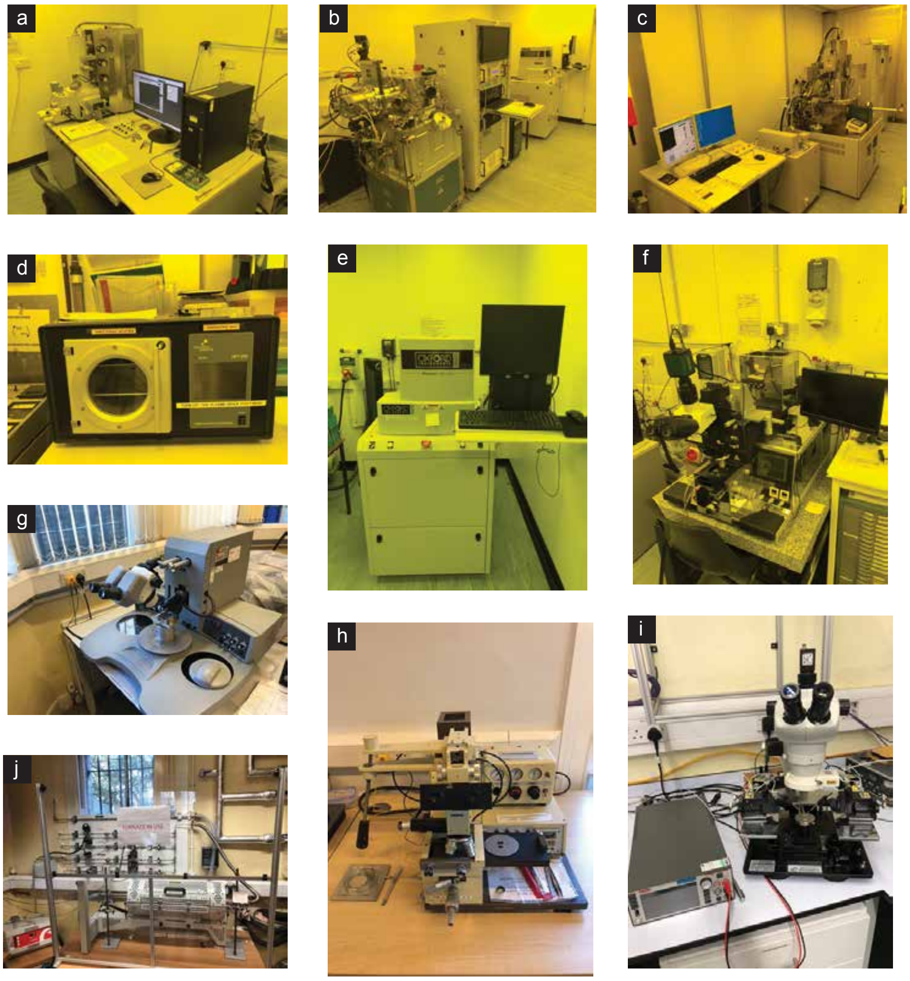

Figure 3.17: Overview of the nanofabrication machines used in this thesis. (a) Hitachi S-4300 microscope. (b) Plassys MEB550S ebeam evaporator. (c) JEOL JBX-5500ZC EBL system. (d) Henniker Plasma HPT-200 plasma treatment system. (e) Oxford Instruments PlasmaPro 80 Cobra ICP RIE. (f) SUSS Mircortech MU84 mask aligner. (g) Kulicke and Soffa Model 4526 wirebonder. (h) Karl Suss mask aligner. (i) Everbeing C Series probe station. (j) Chemical vapor deposition system: Cabolite EVT12300B-23SN tube furnace, equipped with one Alicat MC-2SLPM-D/5M/5IN mass flow controller for argon, and three MC-1SLPM-D/5M/5IN mass flow controllers for hydrogen and methane.

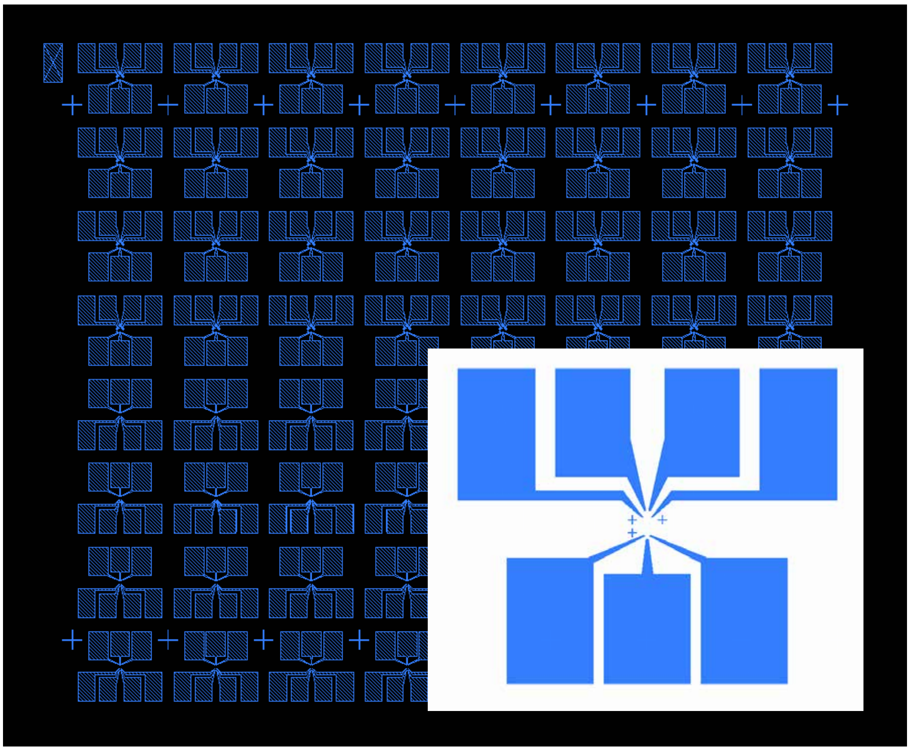

Figure 3.18: Schematic of the mask design used to pattern bonding pads and global markers. The design includes 64 devices as well as global alignment markers. The inset shows a magnified view of one of the devices.

3.3.2 Device Chip Fabrication

Lithography

The device chip was fabricated using designs adapted from Ref. [120]. A 10 mm × 10 mm silicon chip with a 300 nm thermally grown layer of SiO_2 served as the base substrate for the fabrication process. Each chip contained 64 devices.

Bonding pads and global markers were created using standard photolithographic techniques. The full recipe including the deposition and lift-off stages can be found in Appendix B. Fig. 3.18 shows the photolithography mask design used to define the chip's bonding pads and global alignment markers. Fig 3.19a shows an optical microscope image of a single device chip following photolithography, deposition and lift-off. Ti/Au (5/35 nm) gates are clearly visible on the SiO_2 substrate. The gates and source and drain electrodes were patterned using EBL. This stage of the fabrication process was carried out exclusively by Dr. Yikai Yang; however, a description of the process is included here

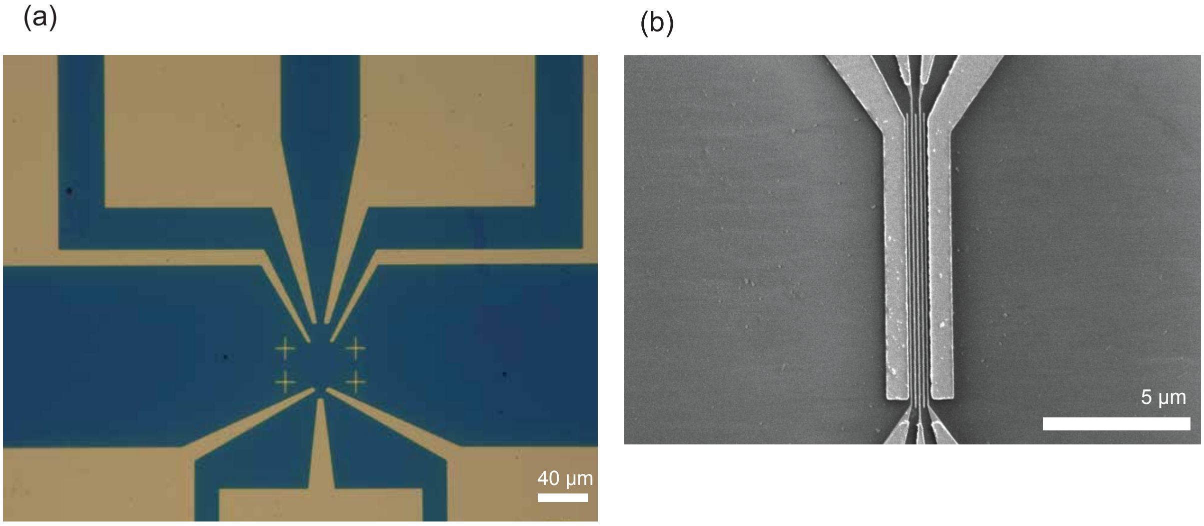

Figure 3.19: Optical and ebeam lithography (a) An optical microscope image of the bonding pads of a device patterned using the optical lithography process described in Section 3.3.2. (b) An SEM image of the source, drain and gate of a device patterned using the EBL process described in Section 3.3.2

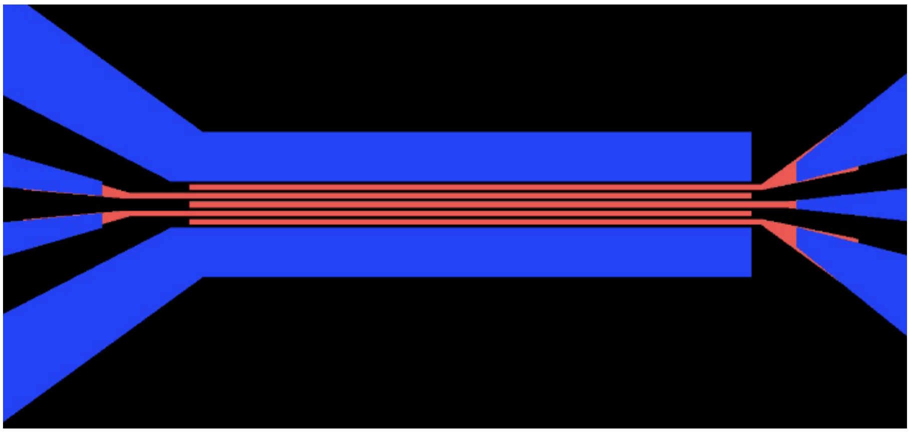

Figure 3.20: Pattern used to expose source, drain and gates during EBL. Source, drain and contact pads are in blue and gates in red.

for completeness. The recipes used are given in Appendix B, and details of the specific equipment (E-beam, mask aligner, plasma cleaner and ebeam evaporator) used can be found in Fig. 3.17 and its associated caption. The pattern used to expose the gates and source drain electrodes is shown in Fig. 3.20. Gates are shown in red and source and drain electrodes are shown in blue. An SEM image of the device following the EBL stage is shown in Fig. 3.19b.

This image has been removed the publicly available version of this thesis due to copyright restrictions

Figure 3.21: Schematic showing the bi-layer lift-off process. (a) Coat and soft-bake LOR. (b) Coat and soft-bake photoresist. (c) Expose the resist. (d) Develop imaging photoresist and LOR creating an undercut sidewall profile. (e) Deposit metals. Undercut profile results in discontinuous deposition. (f) Perform lift-off leaving a clean realisation of the desired pattern. Figure adapted from Ref. [63]

Refining lift-off

In refining the lithography recipes described above, we found the lift-off process to require significant optimisation. Initial attempts often resulted in the destruction of smaller features. To address this, we investigated the use of a bi-layer lift-off technique. Ultimately, we were able to achieve successful lift-off using a single layer of resist in combination of warm acetone and gentle sonication. Nevertheless, a description of the bi-layer method is included here for completeness. A schematic of the process is shown in Fig. 3.21. In bi-layer lift-off, the substrate is coated with two different resists that are immiscible with one another. The bottom resist is chosen for its slower and controllable dissolution rate, which allows for the formation of an undercut profile. This undercut plays a critical role during metal deposition by preventing the metal from forming continuous sidewalls between the patterned features and the surrounding resist. As a result, the metal is more cleanly separated during lift-off, reducing the likelihood of features being pulled off the substrate. An example bi-layer lift-off recipe is detailed in Appendix B.

3.3.3 Carbon Nanotube Growth

CNTs were grown using the well established chemical vapor deposition (CVD) method [65, 70]. During a typical CVD process for CNT growth, a catalyst material is heated to high temperatures, generally in the range of 500 to 1000 °C, within a tube furnace. During this process, a hydrocarbon gas is introduced into the reaction chamber and flows over the catalyst for a given duration. The catalyst typically consists of transition metal nanoparticles such as Ni, Co, Fe or metal salts [84], which are often dispersed on high-surface-area support materials such as porous alumina (Al_2O_3). The growth mechanism involves catalytic decomposition of the hydrocarbon molecules at the surface of the metal particles. Carbon atoms resulting from this decomposition dissolve into the metal, gradually saturating the particle. Once saturated, carbon precipitates out of the nanoparticle and assembles into tubular graphitic structures forming the CNT [31].

Catalyst preparation

The catalyst used in this work was adapted from Ref. [120] and consisted of a methanol suspension of Al_2O_3 nanoparticles (0.375 mg/mL), $Fe(NO_3)_3 \cdot 9H_2O$ (0.5 mg/mL), and $MoO_2(acac)_2$ (0.113 mg/mL). The high temperatures attained during CVD causes $Fe(NO_3)_3 \cdot 9H_2O$ to undergo thermal decomposition to form iron oxide (Fe_2O_3) nanoparticles [84, 106], which act as the active catalytic sites from which the CNTs grow. The Al_2O_3 nanoparticles serve as a support material for the catalyst. Their primary role is to ensure uniform distribution of the catalyst over the substrate surface and to suppress sintering during the high-temperature CVD process [55]. The inclusion of $MoO_2(acac)_2$ improves the dispersion of the iron catalyst and contributes to more uniform and higher-yield CNT growth [62].

Patterning quartz chip

CNTs were grown on polished quartz chips. Quartz was used as a substrate for two reasons. Firstly, it is transparent, allowing it to be aligned with the device chip during the stamping process (see Section 3.3.4 below). Secondly, quartz is composed of crystalline SiO_2, which has been shown to promote the reduction of iron oxide in an Fe-Al_2O_3 catalyst aiding the generation of Fe nanoparticles on the surface of the substrate [125].

Quartz chips were patterned with 6 μm pillars using reactive ion etching. Starting from a 4 inch wafer, a negative photoresist was applied. The wafer was exposed through a photomask containing a grid of 10 mm by 10 mm chips, each comprising 64 sets of pillars as well as a set of markers positioned to align with the global markers on the device chip. The chip geometry was designed to ensure compatibility with device chips during the stamping process (see Fig. 3.24). The pillars were then etched using Inductively Coupled

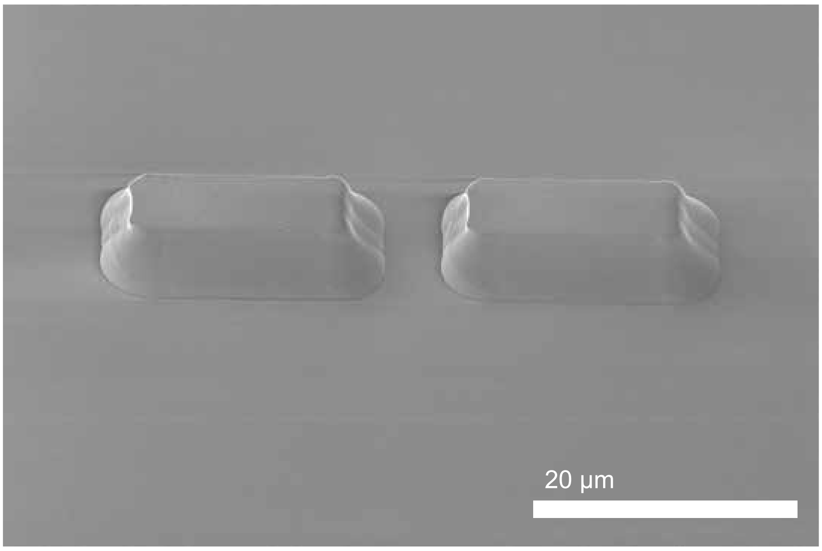

Figure 3.22: SEM image showing quartz pillars protruding from the substrate following ICP-RIE etching.

Plasma Reactive Ion Etching (ICP-RIE) (see Fig. 3.17(e)) using the recipe detailed in Appendix B. Fig. 3.22 shows an SEM image of quartz pillars protruding from the substrate following the ICP-RIE process.

Catalyst deposition

Growing CNTs between the pillars of the quartz chip requires the catalyst to be deposited exclusively on the tops of the pillars. This was accomplished by first coating the chip with a layer of resist thinner than the pillar height then depositing the catalyst across the entire chip. Finally, the resist was removed, resulting in a coating of catalyst on the tops of the pillars and nowhere else. The full recipe is detailed in Appendix B.

Chemical vapour deposition

CNTs were grown via chemical vapour deposition (CVD) in a tube furnace (see Fig. 3.17(j)) using CH_4 as a source of carbon. As described above, the CVD process promotes the vertical growth of CNTs from iron nanoparticle catalysts. To ensure that the CNTs bridge two adjacent pillars, the quartz chip was aligned such that the direction of gas flow in the furnace was parallel to the axis connecting each pair of pillars. Initially, the CNTs grow vertically from the catalyst particles. As growth continues, they fall over in the

CH_4 flow rate (sccm)	Single CNT devices (%)
400	14
300	18
220	33
210	28
200	21

Table 3.1: Percentage of single CNT devices obtained at different CH_4 flow rates. Each value corresponds to a single CVD growth run with a growth time of 1 hour.

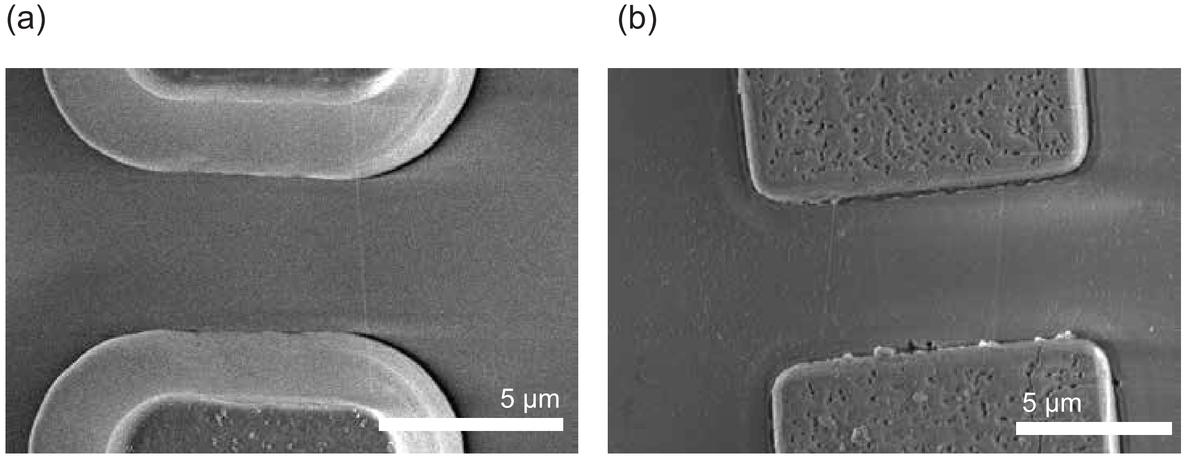

Figure 3.23: SEM images showing the growth of CNTs between quartz pillars. (a), A single CNT suspended between pillars following growth with a CH_4 flow rate of 220 sccm for 1 hour. (b), Two CNTs suspended between pillars following growth with a CH_4 flow rate of 1300 sccm for 1 hour.

direction of the gas flow, forming suspended bridges between neighbouring pillars [120].

A single quartz chip contains 64 pairs of pillars. During growth it is not uncommon for pillars to be spanned by multiple CNTs. The resulting devices, which can also consist of multiple suspended CNTs, are unsuitable for experiments. Moreover, the stamping process does not guarantee that a CNT suspended between two pillars will be successfully transferred to a device chip. The number of CNTs suspended between each pair of pillars can be controlled by adjusting the flow rate of CH_4 during the CVD process. Table 3.1 details the affect of flow rate on the percentage of single CNT devices on a given chip. From these results we concluded a CH_4 flow rate of 220 sccm to be optimal. The number of CNTs per pillar pair was quantified by imaging the samples in an SEM. Fig. 3.23 shows examples of both single and multiple suspended CNTs. The CVD process consists of two main stages. Firstly, with the furnace at 950°C, the quartz chip is exposed to a H_2/Ar gas mixture, which reduces the Fe_2O_3 formed by the thermal decomposition of

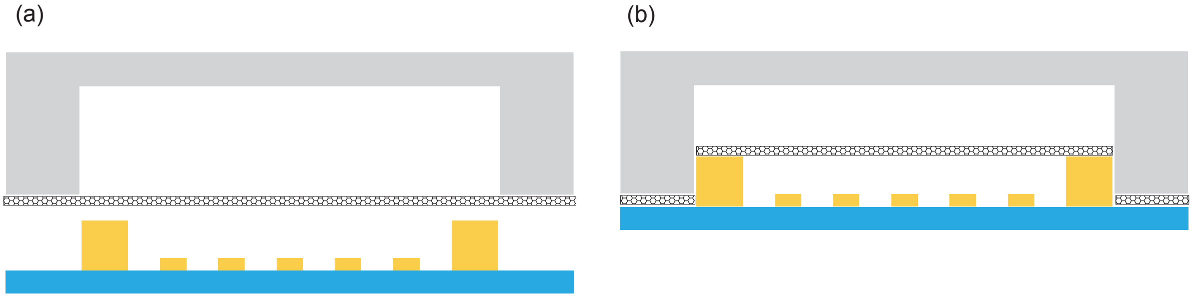

Figure 3.24: Schematics of the stamping process. (a), The device and quartz chips are aligned using global markers patterned on both chips. (b), The device chip is raised until it makes contact with the quartz chip. At this point, the CNT adheres to the source and drain electrodes, and its ends are severed by the edges of the quartz chip.

$Fe(NO_3)_3$ to metallic Fe via the reaction:

$$Fe_2O_3 + 3H_2 \rightarrow 2Fe + 3H_2O. \tag{3.31}$$

Secondly, the gas is switched to a CH_4/H_2 mixture, to precipitate the growth of CNTs. The complete CVD recipe, including optimised flow rates and growth duration, is detailed in Appendix B.

3.3.4 Stamping

CNTs were transferred from the quartz growth chip to the device chip using the stamping method described in Refs. [120, 124]. To improve electrical contact quality, the device chips were cleaned using an oxygen plasma treatment prior to stamping. The stamping process was performed using an optical mask aligner (see Fig. 3.17h). The quartz chip containing CNTs was mounted onto a blank glass mask using PMMA as an adhesive, while the device chip was secured to the sample stage with a vacuum. The sample stage was gradually raised whilst the chips were brought into precise alignment using the global makers on the quartz and device chips. Fig. 3.24 shows a schematic of this process. The height of the quartz pillars (6 μm) was greater than the height of the source and drain contacts on the device chip (100 nm), and the spacing between adjacent pillars (5 μm) exceeded the width of the gate structure (2.4 μm). This geometry ensured that initial contact occurred between the suspended CNTs and the source/drain electrodes. Upon

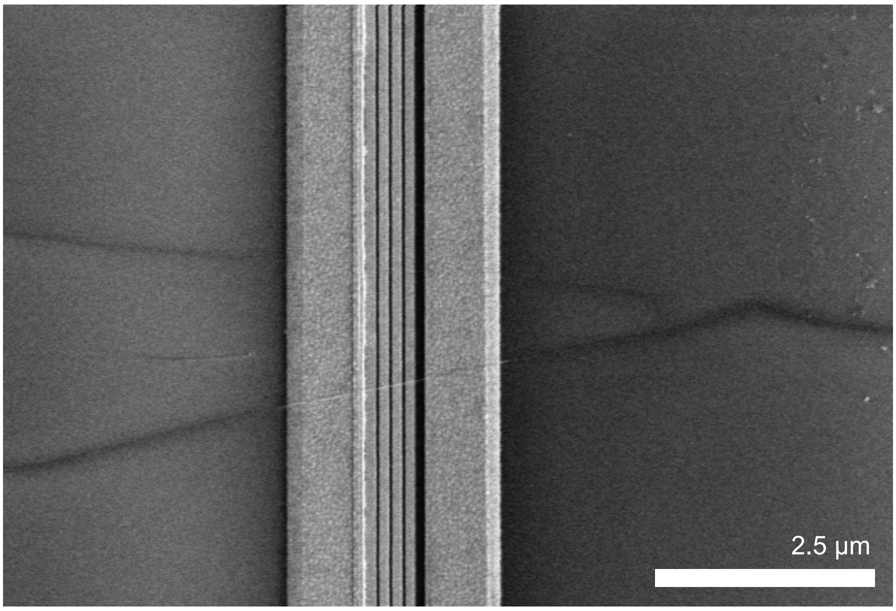

Figure 3.25: SEM of suspended CNT device. The image shows a CNT suspended between source and drain electrodes positioned above underlying gate electrodes. The CNT was transferred using the stamping method described above.

contact, the CNTs adhere to the metal electrodes through van der Waals interactions. Further upward motion of the sample stage caused the quartz pillars to contact the substrate, effectively "clipping" the CNTs at the pillar edges and completing the transfer. A schematic illustration of the process is shown in Fig. 3.24 and an SEM image of a CNT suspended above the gate architecture is shown in Fig. 3.25.

3.3.5 Device Characterisation

Once stamped, the resistance of the 64 individual devices of a device chip were measured using a probe station (Fig. 3.17i) via a two probe resistance measurement. Previous work in the group found that tunable devices typically exhibited room-temperature resistances of ~ 100 kΩ, consistent with values reported in Ref. [118], where this resistance is attributed primarily to the contact resistance between the CNT and the gold source/drain electrodes. Devices displaying resistance in this range, typically no more than 10% of those stamped, were subsequently imaged using an SEM to verify that the observed resistance was not due to multiple CNTs spanning the device or defects in the gate architecture. It has been shown that low-energy electron beams do not introduce disorder into the electronic spectrum a CNT [21,27]. However, bombarding the substrate of the device chip can lead to trapped charge, which may have a detrimental effect on the electrostatic potential landscape experienced by the CNT. Indeed, disorder in the substrate is believed to be a primary source of charge noise in CNT devices [27,69]. To minimize these effects, imaging was performed at a low accelerating voltage of 2 kV and conducted as quickly as possible. Following room-temperature characterization, a promising device was selected from the chip, loaded into a cryostat and cooled to a base temperature of approximately 20 mK for further testing.

Unfortunately, the time constraints imposed by my DPhil required that I transition away from CNT fabrication before an experimentally viable device could be obtained, in order to focus on the experiment detailed in Chapter 4. However, at the time of writing, fabrication efforts are ongoing, and usable devices are beginning to be produced.

4

Beyond Landauer: Non-Equilibrium Corrections to Information Erasure in a Quantum Dot

Contents

In the following chapter, the derivation leading up to Eq. 4.9 represents the author's extension of the model presented in Ref. [36] to the case of a two-fold degenerate QD. The derivation leading to Eqs. 4.26 and 4.29 was originally formulated by Joe Dunlop, with the derivations leading to equations 4.50 and 4.51 representing the author's extension of this work to the two-fold degenerate case.

4.1 Introduction

We saw in Section 2.2 how Rolf Landauer argued that the logically irreversible manipulation of information is a dissipative process. We saw that the process of performing the logically irreversible RESET TO ONE operation (or equivalently RESET TO ZERO operation) must be accompanied by the dissipation of at least $k_B T \ln 2$ of heat, where T is the temperature of the environment into which the heat is dissipated. We noted that performing the RESET TO ONE and RESET TO ZERO operations so as to dissipate the minimum possible heat has come to be known as Landauer erasure (LE) and this minimum, $k_B T \ln 2$, as the Landauer bound (LB). In addition we showed that at least $k_B T \ln 2$ of work must be performed in order to carry out LE.

Today, the energetic cost of computation is of increasing practical concern. Information technology accounts for approximately five percent of the global energy supply, with data centres alone consuming more energy than many individual nations [47]. While the LB provides a theoretical minimum for the energy cost of erasing a bit of information, current silicon-based digital circuits operate at energy scales many orders of magnitude above this limit, typically requiring hundreds of k_BT per logic operation [32]. Nonetheless, reducing the energetic cost of computation is an active area of research. Novel approaches, such as reversible [43, 44] and thermodynamic [78] computing, have been proposed as ways to drastically reduce the cost of computation and recent advances in semiconductor technology have enabled transistors to operate with 30% less power consumption than the minimum predicted for traditional silicon-based chips [59].

The LB is reached when the system encoding the information remains in equilibrium with its environment as erasure is performed. At a minimum, maintaining equilibrium requires any manipulation of the system to be performed quasistatically, rendering any information processing device operating at the LB impractical for real-world applications. Finite-time erasure has been studied experimentally in a number of physical systems including an underdamped micromechanical oscillator [30] and an overdamped colloidal particle in a double well potential [10, 12, 61]. Theoretical studies of finite-time erasure have been conducted across a range of settings, including systems governed by classical Langevin dynamics [100], strong system–environment coupling [92], and regimes where quantum coherence plays a role [114]. Additionally, a number of studies have focused on designing optimal protocols for finite-time erasure [1, 34, 87, 88, 94, 128].

Although finite-time erasure is necessary for practical information processing, it is not sufficient. Electronic components typically require a potential difference to operate. Thermodynamically, this requires the device to be coupled to reservoirs with different electrochemical potentials, introducing non-equilibrium processes beyond those present in the finite-time case. An experimental investigation into the effect of multiple reservoirs on the work cost of erasure was hitherto absent.

In this Chapter, we address this gap by measuring the work cost of erasing a single bit of information encoded in the charge occupancy of a QD coupled to source and drain electrodes whose relative electrochemical potentials can be tuned. We investigate how the work cost changes as the erasure process departs from the idealised quasistatic, single reservoir case considered by Landauer. Our results show how intrinsic physical properties of the system, such as tunnel rates and energy level degeneracy, introduce asymmetries in the work cost to erase to zero and one, with these asymmetries becoming more pronounced as erasure departs from the idealised case. We observe a finite-time correction to the work cost that scales inversely with the erasure time in line with previous studies. Extending these results to include an additional reservoir, we find that the finite-time correction remains independent of the relative electrochemical potential of the two reservoirs.

4.2 Information Processing in a Quantum Dot

In this section we derive expressions for the work cost of erasure in a two-fold degenerate QD system. The QD is coupled to source and drain reservoirs whose relative electrochemical potentials can be tuned, allowing the effect of an additional reservoir on the work cost of erasure to be studied. The derivations build on the work of Ref. [36], where the impact of an additional reservoir on the work cost of erasure was examined in the context of a non-degenerate QD system under quasistatic driving. Here, we extend these results by considering the impact of both an additional reservoir and finite-time driving on a two-fold degenerate QD system.

4.2.1 Landauer erasure in a quantum dot

We can encode a single bit of information in the charge occupancy of a QD, with unoccupied and occupied states of the dot encoding logical zero and logical one respectively. An energy space representation of the QD is shown in Fig. 4.1. In line with the description given in Section 3.1.1, the QD with electrochemical potential μ is coupled to source and drain electrodes whose electronic occupancies are described by Fermi functions parametrised by a temperature T and electrochemical potentials μ_S and μ_D. The coupling between the QD and reservoirs is parametrised by tunnelling rates Γ_S and Γ_D. The electrochemical potential of the dot can be manipulated by applying a voltage V_G to

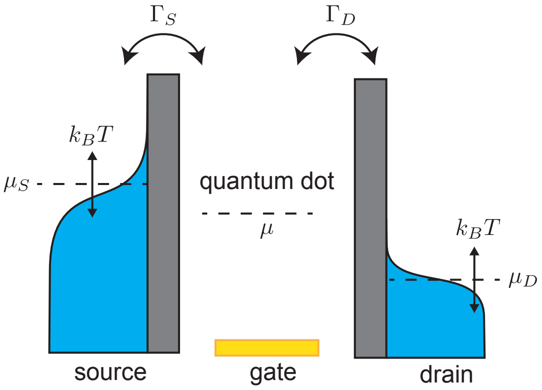

Figure 4.1: Energy space representation of a QD. A spin degenerate energy level μ is coupled to source and drain electrodes with electrochemical potentials μ_S and μ_D, and temperatures T. The dot exchanges charge with the source and drain at rates Γ_S and Γ_D. The energy level of the dot can be adjusted using a voltage applied to a gate electrode.

a nearby gate electrode. In Section 4.3.2 below we will show that, for the experimental device considered in this work, the energy level of the QD is two-fold degenerate. In addition we will see that $\hbar\Gamma \ll k_BT$, where $\Gamma = \Gamma_S + \Gamma_D$, allowing us to neglect the effect of lifetime broadening in the following analysis. The bias across the QD, $\Delta\mu_{S,D} = \mu_S - \mu_D$ and the thermal broadening of the source and drain electrodes, k_BT define two characteristic energy scales, E_{bias} and E_{therm}, which, as we shall see, can be used to characterise erasure in the QD system. We follow [36] and introduce the following protocol for erasing the information encoded in the charge occupancy of the QD:

1. Prime the dot for erasure by initialising μ at a value $\mu_{\frac{1}{2}}$ such that the steady-state occupation probability of the dot $p_{ss}(\mu_{\frac{1}{2}}) = 0.5$.

2. Erase to zero (one) by linearly ramping μ from $\mu_{\frac{1}{2}}$ to μ_0 (μ_1) over a time τ_{ramp}, such that the steady state occupation probability of the dot becomes $p_{ss}(\mu_0) = 0$ ($p_{ss}(\mu_1) = 1$).

3. Reset the dot to its initial configuration by ramping μ back to $\mu_{\frac{1}{2}}$ from μ_0 (μ_1). This reset must be performed sufficiently quickly to ensure that the charge occupation of the dot does not change and the QD returns to $\mu_{\frac{1}{2}}$ with a well defined charge occupation.

4.2.2 Quasistatic erasure

The erasure protocol described above is carried out quasistatically when the duration of the linear ramp, τ_{ramp}, is much longer than the characteristic equilibration time of the dot $\tau_{\mathrm{eq}} = \frac{1}{\Gamma}$. Here, τ_{eq} represents the time taken for the charge occupancy of the QD to reach a steady state. In this regime the dot remains in a steady-state throughout the second stage of the erasure process, with its charge occupation tracking its steady-state value. If the dot is occupied, work must be performed by the external circuit to change V_G and effect a change of its electrochemical potential. Specifically, for an occupied dot, a change in the electrochemical potential $d\mu$ corresponds to an amount of work dW being performed. Conversely, if the dot is unoccupied no work is done. When erasing to zero, the work done over the second stage of the erasure protocol is therefore given by

$$W^0 = \int_{\mu_{\frac{1}{2}}}^{\mu_0} p_{ss}(\mu) d\mu. \tag{4.1}$$

The final reset stage of the erasure process takes μ from μ_0 to $\mu_{\frac{1}{2}}$ with the dot unoccupied throughout. No work is done during this process such that the total work done when erasing to zero is given by Eq. 4.1. When erasing to one the work done during the second stage of the erasure protocol is given by

$$W = \int_{\mu_{\frac{1}{2}}}^{\mu_1} p_{ss}(\mu) d\mu. \tag{4.2}$$

The reset phase of the erasure protocol takes μ from μ_1 to $\mu_{\frac{1}{2}}$ with the dot occupied throughout. The total work done when erasing to one is therefore given by

$$\begin{aligned} W^1 &= \int_{\mu_{\frac{1}{2}}}^{\mu_1} p_{ss}(\mu) d\mu + \int_{\mu_1}^{\mu_{\frac{1}{2}}} d\mu \\ &= \int_{\mu_1}^{\mu_{\frac{1}{2}}} (1 - p_{ss}(\mu)) d\mu. \end{aligned} \tag{4.3}$$

For a QD with a two-fold degenerate level and electrochemical potential μ, the electron currents in and out of the dot are given by

$$\begin{aligned}
\Gamma_S^{\text{in}} &= 2\Gamma_S f_S(\mu)(1 - p_{ss}(\mu)), \\
\Gamma_S^{\text{out}} &= \Gamma_S(1 - f_S(\mu))p_{ss}(\mu), \\
\Gamma_D^{\text{in}} &= 2\Gamma_D f_D(\mu)(1 - p_{ss}(\mu)), \\
\Gamma_D^{\text{out}} &= \Gamma_D(1 - f_D(\mu))p_{ss}(\mu)),
\end{aligned} \tag{4.4}$$

where $f_{S,D}(\mu)$ are the Fermi functions of the source and drain electrodes given by

$$f_{S,D}(\mu) = \frac{1}{1 + e^{\beta(\mu - \mu_{S,D})}}, \tag{4.5}$$

where $\beta^{-1} = k_B T$. The factor of 2 in the expressions for Γ_S^{in} and Γ_D^{in} account for the fact that, in a two-fold degenerate system, there are two channels by which an electron can tunnel into the dot. The factor of 2 is missing in the expressions for Γ_S^{out} and Γ_D^{out} since Coulomb blockade dictates that only one electron can occupy the dot at a time. Once occupied, there is only one electron available to tunnel out, and therefore only a single outgoing channel. Steady-state occupation is achieved when the condition

$$\Gamma_S^{\text{in}} + \Gamma_D^{\text{In}} = \Gamma_S^{\text{out}} + \Gamma_D^{\text{out}} \tag{4.6}$$

is satisfied, which allows us to write

$$p_{ss}(\mu) = \frac{2\Gamma_S}{\gamma(\mu)} f_S(\mu) + \frac{2\Gamma_D}{\gamma(\mu)} f_D(\mu), \tag{4.7}$$

where

$$\gamma(\mu) = \Gamma_S(1 + f_s(\mu)) + \Gamma_D(1 + f_D(\mu)). \tag{4.8}$$

For $\Delta\mu_{S,D} = 0$ Eq. 4.7 reduces to

$$p_{ss}(\mu) = \frac{2f(\mu)}{1 + f(\mu)}, \tag{4.9}$$

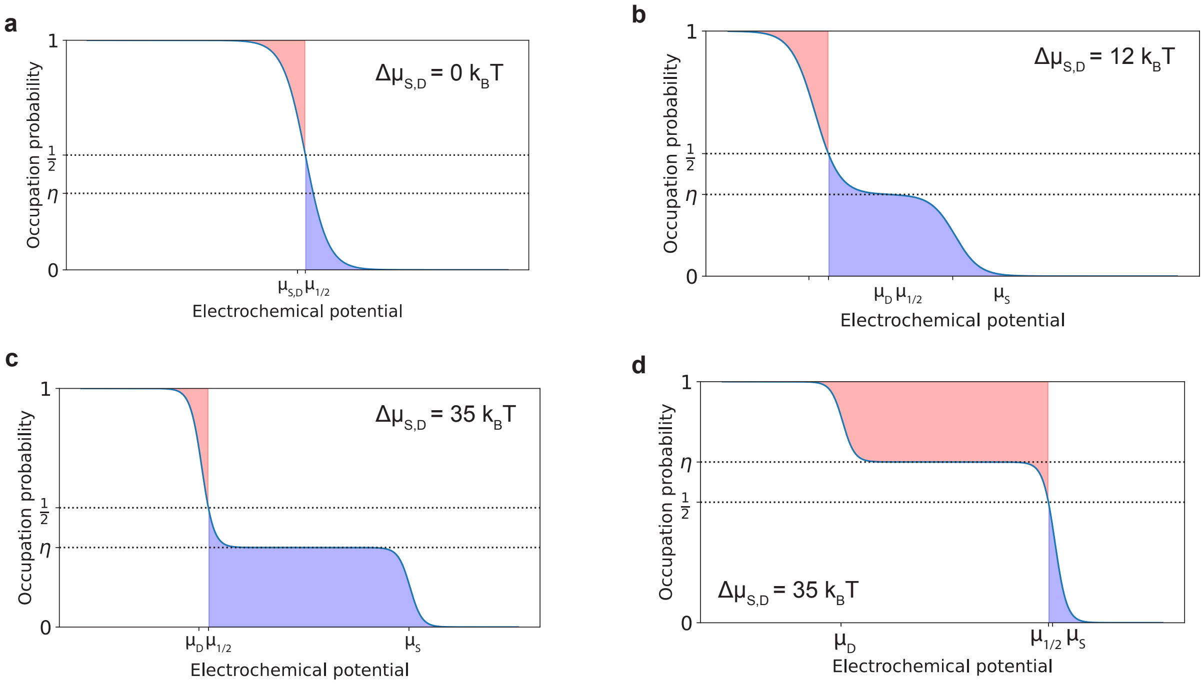

Figure 4.2: Eq. 4.7 plotted for increasing values $\Delta\mu_{S,D}$. Red regions represent the work required to erase to one and blue regions the work required to erasure to zero. (a), (b), (c), $\frac{\Gamma_D}{\Gamma_S} = 0.25$, giving $\eta < 0.5$, (d) $\frac{\Gamma_D}{\Gamma_S} = 1$, giving $\eta > 0.5$.

and erasure takes place in the context of the conventional Landauer framework of a system coupled to a single thermal reservoir. The system is in equilibrium throughout the erasure process and Eqs. 4.1 and 4.3 recover the familiar LB with $W^0 = W^1 = k_BT\ln 2$. In Fig. 4.2 we set $\mu_D = 0$ and plot $p_{ss}(\mu)$ for four values of μ_S. Red regions represent the work cost to reset to one, W^1, and blue regions represent the work cost to reset to zero, W^0. For $|\mu_S| > 0$ the system is coupled to two reservoirs at different chemical potentials, the system is no longer in equilibrium as erasure is performed and both W^0 and W^1 are greater than $k_BT\ln 2$. If the tunnelling rates Γ_S and Γ_D are not equal an asymmetry develops between W^0 and W^1 as μ_S is increased. Since efficient information encoding requires zeros and ones to occur with equal frequency [102], we follow [36] in taking the average work cost, $\overline{W} = \frac{1}{2}(W^0 + W^1)$, as a suitable measure of the work cost in the presence of this asymmetry.

The origin of the asymmetry becomes apparent if we consider $p_{ss}(\mu)$ when $\Delta\mu_{S,D} \gg k_BT$. In this regime $p_{ss}(\mu)$ resembles the sum of two step functions with a plateau at

$p_{ss} = \eta$ where

$$\eta = \frac{2}{2 + \frac{\Gamma_D}{\Gamma_S}}. \tag{4.10}$$

This is approximately the case in Fig. 4.2c where where $p_{ss}(\mu)$ is plotted for $\Delta\mu_{S,D} = 35k_BT$. In the figure we have $\eta < 0.5$ and $\mu_D \approx \mu_{\frac{1}{2}}$ such that the work required to erase to one is small ($W^1 \approx 0$). Conversely, erasure to zero involves rasing μ from approximately μ_D to μ_S with a near constant occupation probability of $\eta = 0.25$, giving $W^1 \approx \eta(\mu_D - \mu_S)$. In contrast, when $\eta > 0.5$ (4.2d) we have $W^1 \approx 0$ and $W^0 \approx \eta(\mu_S - \mu_D)$. In the limit that $T \to 0$ these approximations become exact, as we will now show.

4.2.3 Erasure classification and the zero temperature limit

In the limit that $T \to 0$ the steady state occupation probability of the QD (Eq. 4.7) becomes

$$\lim_{T\to 0} p_{ss}(\mu) = \frac{2\Gamma_S\,\Theta(\mu_S - \mu) + 2\Gamma_D\,\Theta(\mu_D - \mu)}{\Gamma_S\Big[1 + \Theta(\mu_S - \mu)\Big] + \Gamma_D\Big[1 + \Theta(\mu_D - \mu)\Big]}, \tag{4.11}$$

where Θ is the Heaviside step function. Eq. 4.11 is the sum of two step functions with a plateau at η

$$\lim_{T\to 0} p_{ss}(\mu) = \begin{cases} 1, & \mu < \mu_D, \\ \eta, & \mu_D < \mu < \mu_S, \\ 0, & \mu > \mu_S, \end{cases} \tag{4.12}$$

where

$$\eta = \frac{2}{2 + \frac{\Gamma_D}{\Gamma_S}}. \tag{4.13}$$

For $\eta < 0.5$, $\mu_{1/2}$ approaches μ_D as $T \to 0$, implying that $W^1 \to 0$. If we define μ_η as the value of μ for which $p_{ss}(\mu_\eta) = \eta$, then in the limit $T \to 0$ the points $\mu_{1/2}$ and μ_η coincide, such that $W^0 \to \eta\,\Delta\mu_{S,D}$. The average erasure cost then becomes $\overline{W} = \frac{1}{2}\eta\Delta\mu_{S,D}$. Conversely for $\eta > 0.5$ we have $W^0 \to 0$ and $W^1 \to (1-\eta)\Delta\mu_{S,D}$, giving $\overline{W} = \frac{1}{2}(1-\eta)\Delta\mu_{S,D}$. As $\Delta\mu_{S,D}$ becomes increasingly large compared to k_BT, we can approximate $p_{ss}(\mu)$ with its value at the zero temperature limit. In this bias dominated regime we have $E_{\text{bias}} \gg E_{\text{therm}}$, and the average work cost can be approximated by

$$\overline{W}_{\text{bias}}(\Delta\mu_{S,D}) = \begin{cases} \frac{1}{2}\eta\Delta\mu_{S,D} & \text{for } \eta < 0.5 \\ \frac{1}{2}(1-\eta)\Delta\mu_{S,D} & \text{for } \eta > 0.5. \end{cases} \tag{4.14}$$

We classify erasure in the QD system according to whether temperature or bias dominate the erasure process. When $\overline{W}_{\text{bias}} > k_B T \ln 2$ we consider erasure to be bias dominated. Conversely, since $k_B T \ln 2$ represents a lower bound on the work cost of erasure, when $\overline{W}_{\text{bias}} < k_B T \ln 2$ the zero temperature approximation breaks down and we consider erasure to be temperature dominated.

4.2.4 Finite time erasure

In the previous section we derived expressions for the work cost of erasure in a two-fold degenerate QD system when erasure is carried out quasistatically. We now examine the effect of finite time driving on the work cost of erasure. Specifically, we show that the two-fold degeneracy of the QD system results in a further asymmetry between W^0 and W^1 when erasure is carried out in finite time. This prediction is a new theoretical result and constitutes an original contribution of this thesis.

To perform erasure to zero (one) we assume the electrochemical potential of the dot is ramped from $\mu_{\frac{1}{2}}$ to μ_0 (μ_1) between $t = 0$ and $t = \tau_{\text{ramp}}$ at a constant rate. The rates $\dot{\mu_0}$ and $\dot{\mu_1}$ at which erasure to zero and erasure to one are carried out are therefore given by

$$\dot{\mu_0} = \frac{\mu_0 - \mu_{\frac{1}{2}}}{\tau_{\text{ramp}}}, \quad \dot{\mu_1} = \frac{\mu_1 - \mu_{\frac{1}{2}}}{\tau_{\text{ramp}}}, \tag{4.15}$$

where $\mu_1 < \mu_{\frac{1}{2}} < \mu_0$. We also assume that the magnitude of the change in μ is the same when erasing to zero and one such that

$$\dot{\mu_0} = -\dot{\mu_1} = \frac{\Delta\mu}{\tau_{\text{ramp}}} \tag{4.16}$$

Eq. 4.16 describes the ramps used to perform erasure in the experimental portion of this work making the following analysis applicable to the experimental protocol described in Section 4.3.3 below. The linear nature of the ramps mean that μ is in one-to-one correspondence with t. In the absence of spin degeneracy, the master equation describing the occupation of the QD can therefore be written

$$\frac{dp}{dt} = \gamma_{\text{in}}(t)(1 - p(t)) - \gamma_{\text{out}}(t)p(t), \tag{4.17}$$

where $\gamma_{\text{in/out}}$ are effective tunnelling rates, given by

$$\gamma_{\text{in}} = \Gamma_S f_S(t) + \Gamma_D f_D(t), \qquad \gamma_{\text{out}} = \Gamma_S(1 - f_S(t) + \Gamma_D(1 - f_D(t)). \tag{4.18}$$

Here $\Gamma_{S,D}$ the tunnelling rates of the source and drain electrodes and $f_{S,D}(t)$ are the source and drain Fermi functions evaluated at the time-dependent electrochemical potential $\mu(t)$. Eq. 4.17 simplifies to

$$\frac{dp}{dt} = \Gamma \left[\frac{\Gamma_S}{\Gamma} f_S(t) + \frac{\Gamma_D}{\Gamma} f_D(t) - p(t) \right], \tag{4.19}$$

Where $\Gamma = \Gamma_S + \Gamma_D$. From Eq. 4.19 we see that $\frac{dp}{dt} = 0$ when

$$p(t) = \frac{\Gamma_S}{\Gamma} f_S(t) + \frac{\Gamma_D}{\Gamma} f_D(t), \tag{4.20}$$

such that the steady state occupation of the dot $p_{ss}(t)$ is given by

$$p_{ss}(t) = \frac{\Gamma_S}{\Gamma} f_S(t) + \frac{\Gamma_D}{\Gamma} f_D(t). \tag{4.21}$$

The master equation then becomes

$$\frac{dp}{dt} = \Gamma(p_{ss}(t) - p(t)). \tag{4.22}$$

The one-to-one correspondence between μ and t allows us to write $\frac{dp}{dt} = \dot{\mu}_0 \frac{dp}{d\mu}$. Rewriting

Eq. 4.17 as a function of μ and rearranging we therefore have

$$p(\mu) = p_{\mathrm{ss}}(\mu) - \frac{\dot{\mu}_0}{\Gamma}\frac{dp}{d\mu}. \tag{4.23}$$

The work cost of erasing to zero is given by

$$W^0 = \int_{\mu_{\frac{1}{2}}}^{\mu_0} p(\mu) d\mu. \tag{4.24}$$

From Eq. 4.23 we therefore have

$$W^0 = \int_{\mu_{\frac{1}{2}}}^{\mu_0} p_{\mathrm{ss}}(\mu)\, d\mu - \frac{\dot{\mu}_0}{\Gamma}\int_{\mu_{\frac{1}{2}}}^{\mu_0} \frac{dp}{d\mu}\, d\mu. \tag{4.25}$$

The first term in this expression is simply the quasistatic work cost W^0_{QS}. Moreover, in erasing to zero we have taken the occupation of the dot from $p = \frac{1}{2}$ to $p = 0$. The work cost therefore becomes

$$\begin{aligned} W^0 &= W^0_{QS} + \frac{\dot{\mu}_0}{2\Gamma} \\ &= W^0_{QS} + \frac{\Delta\mu}{2\Gamma\tau} \\ &= k_B T \ln 2 + b_0 + \frac{a}{\tau}, \end{aligned} \tag{4.26}$$

where $a = \frac{\Delta\mu}{2\Gamma}$ and b_0 is the excess work required to erase to zero in the presence of a bias. The work cost of erasing to one is given by

$$W^1 = \int_{\mu_1}^{\mu_{\frac{1}{2}}} (1 - p(\mu)) d\mu. \tag{4.27}$$

Substituting this in Eq. 4.1

$$W^1 = \int_{\mu_1}^{\mu_{\frac{1}{2}}} (1 - p_{\mathrm{ss}}(\mu))\, d\mu + \frac{\dot{\mu}_1}{\Gamma}\int_{\mu_1}^{\mu_{\frac{1}{2}}} \frac{dp}{d\mu}\, d\mu, \tag{4.28}$$

The first term of Eq. 4.1 is the quasistatic work cost W^1_{QS}. In erasing to one the occupation of the dot is taken from $p = \frac{1}{2}$ to $p = 1$ such that the work cost becomes

$$\begin{aligned} W^1 &= W^1_{QS} - \frac{\dot{\mu}_1}{2\Gamma} \\ &= W^1_{QS} + \frac{\dot{\mu}_0}{2\Gamma} \\ &= W^1_{QS} + \frac{\Delta\mu}{2\Gamma\tau} \\ &= k_B T \ln 2 + b_1 + \frac{a}{\tau}, \end{aligned} \tag{4.29}$$

where b_1 is the excess work required to erase to one in the presence of a bias. At zero bias we have $b_0 = b_1 = 0$. In the absence of a bias, when erasure is carried out in finite time, Eqs. 4.26 and 4.29 therefore predict that there should be no difference in the work costs required to erase to zero and one.

Taking into account spin degeneracy the master equation takes the same form as Eq. 4.17

$$\frac{dp}{dt} = \gamma_{\text{in}}(t)(1 - p(t)) - \gamma_{\text{out}}(t)p(t), \tag{4.30}$$

with the effective tunnelling rates γ_{in} and γ_{out} now given by

$$\gamma_{\text{in}} = 2\left[\Gamma_S f_S(t) + \Gamma_D f_D(t)\right], \qquad \gamma_{\text{out}} = \Gamma_S(1 - f_S(t) + \Gamma_D(1 - f_D(t)), \tag{4.31}$$

where the factor of 2 in front of γ_{in} accounts for the fact that there are now two states into which electrons can tunnel. At zero bias where $f_S(t) = f_D(t)$ the effective tunnelling rates become

$$\gamma_{\text{in}} = 2\Gamma f(t), \qquad \gamma_{\text{out}} = \Gamma(1 - f(t)), \tag{4.32}$$

where we now imagine the dot to be coupled a a single Fermionic reservoir with Fermi function $f(t)$. Substituting the zero bias effective tunnelling rates into Eq. 4.30 and rearranging gives

$$\frac{dp}{dt} = 2\Gamma f(t) - \Gamma(1 + f(t))p(t). \tag{4.33}$$

Adding and subtracting the term $\Gamma(1 + f(t))p_{ss}(t)$ to the left hand side of Eq. 4.33 allows us to write

$$\frac{dp}{dt} = \Gamma(1+f)(p_{ss} - p) + 2\Gamma f - \Gamma(1+f)p_{ss}, \tag{4.34}$$

where we have dropped the dependence on t for clarity. The occupation of the QD reaches a steady state when $\frac{dp}{dt} = 0$. From Eq. 4.34 we see that a necessary condition for this to occur is $p = p_{ss}$ from which we associate p_{ss} with the steady state solution. The steady state solution also requires that

$$2\Gamma f - \Gamma(1+f)p_{ss} = 0, \tag{4.35}$$

from which we obtain

$$p_{ss} = \frac{2f}{1+f}. \tag{4.36}$$

Substituting this into Eq. 4.34 we arrive at the following master equation for the occupancy of the QD at zero bias in the presence of spin degeneracy

$$\frac{dp}{dt} = \Gamma(1+f)(p_{ss} - p). \tag{4.37}$$

Considering erasure to zero, using the same argument used to derive Eq. 4.23, we can write

$$p(\mu) = p_{ss}(\mu) - \frac{\dot{\mu}_0}{\Gamma}\frac{1}{1+f(\mu)}\frac{dp}{d\mu}, \tag{4.38}$$

We can rewrite Eq. 4.38 as

$$\varepsilon g(\mu)p'(\mu) + p(\mu) = p_{ss}(\mu), \tag{4.39}$$

where

$$\varepsilon = \frac{\dot{\mu}_0}{\Gamma}, \qquad g(\mu) = \frac{1}{1+f(\mu)}. \tag{4.40}$$

We note that as $\dot{\mu}_0 \to 0$ the solution of Eq. 4.39 tends towards the steady state solution $p_{ss}(\mu)$. We therefore seek a perturbative solution to Eq. 4.38 of the form

$$p(\mu) = p_0(\mu) + \varepsilon p_1(\mu) + \varepsilon^2 p_2(\mu)... \tag{4.41}$$

Plugging Eq. 4.41 into Eq. 4.39 and comparing coefficients gives

$$p_0(\mu) = p_{ss}(\mu) \tag{4.42}$$

$$p_1(\mu) = -g(\mu)p'_{ss}(\mu). \tag{4.43}$$

To first order in ε the work cost of erasing to zero is then given by

$$W^0 = \int_{\mu_{\frac{1}{2}}}^{\mu_0} p_{ss}(\mu) - \varepsilon \int_{\mu_{\frac{1}{2}}}^{\mu_0} g(\mu)p'_{ss}(\mu)d\mu + \mathcal{O}(\varepsilon^2). \tag{4.44}$$

The first term of Eq. 4.44 is the quasistatic work cost W^0_{QS}. From Eq. 4.36 we have

$$p'_{ss}(\mu) = \frac{-2\beta f(\mu)(1-f(\mu))}{(1+f(\mu))^2}, \tag{4.45}$$

where $\beta = \frac{1}{k_B T}$. We therefore have

$$W^0 = W^0_{QS} + 2\beta\varepsilon \int_{\mu_{\frac{1}{2}}}^{\mu_0} \frac{f(\mu)(1-f(\mu))}{(1+f(\mu))^3} d\mu + \mathcal{O}(\varepsilon^2). \tag{4.46}$$

The integral can be solved by noting that

$$\frac{df}{d\mu} = -\beta f(\mu)(1-f(\mu)) \tag{4.47}$$

giving

$$W^0 = W^0_{QS} + \varepsilon \frac{1}{(1+f(\mu))^2}\Bigg|_{\mu_{\frac{1}{2}}}^{\mu_0} + \mathcal{O}(\varepsilon^2). \tag{4.48}$$

$\mu_{\frac{1}{2}}$ and μ_0 are defined such that

$$p_{ss}(\mu_{\frac{1}{2}}) = \frac{1}{2}, \qquad p_{ss}(\mu_0) = 0 \tag{4.49}$$

from which we see that $f(\mu_{\frac{1}{2}}) = \frac{1}{3}$ and $f(\mu_0) = 0$. We therefore have

$$W^0 = W^0_{QS} + \frac{a_0}{\tau_{\text{ramp}}} + \mathcal{O}(\varepsilon^2), \tag{4.50}$$

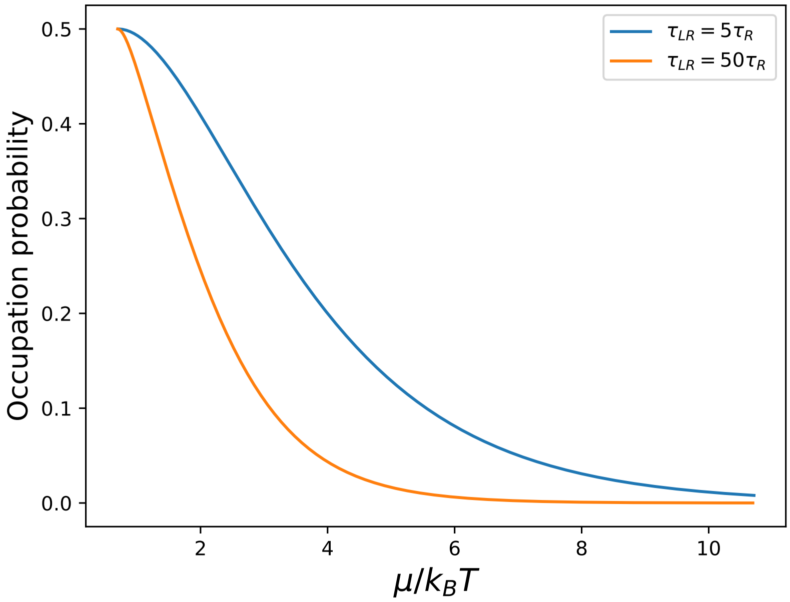

Figure 4.3: Dot occupation probability as a function of its electrochemical potential for erasure to zero. Blue and orange curves are computed via a numerical integration of Eq. 4.37. The orange curve represents the quasistatic case with $\tau_{\text{ramp}} = 50\tau_{\text{eq}}$. The blue curve represents the finite time case with $\tau_{\text{ramp}} = 50\tau_{\text{eq}}$.

where $a_0 = \frac{7}{16}\frac{\Delta\mu}{\Gamma}$. A similar analysis shows that

$$W^1 = W^1_{QS} + \frac{a_1}{\tau_{\text{ramp}}} + \mathcal{O}(\varepsilon^2), \tag{4.51}$$

where $a_1 = \frac{5}{16}\frac{\Delta\mu}{\Gamma}$. The form of Eqs. 4.50 and 4.51 are consistent with previous work [10, 30, 87, 92, 100, 114], where a terms proportional to τ_{ramp}^{-1} plus higher order corrections account for the additional work required to overcome dissipation that arises outside the quasistatic limit. In our system this excess work originates from the deviation of the dot's occupation probability from its steady-state value. The idea is illustrated in Fig. 4.3, where the dot occupation probability is plotted as a function of its electrochemical potential for erasure to zero for two different ramp lengths. We see that the occupation probability of the faster ramp ($\tau_{\text{ramp}} = 5\tau_{\text{eq}}$) lags the occupation probability of the slower ramp ($\tau_{\text{ramp}} = 50\tau_{\text{eq}}$), resulting in a larger work cost.

Since $a_0 \neq a_1$, Eqs. 4.50 and 4.51 predict an asymmetry between the work cost to erase to zero and the work cost to erase to one. This asymmetry was absent in the spin-degenerate case and can therefore be attributed to the presence of spin degeneracy.

Physically we can understand this asymmetry as follows. We saw above that when erasure is carried out quasistatically, such that the occupation of the dot tracks its steady state occupation, the work cost of erasing to zero and one are equal. Now consider a situation where erasure is carried out in finite time. Specifically, consider a case where erasure is carried out at a rate $\dot{\mu}^*$ such that over a time $t^* < \tau_{\mathrm{eq}}$ the electrochemical potential of the dot changes by an amount $\Delta\mu^* > k_B T$, where τ_{eq} is the characteristic relaxation time of the dot.

Consider erasure to zero. By ramping at $\dot{\mu}^*$ we are ensuring that after a time t^*, corresponding to a change in μ of $\Delta\mu^*$, there are effectively zero states in the source or drain available from which an electron can tunnel into the dot. If the ramp was initialised with the dot unoccupied, then we have succeeded in erasing to zero. However, if the ramp was initialised with the dot occupied we need to continue to ramp for a time t^0 until the electron leaves the dot. We call the distance over which this ramp takes place $\Delta\mu^0$. Therefore, in order to ensure that erasure to zero has taken place we need to ramp μ by a total amount $\Delta\mu^0_{\mathrm{tot}} = \Delta\mu^* + \Delta\mu^0$.

Now consider erasure to one. By ramping at $\dot{\mu}^*$ for a time t^* we have ensured that there are effectively zero states in the source or drain into which an electron initially on the dot can leave. As a result we can be certain that erasure has taken place is the dot was initially occupied. If the dot was initially unoccupied, we continue to ramp for a time t^1 until an electron tunnels into the dot. The distance over which μ travels in this time we call $\Delta\mu^1$. Therefore in order to ensure erasure to one has taken place we need to ramp μ by an amount $\Delta\mu^1_{\mathrm{tot}} = \Delta\mu^* + \Delta\mu^1$.

Crucially, in the presence of spin degeneracy there are two states into which electrons can tunnel into the dot, but only one from which the electrons leave. As a result, the time required for the electron to leave the dot when erasing to zero is greater than the time required for an electron to enter the dot when erasing to one, i.e. $t^0 > t^1$. Given the ramps are linear and symmetric this implies that $\Delta\mu^0_{\mathrm{tot}} > \Delta\mu^1_{\mathrm{tot}}$, which in turn implies that $W^0 > W^1$.

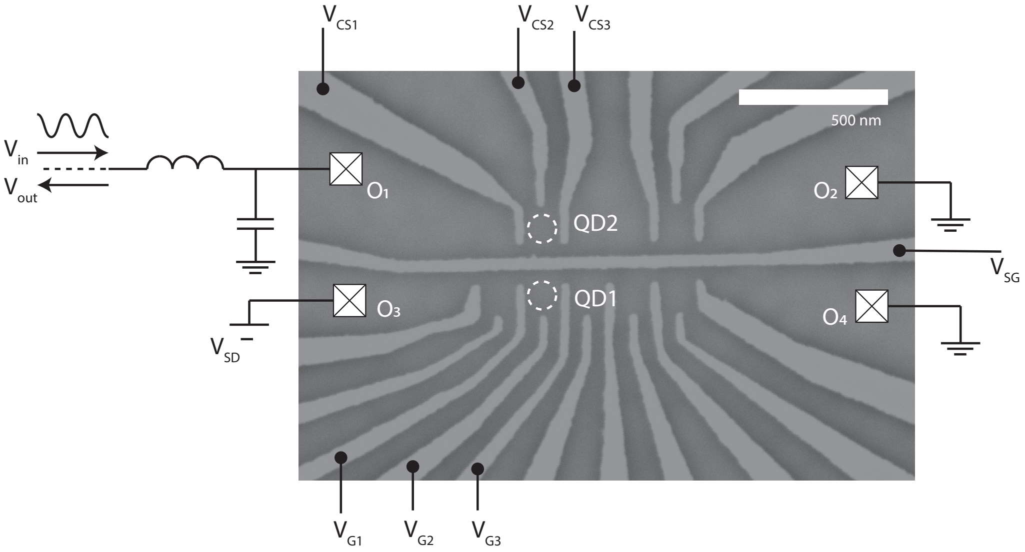

Figure 4.4: SEM image of the device used in the experiment. QD1 encodes the information erased in the experiment and is defined using voltages V_{G1-G3} with a bias V_{SD} applied via ohmic contact O_1. The charge-sensing QD, QD2, is tuned using gates $V_{CS1-CS3}$ and coupled to an RF cavity for charge sensing reflectometry. Couping between QD1 and QD2 is controlled using the splitter gate voltage V_{SG}. The cavity is probed with an RF signal V_{in}, and the reflected portion, V_{out}, is demodulated and measured to extract information concerning the occupancy of QD1.

4.3 Methods

In the previous section we saw how a QD can be used as a platform to investigate LE, with a focus on showing how the work cost of erasure deviates from the LB in the presence of an applied bias and finite time driving. In this section we present an experimental realisation of LE that allows these predictions to be tested.

4.3.1 Experimental setup

The device used in the experiment is shown in Fig. 4.4. A Ge/SiGe heterostructure con-

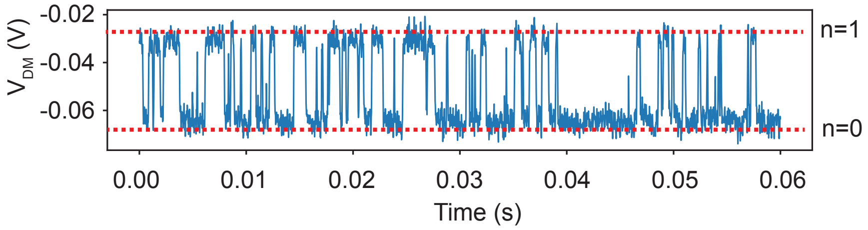

Figure 4.5: Demodulated voltage as a function of time from a charge sensing reflectometry measurement of QD2. The signal exhibits two distinct levels corresponding to the occupied ($n = 1$) and unoccupied ($n = 0$) charge states of QD1.

fines charge in a plane perpendicular to the growth direction, forming a two-dimensional hole gas (2DHG). Positive voltages applied to gates patterned on the surface of the heterostructure further confine the 2DHG allowing the formation of QDs in the lower (QD1) and upper (QD2) arrays of the device. The occupancy $n \in \{0, 1\}$ of a two-fold degenerate energy level in QD1, encodes the bit of information to be erased in the experiment. We manipulate the electrochemical potential of QD1, μ, with the plunger gate voltage V_{G2}, which has a lever arm of $\alpha = 0.048$ eV/V. QD1 is tunnel-coupled to two large regions of the 2DHG across which a bias V_{SD} can be applied. The result is the system shown in Fig. 4.1: a two-fold degenerate energy level coupled to fermionic source and drain reservoirs at temperature $T = 195$ mK, and electrochemical potentials μ_S and μ_D. A description of the methods used to extract α and T is provided in Section 5.5.1. A charge sensing QD (QD2) is integrated into an rf cavity and capacitively coupled to QD1. The cavity is probed with a reference signal V_{in}. The reflected signal V_{out} is sensitive to the occupation of QD1, giving a real-time measurement of n [115] (see section 3.2.2 for a full description of this measurement). Fig. 4.5 shows a typical time trace of the reflected signal after demodulation. A simplified schematic of the full experimental setup used to perform charge sensing reflectometry on QD2 is shown in Fig. 4.6. A lock-in amplifier generates the reference signal V_{out}. The reflected signal, V_{out} is transferred, via a directional coupler, to the input port of the lock-in amplifier, where it is mixed with the reference signal and low pass filtered to give the demodulated outputs V_{out}^x and V_{out}^y. The bias across the device dot (QD1) and sensor dot (QD2) are controlled using voltage sources V_{SD} and V_{CS} generated by a Delft IVVI rack. The current through the sensor dot can be measured using the current amplifier I_{CS}. Gate voltages are also generated using the IVVI rack; however, the lines directing these voltages to the sample are omitted from the figure for simplicity.

4.3.2 Parameter extraction

Occupation probability

Several key experimental parameters are determined by measuring the dot's occupation probability as a function of V_{G2}. Here we describe the procedure for performing this measurement.

To measure the occupation probability of QD1, transport must be slowed sufficiently for individual tunnelling events to be resolved by the measurement set up. This is achieved in the so called *latched* regime, where individual charge transport events are detected within the integration time of the charge sensing measurement. The latched regime is reached by adjusting the barrier gates V_{G1} and V_{G3} until individual tunnelling events can be resolved. Fig. 4.7a shows a transition between the occupied and unoccupied states of the dot in this regime. Once the device is tuned to a sufficiently slow regime, we proceed by sweeping V_{G2} across the transition, driving the dot from an occupied to an unoccupied state. At each gate voltage in the sweep, we measure the dot's charge occupation for two seconds. Fig. 4.7b shows a typical measurement. The measured voltages, V_{DM}, correspond to demodulated signals obtained via charge sensing reflectometry performed on QD2. The occupation probability of the dot at a given value of V_{G2} is estimated from the corresponding time trace using

$$p(V_{G2}) = \frac{t_{\mathrm{occ}}(V_{G2})}{t_{\mathrm{tot}}}, \tag{4.52}$$

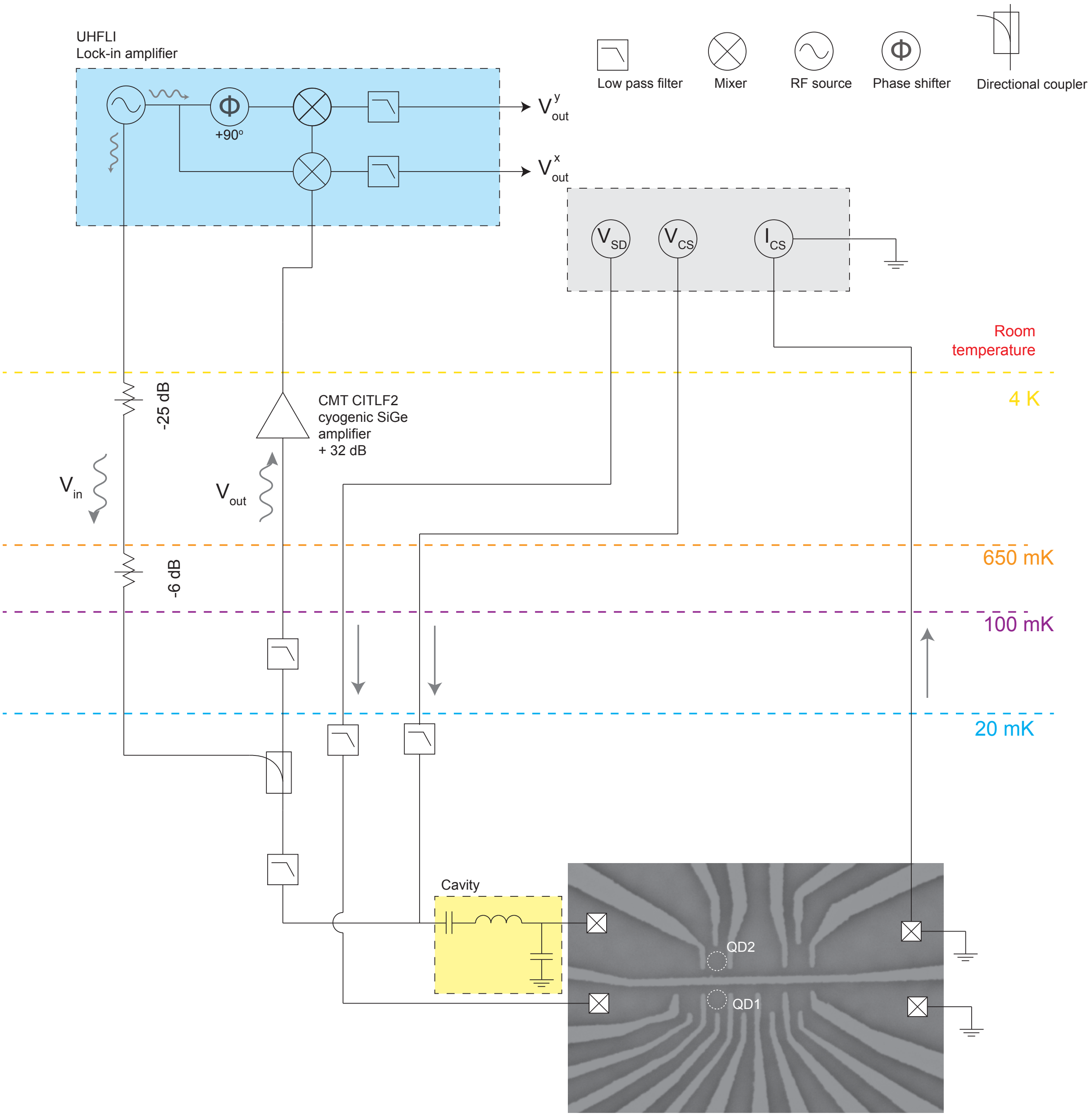

Figure 4.6: Schematic of the measurement as described in Section 4.3.1

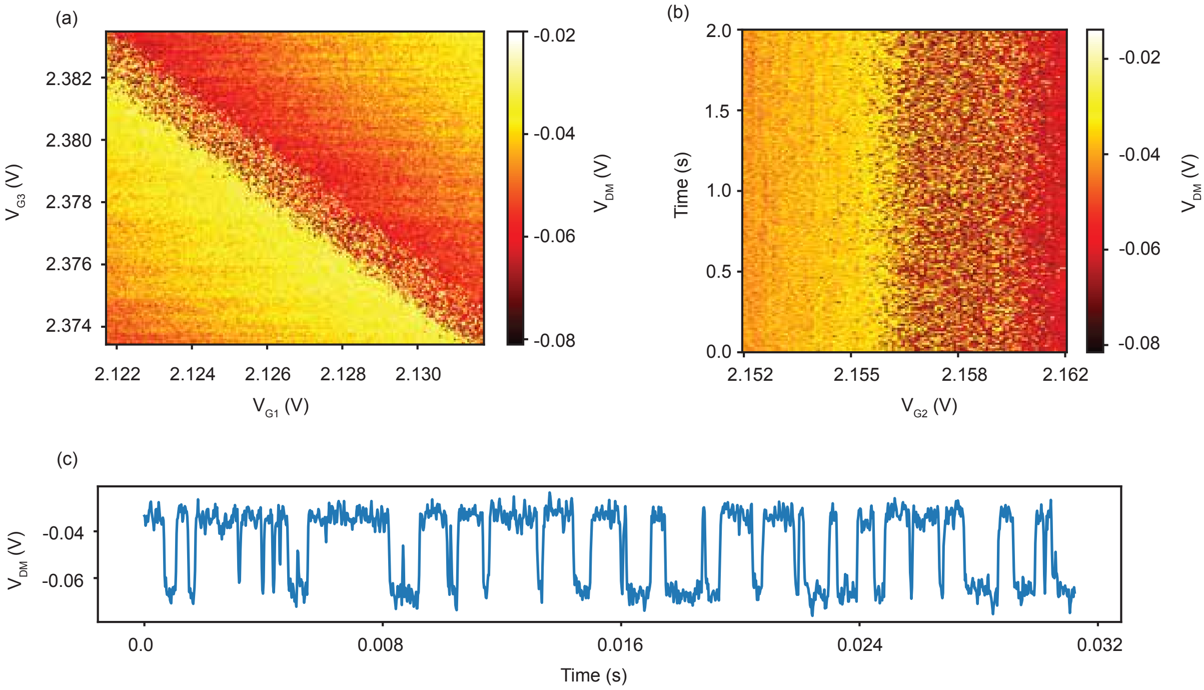

Figure 4.7: (a) Charge sensing reflectometry measurement of QD1, showing a transition between unoccupied and occupied states. The demodulated voltage, V_{DM} is plotted as a function of the barrier gate voltages VG1 and VG3. The transition appears noisy due to the switching events occurring within the bandwidth of the measurement setup. (b), Occupation of the erasure dot as a function of V_{G2}, measured using charge sensing reflectometry. The sweep is taken across the transition shown in (a), with each value of V_{G2} representing a two-second time trace.

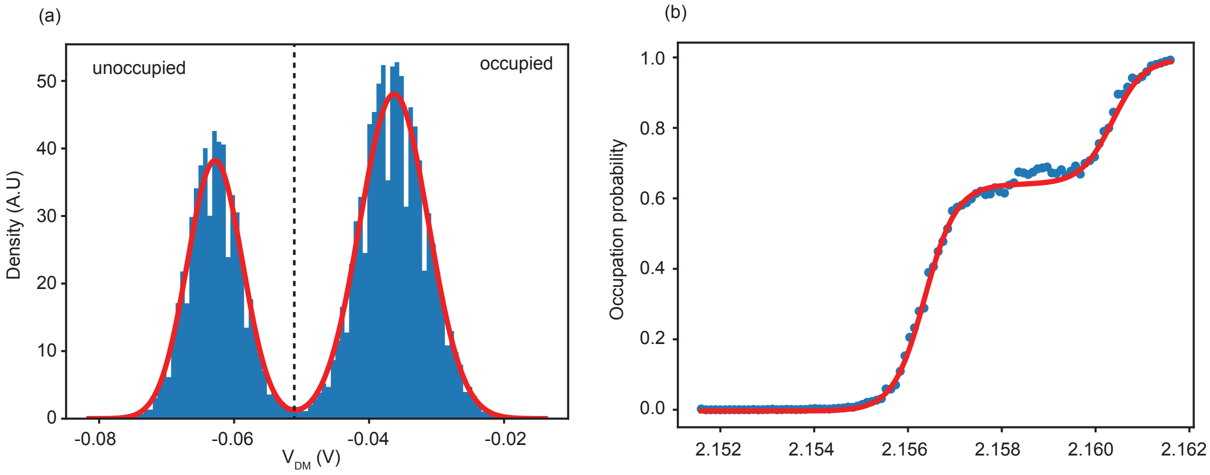

Figure 4.8: (a) Histogram of the demodulated voltages measured in Fig. 4.7b. Red curve is a fit to a bimodal Gaussian distribution described by Eq. 4.53. The two peaks of the distribution represent occupied and unoccupied states of the dot. (b) Dot occupation probability as a function of V_{G2}. Blue dots are measured probabilities computed from the time traces of Fig. 4.7b. The red curve is a fit to Eq. 4.7 from the main text, yielding $\alpha = 0.048$ eV/V.

where t_{tot} is the duration of the time trace and t_{occ} the total time that the dot is occupied during the time trace. Extracting t_{occ} is achieved by creating a histogram of the time trace's voltages which is then fitted to a bimodal Gaussian distribution

$$p(V_{\mathrm{DM}}) = \sum_{i=1}^{2} h_i \mathcal{N}(V_{\mathrm{DM}}; \mu_i, \sigma_i), \tag{4.53}$$

where μ_i and σ_i are the mean and standard deviations of the ith Gaussian. The prefactor h_i accounts for the relative probabilities of the occupied and unoccupied states of the dot. An example of this fit is shown in Fig. 4.8a, where the two peaks correspond to the occupied and unoccupied states of the dot. To classify the charge occupation at a given time, we compare each measured value of V_{DM} against the fitted Gaussian distributions and assign it to the state (occupied or unoccupied) whose distribution it most likely belongs to. Measurements are performed at a sampling rate of $f_s = 50$ kHz. For a given time trace, t_{occ} is computed as

$$t_{\mathrm{occ}} = \frac{n_{\mathrm{occ}}}{f_s}, \tag{4.54}$$

where n_{occ} is the number of samples for which the dot is occupied. The first stage of the erasure protocol described in Section 4.2.1 requires the QD to be initialised with its electrochemical potential at $\mu_{\frac{1}{2}}$ such that $p_{ss}(\mu_{\frac{1}{2}}) = 0.5$. Fig. 4.8b shows a typical plot of the steady state occupation probability p_{ss} as a function of V_{G2} obtained using the method described above. From this plot it is straight forward to extract the value of V_{G2} corresponding to $p_{ss} = 0.5$. In order to extract the value of $\mu_{\frac{1}{2}}$, we convert voltages to electrochemical potentials using

$$\mu = -e\alpha V_{G2}, \tag{4.55}$$

where α is the lever arm of gate G2. We obtain α from Fig. 4.8b by using Eq. 4.55 to rewrite Eq. 4.7 in terms of the plunger gate voltage and performing a least squares fit, with Γ_S, Γ_D and α as fitting parameters. An example of this fit is shown in Fig. 4.8b from which we obtain $\alpha = 0.048$ eV/V.

Tunnelling rates

The tunnelling rates define the characteristic relaxation time of the QD through the expression

$$\tau_{\text{eq}} = \frac{1}{\Gamma}, \tag{4.56}$$

where $\Gamma = \Gamma_S + \Gamma_D$, with $\Gamma_{S,D}$ the intrinsic tunnelling rates associated with the dot's coupling to the source and drain electrodes, which are assumed to be energy independent. In a d-fold degenerate QD the rate at which electrons tunnel into the dot is given by the sum of the rates into the d degenerate states, while the rate at which electrons tunnel out of the dot correspond to electrons leaving through a single occupied level. Consequently, for a d-fold degenerate QD coupled to source and drain electrodes characterised by Fermi functions $f_S(\mu)$ and $f_D(\mu)$, the effective tunnelling rates into an empty state and out of an occupied state are given by

$$\begin{aligned}
\gamma_S^{\text{in}} &= d\Gamma_S f_S(\mu) \\
\gamma_D^{\text{in}} &= d\Gamma_D f_D(\mu) \\
\gamma_S^{\text{out}} &= \Gamma_S(1 - f_S(\mu)) \\
\gamma_D^{\text{out}} &= \Gamma_D(1 - f_D(\mu)),
\end{aligned} \tag{4.57}$$

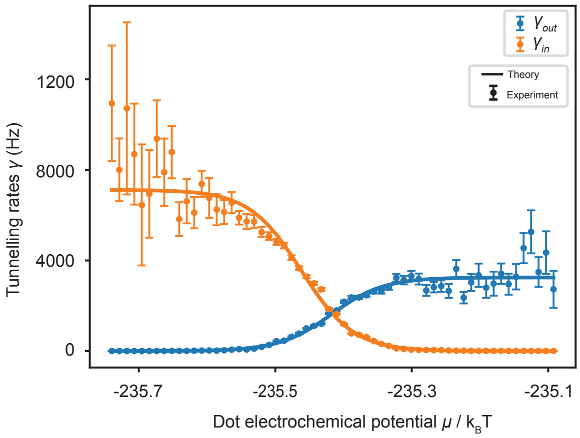

Figure 4.9: Effective tunnelling rates γ^{in} and γ^{out} as a function of the dot's electrochemical potential. The rates are extracted via Eq. 4.59 using time traces measured by sweeping across the transition shown in Fig. 4.7a at zero bias. Solid curves are weighted least-mean-square fits to Eq. 4.58, with uncertainties representing the standard error calculated according to Eq. 4.60

At zero bias, where $f_S(\mu) = f_D(\mu)$, the dot is effectively coupled to a single environment characterised by a Fermi function $f(\mu)$. In this case, the effective tunnelling rates simplify to

$$\begin{aligned} \gamma^{\text{in}} &= \Gamma_{\text{in}} f(\mu), \\ \gamma^{\text{out}} &= \Gamma_{\text{out}}(1 - f(\mu)), \end{aligned} \tag{4.58}$$

where $\gamma^{\text{in}} = \gamma_S^{\text{in}} + \gamma_D^{\text{in}}$, $\gamma^{\text{out}} = \gamma_S^{\text{out}} + \gamma_D^{\text{out}}$, and $\Gamma_{\text{in}} = d\Gamma$ and $\Gamma_{\text{out}} = \Gamma$. The effective tunnelling rates can be estimated from time traces such as those shown in Fig. 4.7b using the expression [51]

$$\gamma^{\text{out/in}} = \frac{1}{\left\langle t_{\text{occ/unocc}} \right\rangle}, \tag{4.59}$$

where $\left\langle t_{\text{occ/unocc}} \right\rangle$ represents the average time that the dot is occupied/ unoccupied during a given time trace [51]. In Fig. 4.9 we use the time traces shown in Fig. 4.7a to plot $W_{\text{in/out}}$ as a function of the dot's electrochemical potential at zero bias.

Uncertainties in this plot represent the standard error given by

$$\sigma^W_{\text{occ/unocc}} = \frac{1}{\left\langle t_{\text{occ/unocc}} \right\rangle^2} \frac{\sigma^t_{\text{occ/unocc}}}{\sqrt{N}}, \tag{4.60}$$

where $\sigma^t_{\text{occ/unocc}}$ is the standard deviation of the occupied/unoccupied dwell times, and N is the number of occupied/unoccupied events. A weighted least-squares fit of Eq. 4.58 to these plots gives $\Gamma_{\text{in}} = 7$ kHz and $\Gamma_{\text{out}} = 3.2$ kHz from which extract $\tau_{\text{eq}} = 0.3$ ms. Additionally, given that $\Gamma_{\text{in}} \approx 2\Gamma_{\text{out}}$ we are able to conclude that the dot is 2-fold degenerate.

Temperature and lifetime broadening

We estimate the temperature T characterising the Fermi-Dirac distributions describing the electronic occupation of the source and drain electrodes by fitting a thermally broadened Coulomb peak of QD1 to the expression [7]

$$G = a\cosh^{-2}\left(\frac{\alpha^* V_g + b}{2kT}\right) + c, \tag{4.61}$$

where a, b, and c are fitting constants, and α^* the lever arm of the dot. We distinguish the lever arm α^* in Eq. 4.61 from the lever arm α determined in Section 4.3.2, since, although they apply to the same dot (QD1), they correspond to different experimental regimes. The lever arm α was determined in a closed regime where transport was slowed by raising the barrier gates G1 and G3. In contrast a Coulomb peak described by Eq. 4.61 is measured using an average current in a more open regime. Given that, in general, α is defined as

$$\alpha = \frac{C_G}{C}, \tag{4.62}$$

where C_G is the capacitance between the gate and the dot and C the total capacitance of the dot. Changes in the electrostatic environment of the dot between the two regimes therefore lead to different values of the lever arm.

Eq. 4.61 is valid in the linear response regime where $\Delta\mu_{S,D} \ll k_B T$, and under the assumption $k_B T \gg \hbar\Gamma^*$, which is met when the conductance of the dot is much smaller than the conductance quantum e^2/h [7]. Once again, we distinguish between Γ, associated with the dot in the closed regime and determined in Section 4.3.2, and Γ^* associated with the dot in the open regime used to measure a Coulomb peak.

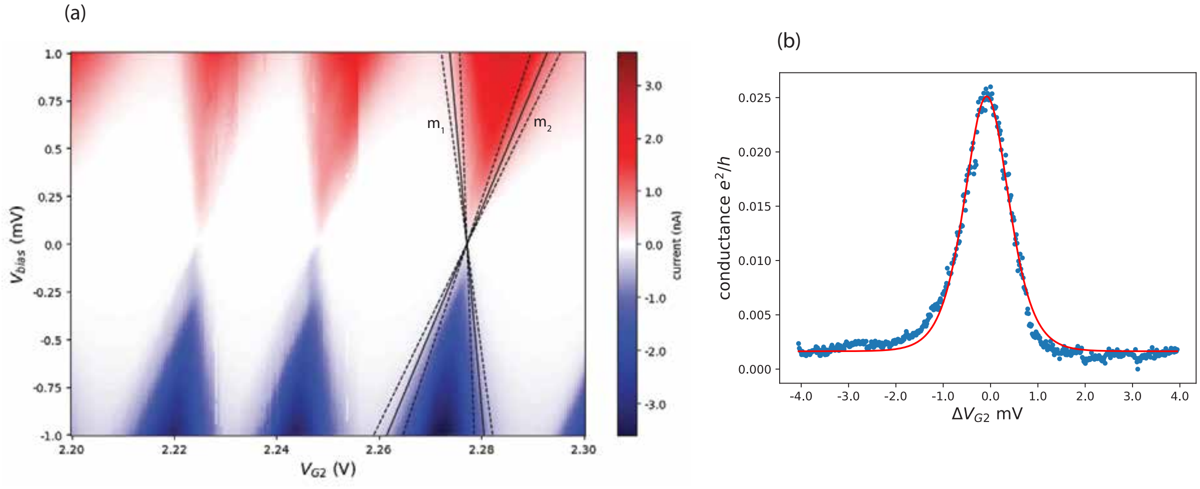

Figure 4.10: (a) Current through QD1 as a function of V_{bias} and V_{G2}, showing Coulomb diamonds indicating that the device is operating in the Coulomb blockade regime. The solid black lines trace the edge of a diamond, with slopes $m_1 = -0.3^{+0.10}_{-0.40}$ and $m_2 = 0.064^{+0.016}_{-0.010}$. Dashed lines represent the uncertainty in the diamond edge position and are used to compute the uncertainties in m_1 and m_2. (b) Conductance of the erasure dot as a function of V_{G2} at $V_{\text{bias}} = 0.015\,\text{mV}$. The red curve is a least-squares fit to Eq. 4.61 Both (a) and (b) were measured at a fridge temperature of 75 mK.

We extract α^* from Coulomb diamonds of QD1 using the expression [49]

$$\alpha^* = \frac{m_1 \times m_2}{m_1 - m_2}, \tag{4.63}$$

where m_1 and m_2 are the slopes of the Coulomb diamond edges, as shown in Fig. 4.10a. The origin of Eq. 4.63 is described in Appendix C. From the figure, we obtain $m_1 = -0.30^{+0.10}_{-0.40}$ and $m_2 = 0.064^{+0.016}_{-0.010}$, giving $\alpha = 0.054^{+0.019}_{-0.0096}$. In Fig. 4.10b, we plot a Coulomb peak of QD1 along with a fit to Eq. 4.61, from which we estimate a temperature of $T = 192^{+70}_{-34}$ mK. The measurement was taken at a bias of 0.015 mV, corresponding to $\Delta\mu_{S,D} = 2.40 \times 10^{-24}$ J. The fridge temperature was $T_F = 75$ mK, giving $k_B T_F = 1.04 \times 10^{-24}$ J, such that $\Delta\mu_{S,D} \sim k_B T_F$. Since $T > T_F$, we conclude that the system is in the linear response regime. Furthermore, we note that the peak conductance is $0.025\ e^2/h \ll e^2/h$, confirming that the condition $k_B T \gg \hbar\Gamma^*$ is satisfied.

From Section 4.3.2, we have $\Gamma_{\text{tot}} = 3.2$ kHz, giving $\hbar\Gamma_{\text{tot}} = 3.37 \times 10^{-31}$ J. A temperature of 195 mK corresponds to $k_B T = 2.70 \times 10^{-24}$ J. Since $k_B T \gg \hbar\Gamma_{\text{tot}}$, we are justified in neglecting the effects of lifetime broadening in our analysis of LE in Section 4.2.1.

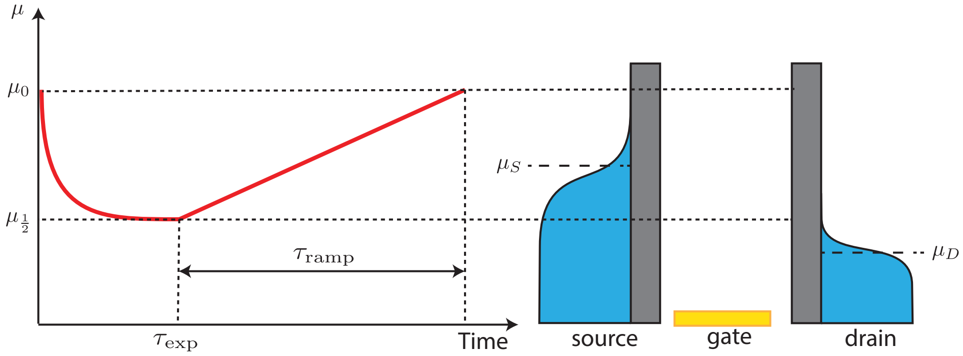

Figure 4.11: Experimental protocol. The dot is primed for erasure by exponentially ramping μ to $\mu_{\frac{1}{2}}$ over a time $\tau_{\mathrm{exp}} \gg \tau_{\mathrm{eq}}$. A linear ramp of duration τ_{ramp} then takes μ to μ_0 (erasure to zero) or μ_1 (erasure to one).

4.3.3 Experimental protocol

The experimental protocol used to perform LE is illustrated in Fig. 4.11. We first use the method detailed in Section 4.3.2 to determine the value of V_{G2} corresponding to $\mu_{\frac{1}{2}}$. Have established $\mu_{\frac{1}{2}}$ we prime the dot for erasure to zero by exponentially ramping μ to $\mu_{\frac{1}{2}}$. This ramp takes place over a time $\tau_{\mathrm{exp}} \gg \tau_{\mathrm{eq}}$ ensuring the dot is in a steady-state when erasure is initiated. Erasure then proceeds by linearly ramping V_{G2} over a time τ_{ramp}, taking the electrochemical potential of the dot from $\mu_{\frac{1}{2}}$ to μ_0 for erasure to zero or μ_1 for erasure to one. Erasure is performed quasistatically when $\tau_{\mathrm{ramp}} \gg \tau_{\mathrm{eq}}$.

Manipulating the dot's electrochemical potential requires work to be performed by the external circuit to change the voltage V_{G2}. We define the work cost associated with a change in μ of $\Delta\mu$ to be $W = \Delta\mu n$, where n is the occupancy of the dot. We therefore see that the work required to perform the final reset stage of the erasure protocol described in Section 4.2.1 is always zero for erasure to zero and $\Delta\mu_1 = \mu_{\frac{1}{2}} - \mu_1$ for erasure to one. Experimentally, we therefore choose to focus on the work associated with the linear ramp, which due to the fluctuating charge occupation of the dot, is a stochastic quantity. To compute this work we measure the charge occupation of the dot throughout the ramp. If measurements of the dot's charge occupation are made at intervals Δt, then measured work associated with a given linear ramp is

$$W = \sum_i \dot{\mu} n_i(t) \Delta t, \tag{4.64}$$

where n_i is the measured occupation of the dot at time t. Experimentally, we wish to measure the work cost as a function of $\Delta\mu_{S,D}$ and τ_{ramp}. Given that W is a stochastic quantity, when measuring the work cost for a given combination of $\Delta\mu_{S,D}$ and τ_{ramp}, we average over 200 realisations of the protocol. In this regime we understand the LB as a quantity that can be violated for individual realisations of the protocol but not on average [35].

4.3.4 Work cost error analysis

Accurately measuring the work cost associated with a given ramp requires the dot to be correctly initialised at $\mu_{\frac{1}{2}}$. This is achieved by estimating the occupation probability of the dot as a function of V_{G2} and selecting the voltage, $V_{\frac{1}{2}}$, associated with an occupation probability of 0.5. Any uncertainty in the estimation of the occupation probability $\Delta p_{\frac{1}{2}}$ will therefore lead to an uncertainty in $V_{\frac{1}{2}}$ and, consequently, to an uncertainty in the work cost. An error in $V_{\frac{1}{2}}$ can be translated into an error in the initialisation time of the erasure ramp. The idea is illustrated in Fig. 4.12 where an error in $V_{\frac{1}{2}}$, $\pm\Delta V_{\frac{1}{2}}$, leads to an error in the initialisation time $\pm\Delta t_{\text{init}}$.

When erasing to zero an error $\pm\Delta t_{\text{init}}$ results in an error $\pm\Delta W$ in the work cost. When erasing to one an error $\pm\Delta t_{\text{init}}$ leads to an error of $\mp\Delta W$. For a given ramp we can compute $\pm\Delta W$ by using Eq. 4.64 to find the amount of work done in the time $\pm\Delta t_{\text{init}}$. We can relate Δt_{init} and $\Delta p_{\frac{1}{2}}$ via

$$\Delta t = \frac{dt}{dV_{G2}} \left. \frac{dV_{G2}}{dp} \right|_{p=\frac{1}{2}} \Delta p_{\frac{1}{2}}. \tag{4.65}$$

Given the ramp used to perform erasure is linear, $\frac{dt}{dV}$ is a known constant. The term $\left.\frac{dV}{dp}\right|_{p=0.5}$ can be computed numerically from the measurement of occupation vs V_{G2} used

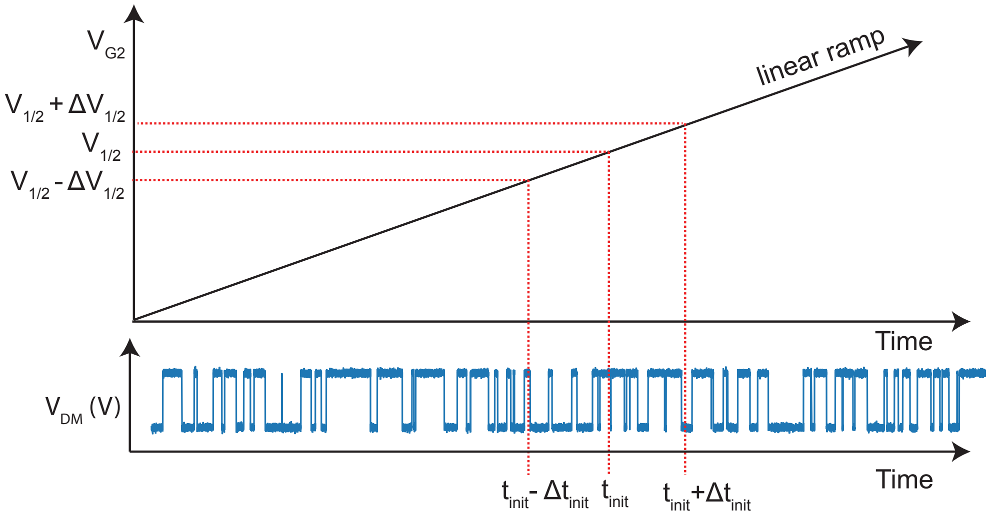

Figure 4.12: In the experiment a linear ramp is applied to V_{G2} whilst the occupation of the dot is measured. An error $\pm\Delta V_{\frac{1}{2}}$ in the initialisation voltage $V_{\frac{1}{2}}$ can be translated into an error $\pm\Delta t_{\text{init}}$ in the initialisation time of the ramp t_{init}.

to extract $V_{\frac{1}{2}}$.

In order to compute Δp we model the occupation of the QD as a continuous time two-state Markov process and the measurement of the occupation of the QD at a fixed value of V_{G2} as a sequence of N_{eff} Bernoulli trials, where N_{eff} is the effective sample size given by [103]

$$N_{\text{eff}} = \frac{T_{\text{tot}}}{2\tau_{\text{int}}}, \tag{4.66}$$

with T_{tot} the total time of the measurement and τ_{int} the integrated autocorrelation time given by

$$\tau_{\text{int}} = \int_0^\infty \rho(\tau)d\tau, \tag{4.67}$$

with $\rho(\tau)$ the autocorrelation function of the Markov process governing the occupation of the QD. Given that the QD is in a steady state as the occupation probability is measured, we can take the Markov process to be stationary. The autocorrelation function is then given by [46]

$$\rho(t) = \frac{\text{Cov}\left[X(0), X(t)\right]}{\sqrt{\text{Var}\left[X(0)\right]\text{Var}\left[X(t)\right]}}. \tag{4.68}$$

To compute the numerator of this expression we use

$$\mathrm{Cov}\left[X(0), X(t)\right] = \mathbb{E}\left[X(0)X(t)\right] - \mathbb{E}\left[X(0)\right]\mathbb{E}\left[X(t)\right] \tag{4.69}$$

Given that the process is stationary we have

$$\mathbb{E}\left[X(0)\right] = \mathbb{E}\left[X(t)\right] = \frac{\gamma_{\mathrm{in}}}{\gamma_{\mathrm{in}} + \gamma_{\mathrm{out}}}. \tag{4.70}$$

Additionally using

$$\mathbb{E}[X(0)X(t)] = \sum_{i\in\{0,1\}} \sum_{j\in\{0,1\}} i \cdot j \cdot P(X(t) = j \mid X(0) = i)\, P(X(0) = i), \tag{4.71}$$

defining $p_{11} = P(X(t) = 1 \mid X(0) = 1)$, we have

$$\mathbb{E}\left[X(0)X(t)\right] = p_{11}P(X(0) = 1). \tag{4.72}$$

The transition matrix $P(t)$ of a two-state continuous time Markov process is given by [46]

$$P(t) = \begin{pmatrix} p_{00}(t) & p_{01}(t) \\ p_{10}(t) & p_{11}(t) \end{pmatrix} = \frac{1}{\gamma_{\mathrm{in}} + \gamma_{\mathrm{out}}} \begin{pmatrix} \gamma_{\mathrm{out}} + \gamma_{\mathrm{in}} e^{-(\gamma_{\mathrm{in}}+\gamma_{\mathrm{out}})t} & \gamma_{\mathrm{in}} - \gamma_{\mathrm{in}} e^{-(\gamma_{\mathrm{in}}+\gamma_{\mathrm{out}})t} \\ \gamma_{\mathrm{out}} - \gamma_{\mathrm{out}} e^{-(\gamma_{\mathrm{in}}+\gamma_{\mathrm{out}})t} & \gamma_{\mathrm{in}} + \gamma_{\mathrm{out}} e^{-(\gamma_{\mathrm{in}}+\gamma_{\mathrm{out}})t} \end{pmatrix}. \tag{4.73}$$

We therefore have

$$\mathrm{Cov}\left[X(0), X(t)\right] = \frac{\gamma_{\mathrm{in}}\gamma_{\mathrm{out}}\, e^{-(\gamma_{\mathrm{in}}+\gamma_{\mathrm{out}})t}}{(\gamma_{\mathrm{in}} + \gamma_{\mathrm{out}})^2}. \tag{4.74}$$

It is straightforward to see that

$$\mathrm{Var}\left[X(0)\right] = \mathrm{Var}\left[X(t)\right] = \frac{\gamma_{\mathrm{in}}\gamma_{\mathrm{out}}}{\gamma_{\mathrm{in}} + \gamma_{\mathrm{out}}}, \tag{4.75}$$

such that

$$\rho(\tau) = e^{-W_{\mathrm{tot}}\tau}. \tag{4.76}$$

The effective sample size is then given by

$$N_{\text{eff}} = \frac{1}{2} T_{\text{tot}} \gamma_{\text{tot}} = \frac{\mathcal{N}}{2}, \tag{4.77}$$

where $\gamma_{\text{tot}} = \gamma_{\text{in}} + \gamma_{\text{out}}$ and $\mathcal{N}$ is the total number of tunnelling events that occurred during the measurement. For a given occupation probability p_1, the number of occupied events in N_{eff} Bernoulli trials follows a binomial distribution. We estimate p_1 from a given time trace using the sample mean $\hat{p}_1$, and approximate the uncertainty using the Wald confidence interval [17, 119]

$$p_1 \approx \hat{p}_1 \pm z_\alpha \sqrt{\frac{\hat{p}_1(1-\hat{p}_1)}{N_{\text{eff}}}}, \tag{4.78}$$

where z_α is the critical value corresponding to the desired confidence level ($z_{0.975} = 1.96$ for a 95% interval for example). A measurement of the work cost represents the average over 200 realisation of the protocol. Since the uncertainty in each repetition originates from the same source (the uncertainty in the value of $V_{\frac{1}{2}}$), the errors across repetitions are correlated. Consequently, the uncertainty in the average work cost is given by

$$\pm\Delta\overline{W} = \pm\frac{1}{N}\sum_i \Delta W_i. \tag{4.79}$$

4.4 Results and Discussion

We saw above that the LB is an equilibrium constraint, reached when erasure is carried out quasistatically and in the presence of a single reservoir. In our system this equates to performing erasure at zero bias ($\Delta\mu_{S,D} = 0$) and at a rate much slower than the equilibration time of the dot ($\tau_{\text{ramp}} \gg \tau_{\text{eq}}$). By tuning the values of $\Delta\mu_{S,D}$ and τ_{ramp} we can measure how the work cost of erasure departs from the LB when non-equilibrium effects become significant. The results presented in this section constitute the main results of this thesis.

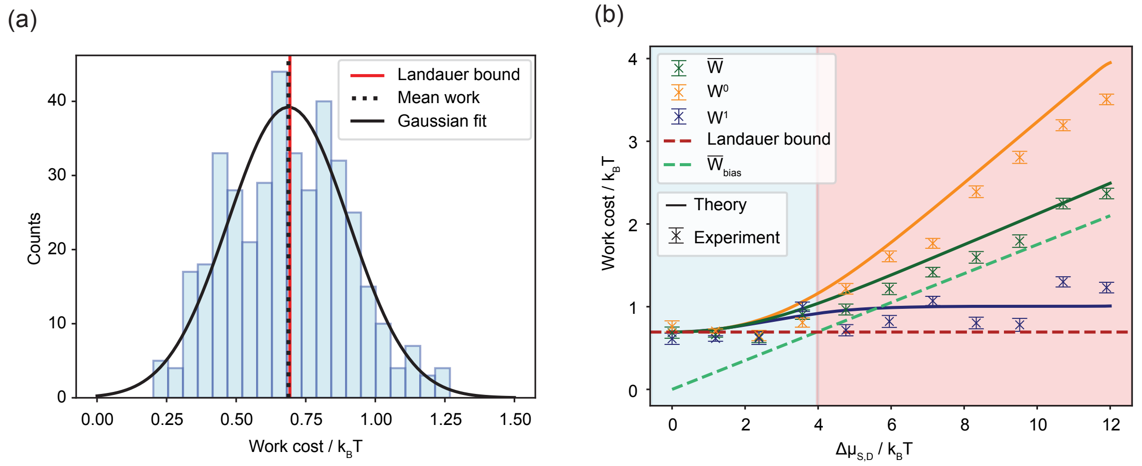

Figure 4.13: (a) Histogram showing the work for 200 quasistatic ($\tau_{\text{ramp}} = 1\,\text{s}$ with $\tau_{\text{eq}} = 0.3\,\text{ms}$) realisations of the erasure to one and erasure to zero protocols at zero bias ($\Delta\mu_{S,D} = 0$). The solid vertical line indicates the LB, while the dotted line represents the mean work. The black solid curve is a Gaussian scaled to match the mean and standard deviation of the measured work distribution. (b) Comparison of predicted and measured work costs for erasure to zero W^0, erasure to one W^1, and their average $\overline{W}$ for a quasistatic ramp with $\tau_{\text{ramp}} = 1\,\text{s}$. Crosses with error bars represent the measured work cost and solid lines theoretical predictions using Eqs. 4.1 and 4.3. The green and red dashed lines represent $\overline{W}_{\text{bias}}$ and the LB, respectively. In the blue region $\overline{W}_{\text{bias}} <$ LB and temperature dominates the erasure process. In the red region $\overline{W}_{\text{bias}} >$ LB and erasure is bias dominated.

4.4.1 Quasistatic erasure

We begin by examining the equilibrium case. The histogram in Fig. 4.13a shows the work cost for 400 realisations of the erasure protocol (200 erasure to zero and 200 erasure to one realisations) with $\Delta\mu_{S,D} = 0$ and $\tau_{\text{ramp}} = 1\,\text{s} \gg \tau_{\text{eq}}$. The average value of the measured work is within 1% of the LB. Owing to the stochastic nature of the charge occupation of the dot, the work cost can be below the LB for individual realisations of the erasure protocol, but not on average [35].

Having demonstrating that our system conforms to the LB in the equilibrium case, we examine how the presence of a bias affects the work cost when erasure is carried out quasistatically. In Fig. 4.13b we plot W^0, W^1, and $\overline{W}$ as functions of $\Delta\mu_{S,D}$ for $\tau_{\text{ramp}} = 1\,\text{s}$. The solid curves represent theoretically predicted values of W^0, W^1, and $\overline{W}$ obtained using Eqs. 4.1 and 4.3. Dashed red and green lines represent the LB and $\overline{W}_{\text{bias}}$ respectively. Crosses with error bars show the measured work cost obtained by

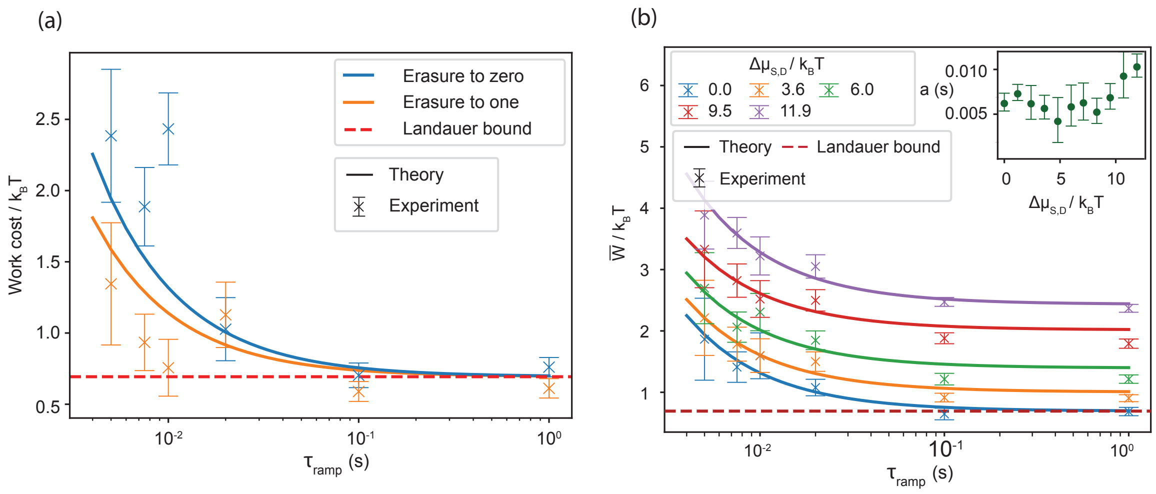

Figure 4.14: (a) Work cost of erasure to zero (blue) and erasure to one (orange) plotted as a function of τ_{ramp} with the device at zero bias ($\Delta\mu_{S,D} = 0$). Crosses with error bars represent the measured work cost obtained by averaging 200 realisations of the erasure protocol. Solid curves represent the work cost predicted using Eqs. 4.50 and 4.51 with $\Gamma = 3.2\,\text{kHz}$. (b) Average cost of erasure $\overline{W}$ plotted as a function of τ_{ramp} for a range of biases. Crosses with error bars represent the measured work cost obtained by averaging over 200 realisations of the erasure protocol. Solid curves represent a fits to Eqs. 4.80 with a as a fitting parameter. Inset shows fitted values of a with their associated uncertainties. Included are a number of points omitted from the main plot for clarity.

averaging over 200 realisations of the erasure protocol. Errors were computed using the method described in Section 4.3.4. In the pink region of the plot $\overline{W}_{\text{bias}} > k_B T \ln 2$ and erasure is bias dominated. In the blue region $\overline{W}_{\text{bias}} < k_B T \ln 2$ and erasure is temperature dominated. In the bias-dominated regime, $\overline{W}$ exhibits a linear dependence on $\Delta\mu_{S,D}$. As the system moves into the temperature dominated regime this linear dependence is lost and $\overline{W}$ tends towards the LB as $\Delta\mu_{S,D}$ tends to zero. We observe good agreement between the measured and theoretically predicted values of W^0, W^1 and $\overline{W}$, with the measured values of W^0 and W^1 demonstrating the emergence of the predicted asymmetry as $\Delta\mu_{S,D}$ is increased.

4.4.2 Finite time erasure

We now examine the effect of a finite-time ramp on the work cost. In Fig. 4.14a we plot W^0, and W^1 as a function of τ_{ramp} with $\Delta\mu_{S,D} = 0$. Crosses with error bars represent the measured work cost obtained by averaging over 200 erasure protocols. Solid curves represent the theoretically predicted values of W^0 and W^1 with $\Gamma = 3.2\,\mathrm{kHz}$. Good agreement is found between theory and experiment with the predicted asymmetry between W^0 and W^1 emerging as τ_{ramp} increases.

Finally, we consider the combined effect of a finite-time ramp and a finite bias on the work cost. In Fig. 4.14b we plot $\overline{W}$ as a function of τ_{ramp} for biases ranging between $\Delta\mu_{S,D} = 0$ and $\Delta\mu_{S,D} = 11.9k_BT$. Solid curves represent a weighted least squares fit to the function

$$\overline{W}(\Delta\mu_{S,D}, \tau_{\mathrm{ramp}}) = \overline{W}_{QS}(\Delta\mu_{S,D}) + \frac{a}{\tau_{\mathrm{ramp}}}, \tag{4.80}$$

where $\overline{W}_{QS}(\Delta\mu_{S,D})$ is the average quasistatic work cost at bias $\Delta\mu_{S,D}$ computed using Eqs. 4.1 and 4.3. The inset to Fig. 4.14b shows the fitted values of a with their associated uncertainties. A chi-squared test for constant value of $a = 0.007$ yields a p-value of 0.609, indicating that the observed variations in a are consistent with statistical noise, from which we conclude that the finite-time correction $\frac{a}{\tau_{\mathrm{ramp}}}$ is, to first order, independent of bias.

4.5 Additional Results

4.5.1 Relationship to the Jarzynski equality

In this section we examine the relationship between the work cost of erasure in the QD system and the JE. If work is performed on a system that is initially in thermal equilibrium with an environment at inverse temperature β, by varying a control parameter λ over a time interval t, then the JE states [56, 57]:

$$\exp(-\beta\Delta F) = \langle\exp(-\beta W)\rangle\,, \tag{4.81}$$

where $\langle\cdot\rangle$ denotes an average over the ensemble of realisations of the process, and

$$\Delta F = F(\lambda_t) - F(\lambda_0) \tag{4.82}$$

is the free energy difference between the equilibrium states corresponding to the initial and final values of the control parameter. When erasure is carried out at zero bias the dot is initialised in equilibrium and we might expect the JE to hold; however, this is not the case as we will now show. Following the fast reset stage of the erasure protocol the QD system is reset to its initial configuration with a well defined occupation. At this point erasure has been performed; however, since the reset occurs on a timescale that is fast compared to the dot's equilibration time, the final state of the system is not an equilibrium state. This does not invalidate the JE since for Eq. 4.81 to hold it is only necessary that the system be initialised in equilibrium. Nevertheless, the quantity $F(\lambda_t)$ refers to the free energy of the *equilibrium* state corresponding to the final value of the control parameter λ_t. Since the fast reset returns the system to its initial configuration, we have $F(\lambda_t) = F(\lambda_0)$, and the JE reduces to

$$\langle \exp(-\beta W) \rangle = 1. \tag{4.83}$$

Jensen's inequality, $\langle \exp x \rangle \geq \exp \langle x \rangle$, then implies

$$\langle W \rangle \geq 0. \tag{4.84}$$

For LE we expect $\langle W \rangle \geq k_B T \ln 2$ and we see that the JE does not describe LE when the final state of the erasure process is non-equilibrium in nature. In order to describe LE in this case we utilise the generalised JE given by [11, 112]

$$\langle \exp(-\beta W(t) \rangle = \frac{\rho^{\mathrm{eq}}\big(\mathbf{x}, \lambda(t)\big)}{\rho(\mathbf{x}, t)} \exp(-\beta \Delta F), \tag{4.85}$$

where $\rho^{\mathrm{eq}}\big(\mathbf{x}, \lambda(t)\big)$ is the equilibrium probability density for the state of the system $\mathbf{x}$ corresponding to the value of λ at time t, and $\rho(\mathbf{x}, t)$ is the actual instantaneous probability density at time t. For erasure in a QD the control parameter is the dot's electrochemical

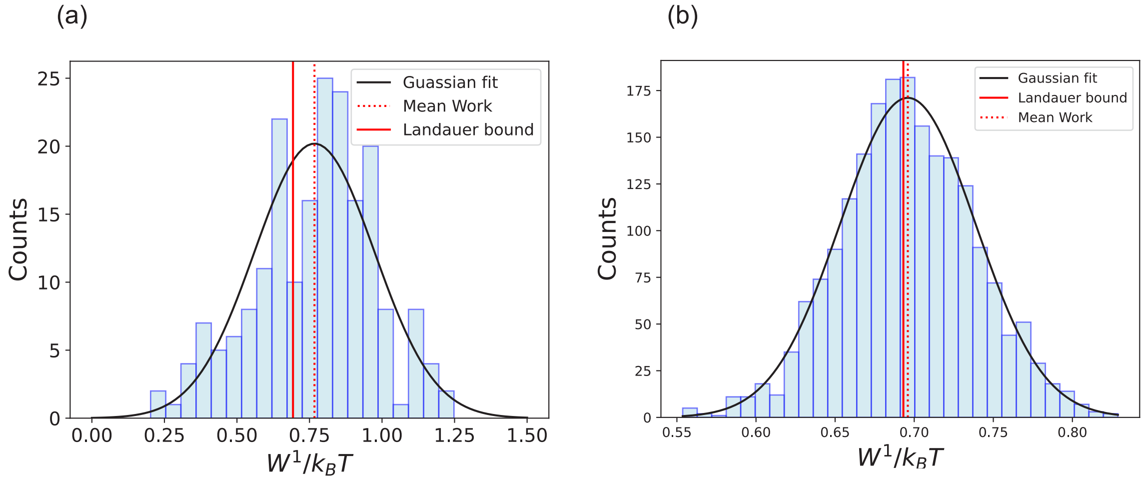

Figure 4.15: (a) Histogram of the experimentally measured work cost for 200 erasure to one protocols with $\Delta\mu_{S,D} = 0$ and $\tau_{\text{ramp}} = 1\,\text{s}$. The black curve represents a scaled Gaussian fit to the data. (b) Histogram showing the distribution of 2000 simulated erasure to one trajectories. Trajectories were simulated using Eq. 4.32 with $\Delta\mu_{S,D} = 0$, $\Gamma = 1$ and $\tau_{\text{ramp}} = 5000\,\text{s}$. The black curve represents a scaled Gaussian fit to the data.

potential μ and the state of the system is described by its occupation n we therefore write

$$\langle \exp(-\beta W(t) \rangle = \frac{\rho^{\text{eq}}\big(n, \mu(t)\big)}{\rho(n,t)} \exp(-\beta \Delta F). \tag{4.86}$$

At the conclusion of the erasure process the dot is in a well defined state such that $\rho(n,t) = 1$; however, once the dot has relaxed to equilibrium we have $\rho^{\text{eq}}\big(n, \mu(t)\big) = \frac{1}{2}$. Setting $\Delta F = 0$ Eq. 4.86 gives

$$\langle \exp(-\beta W(t) \rangle = \frac{1}{2}, \tag{4.87}$$

from which it follows that

$$\langle W \rangle \geq k_B T \ln 2, \tag{4.88}$$

as expected for LE. In Fig. 4.15a we plot a histogram showing the distribution in the work cost for 200 erasure to one trajectories with $\Delta\mu_{S,D} = 0$ and $\tau_{\text{ramp}} = 1\,\text{s}$. The solid curve is a Guassian scaled to match the mean and standard deviation of the distribution. In order to derive an expression for the width of this distribution we use Eq. 4.87 to write

$$\ln \langle \exp(-\beta W(t)\rangle = -\ln 2. \tag{4.89}$$

We can expand the left hand side of this equation using the cumulant generating function

$$\ln \langle \exp tX \rangle = \sum_{n=1}^{\infty} k_n \frac{t^n}{n!}, \tag{4.90}$$

where k_n is the n^{th} cumulant of the random variable X. If we assume the distribution of W^1 shown in Fig. 4.15a is Gaussian, only the first two terms of the expansion are required giving

$$-\beta \left\langle W^1 \right\rangle + \frac{\beta^2}{2}\sigma^2 = -\ln 2, \tag{4.91}$$

from which we obtain

$$\sigma = \sqrt{2\left(\langle W^1 \rangle - \ln 2\right)}, \tag{4.92}$$

where we have expressed σ and $\langle W^1 \rangle$ in units of $k_B T$. The histogram shown in Fig. 4.15a, based on 200 erasure to one trajectories, goes some way to suggesting that W^1 follows a Gaussian distribution. The measured values of W^1 are computed via Eq. 4.64 where the work is expressed as the sum of many individual stochastic contributions accumulated during the ramp. Since the ramps are performed quasistatically, the duration of the protocol is much longer than the equilibration time of the dot, and successive contributions may be treated as effectively independent. Under these conditions, the central limit theorem predicts a Gaussian form for the work distribution.

This prediction is borne out in Fig. 4.15b where we plot a histogram showing the distribution of work costs for 2000 simulated erasure to one trajectories. The trajectories were simulated using Eq. 4.32 with $\Delta\mu_{S,D} = 0$, $\Gamma = 1$ and $\tau_{\text{ramp}} = 5000\,\text{s}$ such that $\tau_{\text{ramp}} \gg \tau_{\text{eq}}$. The black curve represents a fit to a Gaussian. There is a clear convergence to a Gaussian distribution as the number of trajectories is increased from 200 to 2000. Expressed in units of $k_B T$, the mean and standard deviation of the distribution shown in Fig. 4.15a are 0.77 ± 0.015 and 0.21 respectively, where the error in the mean is computed using the method outlined in Section 4.3.4. This leads to a predicted value of

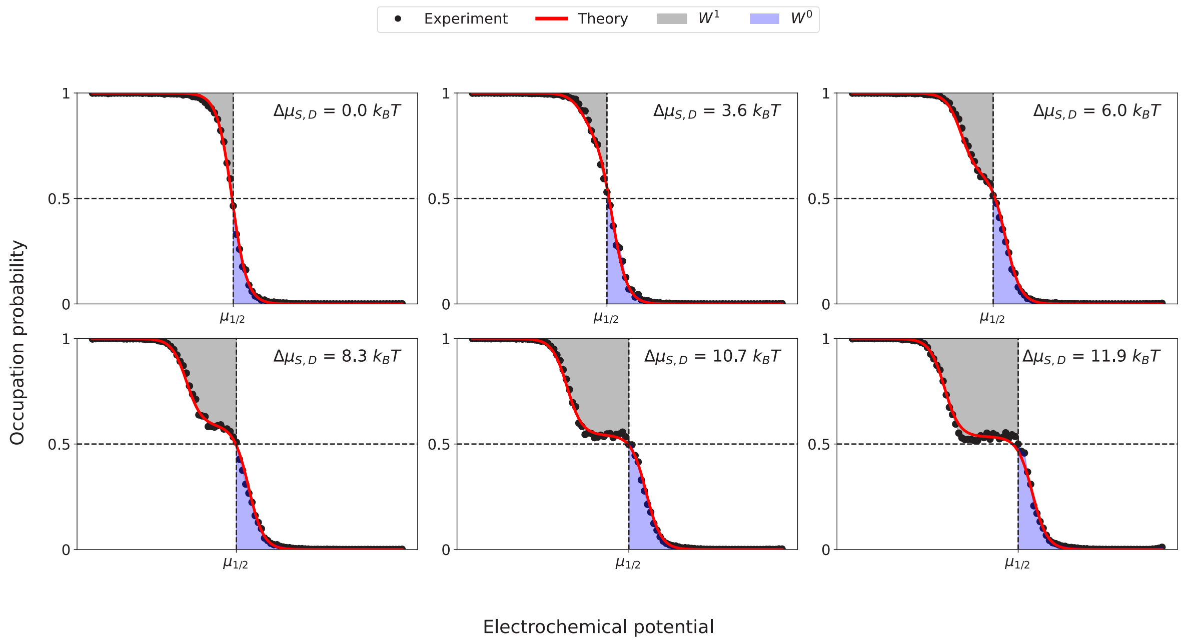

Figure 4.16: Occupation probability as a function the dot's electrochemical potential for a range of values of $\Delta\mu_{S,D}$. Black dots represent the occupation probability measured using the method outlined in Section 4.3.2. Red curves are fits to Eq. 4.93. Grey and blue regions represent W^1 and W^0 respectively.

$\sigma = 0.38 \pm 0.04$. The measured and predicted values of σ broadly agree and we attribute the discrepancy between them to statistical fluctuations in the value of $\langle W^1 \rangle$.

4.5.2 Quasistatic bias dependent work cost

The experimental protocol outlined in Section 4.3.3 was designed to enable to the work cost associated with a realisation of LE to be measured directly. Equations 4.1 and 4.3 suggest that the quasistatic work cost can also be measured indirectly by using the method described in Section 4.3.2 to measure the occupation of the dot as a function of its electrochemical potential and then integrating over the relevant regions of the curve. Of the two methods, the direct approach is preferable, since it requires erasure to be performed and can be extended to the finite-time case. However, by comparing the predictions of Eqs. 4.1 and 4.3 directly to experiment, the indirect method provides a useful consistency check. In Fig. 4.16 we plot the occupation probability of the dot as a function of its electrochemical potential for a range of biases. For a given value of $\Delta\mu_{S,D}$ the black dots represent the occupation probability measured using the method described

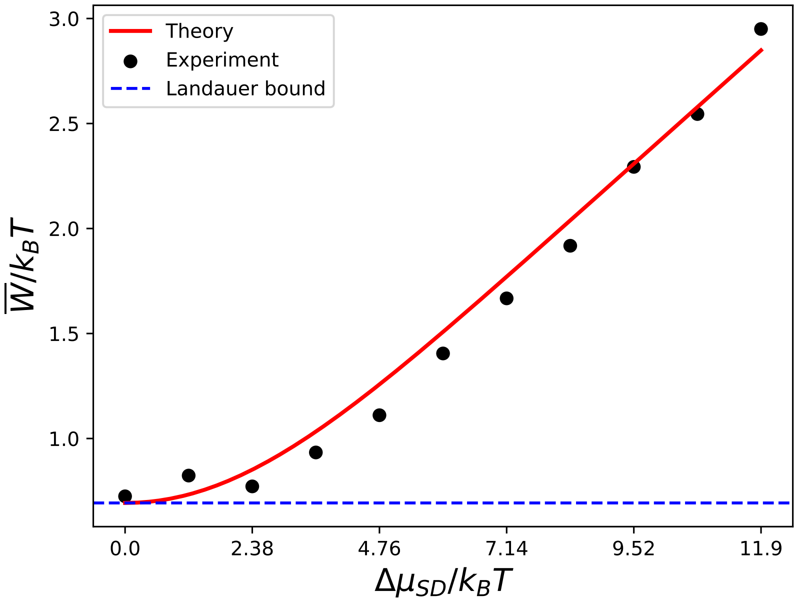

Figure 4.17: Average work plotted as a function of bias. Black dots represent the measured work cost computed via numerical integration of the measured occupation probability vs electrochemical potential plots shown in Fig. 4.16. The red curve represents the theoretically predicted work cost computed by numerically integrating Eq. 4.93 with $r = \frac{20}{9}$.

in Section 4.3.2, with the blue and grey regions representing W^0 and W^1 respectively. We can fit the measured occupation with the theoretical prediction of Eq. 4.7 by noting that Eq. 4.7 can be rewritten in terms of the dimensionless parameter $r = \frac{\Gamma_D}{\Gamma_S}$ giving

$$p_{ss}(\mu) = \frac{2\left[f_S(\mu) + r\, f_D(\mu)\right]}{(1 + f_S(\mu)) + r(1 + f_D(\mu))}. \tag{4.93}$$

The red curves in Fig. 4.16 represent a fit to Eq. 4.93 with r as a fitting parameter. There is a good agreement between theory and experiment and the emergence of the predicted asymmetry between W^0 and W^1 is clearly visible as $\Delta\mu_{S,D}$ is increased. In Fig. 4.17 we plot the average work cost $\overline{W}$ as a function of $\Delta\mu_{S,D}$.

Black dots represent the measured average work computed numerically by integrating the appropriate regions of the associated occupation probability vs electrochemical potential plot (blue and grey regions in Fig. 4.16). In Fig. 4.16 we see the emergence of the plateau at $\eta \approx 0.55$ giving, via Eq. 4.13 $r = \frac{20}{9}$. The red curve represents the average work computed using Eqs. 4.1 and 4.3 with this value of r There is excellent agreement between theory and experiment, providing strong justification that Eq. 4.93 effectively captures the steady-state occupation probability of the dot.

4.5.3 Plateau manipulation

In Section 4.2.2 we saw how the asymmetry between W^0 and W^1 is governed by the position of a plateau in the plot of occupation probability vs dot electrochemical potential. We saw that this plateau occurs at an occupation probability η given by

$$\eta = \frac{2}{2 + \frac{\Gamma_D}{\Gamma_S}}, \tag{4.94}$$

from which we see that the asymmetry is governed by the relative strength of the tunnelling rates Γ_S and Γ_D. In this section we give an empirical demonstration of this observation. By manipulating the barrier gate voltage V_{G1} we are able to tune the relative tunnelling rates. This, in turn, leads to a shift in the position of η and hence the asymmetry between W^0 and W^1. In Fig. 4.18 we plot the occupation probability of the dot as a function of the plunger gate V_{G2} for increasing values of V_{G1}.

The occupation probability is measured using the method outlined in Section 4.3.2, and the red curve is a fit to Eq. 4.93. Increasing the value of V_{G1} causes the width of the tunnel barrier between the drain and the dot to increase resulting in a decrease of the tunnelling rate Γ_D. This is reflected in the results of Fig. 4.18, where we see that increasing V_{G1} causes the position of the plateau to shift towards larger occupation probabilities, which, via Eq. 4.94, tells us that $\frac{\Gamma_D}{\Gamma_S}$ is decreasing with increasing V_{G1}.

4.6 Conclusion

In this work we extended the concept of LE beyond the conventional single-reservoir framework by experimentally investigating the cost of erasing a single bit of information encoded in the electronic occupancy of a QD coupled to two Fermionic reservoirs at different electrochemical potentials. We confirmed that in the single-reservoir, quasistatic limit when the dot remains in equilibrium throughout the erasure process, the LB can be

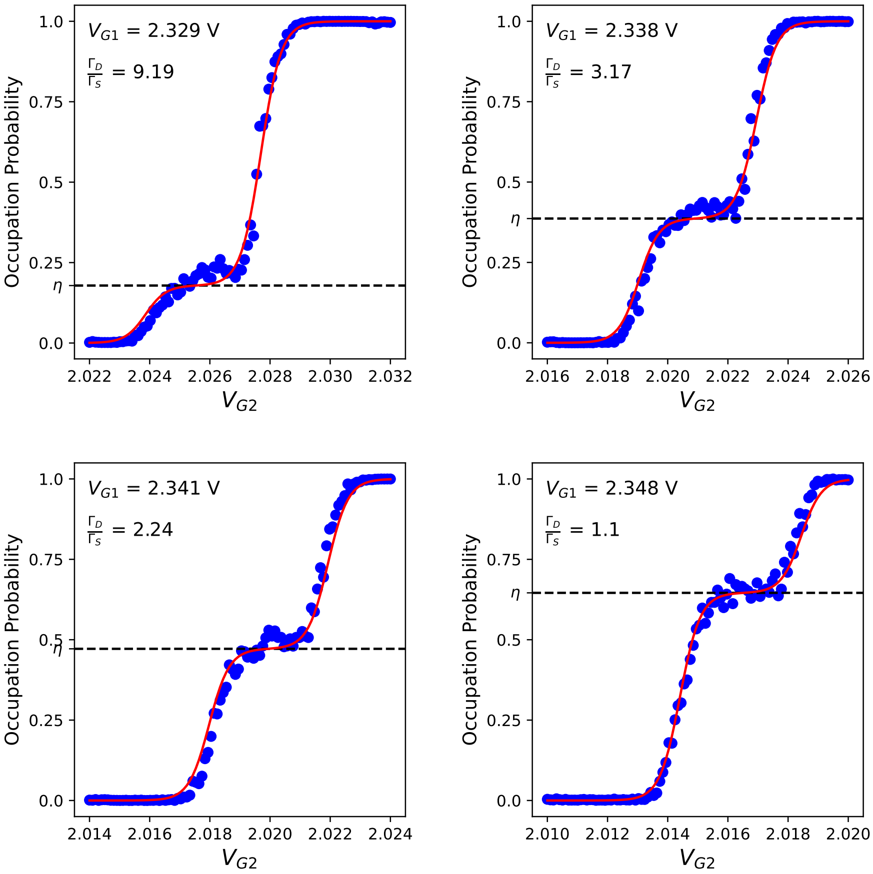

Figure 4.18: Occupation probability vs plunger gate V_{G2} for increasing values of barrier gate V_{G1}. Blue dots are the measured occupation probability and the red curve is a fit to Eq. 4.94

reached with very high accuracy. In addition, in agreement with previous experimental work, [10,12,30,61] , we showed that, when erasure is performed in finite time and in the presence of a single reservoir, the work cost scales inversely with erasure duration, τ_{ramp}^{-1}.

Building on these results, we found that as the erasure process departs from equilibrium, asymmetries emerge in the work required to erase to zero and to one. Specifically, we experimentally validated that the inclusion of an additional reservoir introduces such an asymmetry, which becomes increasingly pronounced as the bias across the device is increased. In addition, we predicted that the two-fold degeneracy of the

This work represents the first experimental study of LE in a multi-reservoir system. It emphasises how the intrinsic properties of a physical system, such as energy level degeneracy and tunnelling rates, influence the cost of erasure as the idealised equilibrium constraints underlying LE are relaxed. A further example is lifetime broadening. QDs in regimes where lifetime broadening dominates over thermal broadening have been realized experimentally [116], and theoretical bounds on the work cost of erasure in this regime have been derived [36]. Investigating the effect of lifetime broadening on the work cost of erasure therefore represents an interesting direction for future research.

Further avenues for future work could include extending the model to include additional degrees of freedom (three or four fold degenerate levels for example) and understanding how existing work on protocol optimisation [1, 34, 87, 88, 94, 128] could be extended to the multi-reservoir case. Our results have implications for information processing: minimising dissipation in bipartite systems where the work cost of erasure differs between states may require an optimised encoding scheme that reduces the use of the higher-cost state.

5

An Autonomous Nanomechanical Clock Driven By Quantum Electromechanics

Contents

5.1 Introduction

Section 2.3 of this thesis provided an overview of the thermodynamics of clocks and timekeeping. We saw how clocks can be understood as bipartite systems consisting of a clockwork and a register. The clockwork being a non-equilibrium system whose dynamics generate a sequence of ticks, while the register is a readout mechanism that allows these ticks to be observed and used as a reference to measure time. From a thermodynamic perspective, we also saw that improving a clock's performance necessarily requires increased dissipation, highlighting a fundamental trade-off between the clock's accuracy and the entropy produced by its operation.

In this chapter, we introduce a clock whose clockwork consists of a suspended CNTQD device of the kind introduced in Section 3.1.7. Using suspended CNT devices to study the thermodynamics of timekeeping offers a number of advantages. The mechanical degree of freedom provides a simple dynamical system that can serve as the clock's clockwork. Readout of the CNT clock is facilitated by the fact that electron transport through a QD defined in an oscillating CNT results in an oscillating current that tracks the mechanical motion of the CNT [116]. By measuring this current, we can extract a tick record from which the performance of the clock can be assessed. In principle, therefore, both the clockwork and the readout mechanism can be integrated into a single experimental platform.

A further advantage is presented by the fact that interactions between the device's mechanical degree of freedom and single-electron tunnelling through a QD defined within the CNT have been shown to result in self-sustained oscillations [110,122]. By exhibiting self-sustained oscillations, the CNT system enables the study of a fully autonomous clock. A clock is autonomous if it is self contained and can be operated without any external control [38]. In particular, an autonomous clock should not require any time dependent control as this would result in measures of the clock's performance, such as its accuracy, depending on the performance of a secondary external clock. Autonomous clocks are of particular interest in thermodynamic studies of timekeeping, as their self-contained nature ensures that all resources required for their operation can be precisely accounted for [38].

Finally, the small size and comparatively simple nature of the suspended CNT system makes measuring the dissipation associated with its dynamics experimentally possible. As a result, quantifying the trade-offs inherent in the clock's operation between dissipation and accuracy becomes an experimentally achievable goal.

The experimental realisation of a clock based on a suspended CNT would represent a novel contribution to the literature on the thermodynamics of timekeeping in two important respects. Firstly, previous experimental work involving clocks with mechanical degrees of freedom has remained firmly within the classical regime [86]. In contrast, the clock discussed in this chapter is driven by single-electron tunnelling, and therefore represents the first mechanical clock to be studied the dynamics of which require a quantum mechanical description. Secondly, the current that forms the basis of the clock's readout mechanism originates from the same single-electron tunnelling events that drive the self-oscillations of the CNT. This means that the clockwork and readout mechanisms originate from the same dynamical process. This stands in contrast to previous experimental work, where a clear demarcation exists between the clock's clockwork and its readout mechanism [50, 86, 117].

In addition to the above, the CNT clock described here would also represent the first experimental study of a truly autonomous clock. While clocks with autonomous clockwork have previously been realised [86, 117], their readout mechanisms have relied on the use of a local oscillator for operation. Although the local oscillators used in these studies were significantly more stable than the clocks under investigation, and therefore did not affect the performance of the clocks under study, their presence in the readout process meant that these clocks could not be considered fully autonomous. In principle, the clock discussed in this work could be operated without the need of any external time reference, allowing for a genuinely autonomous realisation of both clockwork and readout.

Although the focus of this chapter is the experimental realisation of the CNT clock described above, we note at the outset that the experiment could not be completed due to unforeseen technical limitations. Nonetheless, the work presented here makes several original contributions. In Section 5.4, a comprehensive experimental protocol is outlined for implementing the CNT clock. This is followed up in Section 5.7, where a method is proposed for measuring the entropy production associated with the clock's operation. In Section 5.6, a theoretical framework is developed for analysing the data that would be produced by the experiment. This includes the description of an optimal method for extracting ticks of the clock from the measured signal. While this method has previously been applied to the analysis of a different clock [86], the proof of its optimality is original to this work and is presented here for the first time. Also detailed in Section 5.6 is a method for determining the accuracy of the clock from the measured signal, taking into account noise added by its interaction with the cryostat amplifier chain to which it is coupled. In Section 5.5 we present initial experimental results characterising a CNTQD device. Although these results are not themselves novel, they represent an important step towards realising the proposed experiment.

Taken together, the work presented in this chapter provides a comprehensive framework for the full experimental realisation of a CNT clock, the implementation of which would represent an important contribution to the literature on the thermodynamic of clocks and timekeeping.

5.2 Theoretical Background

5.2.1 Electromechanical model

We saw in Section 3.1.7 how suspended CNTQD devices exhibit a coupling between mechanical motion and single electron transport. This section provides an overview of a model, introduced in Ref. [116], which will be used in Section 5.5.1 to quantity this electromechanical coupling in a physical device.

The setup is similar to that shown in Fig. 3.1 of Section 3.1.1. A QD with electrochemical potential μ is coupled to source and drain electrodes characterised by Fermi functions with temperature T and electrochemical potentials μ_S and μ_D. The electrochemical potential, μ, can be tuned via the application of a voltage to a gate electrode. The QD exchanges electrons with the source and drain at rates Γ_S and Γ_D, respectively. Coupling to the leads results in lifetime broadening of the QDs electrochemical potential, with a characteristic width $\hbar\Gamma_{\text{tot}}$, where $\Gamma_{\text{tot}} = \Gamma_S + \Gamma_D$.

A simplified model of the electromechanical system consisting of the oscillating CNT and the QD coupled to a gate electrode can be constructed by drawing an analogy with a simple optomechanical system [4, 116]. The resulting Hamiltonian is given by

$$H = \hbar\omega_0 a^\dagger a + \mu b^\dagger b - \hbar g_m (a + a^\dagger) b^\dagger b. \tag{5.1}$$

Here $a^\dagger a$ is the phonon number operator for the vibrational mode of the CNT and $\omega_0/2\pi$ its resonance frequency , such that the first term represents the mechanical energy of the vibrating CNT. The operator $b^\dagger b$ corresponds to the occupation number of the QD, such that the second term describes the electrostatic energy associated with an electron occupying the dot. The final term represents the electromechanical coupling between the displacement of the CNT and the charge occupation of the dot, with g_m the electromechancial coupling strength.

As will be shown in Section 5.5.1 below, the suspended CNT device studied in this work satisfies $\hbar\Gamma_{\text{tot}} \gg k_B T$. In this regime the current through the QD is given by [33]

$$I(\mu) = \frac{e\Gamma_S\Gamma_D}{\Gamma_{\text{tot}}} \int_{\mu_S}^{\mu_D} D(E,\mu)\, dE, \tag{5.2}$$

where $D(E,\mu)$ is the density of states of the dot, given by [75]

$$D(E) = \frac{1}{2\pi} \frac{\hbar\Gamma_{\text{tot}}}{(E-\mu)^2 + (\hbar\Gamma_{\text{tot}}/2)^2}. \tag{5.3}$$

Defining the effective tunnelling rates as

$$\gamma^{\text{in}}_{\text{S/D}}(\mu) = \Gamma_{\text{S/D}}\rho_{\text{S/D}}(\mu) \tag{5.4}$$

$$\gamma^{\text{out}}_{\text{S/D}}(\mu) = \Gamma_{\text{S/D}}\left(1 - \rho_{\text{S/D}}(\mu)\right), \tag{5.5}$$

where

$$\rho_S(\mu) = \int_{\mu}^{\mu_S} D(E)dE \qquad \rho_D(\mu) = \int_{\mu_D}^{\mu} D(E)dE, \tag{5.6}$$

Eq. 5.2 can be written

$$I(\mu) = e\frac{\gamma^{\text{in}}_{\text{S}}(\mu)\gamma^{\text{out}}_{\text{D}}(\mu) - \gamma^{\text{in}}_{\text{S}}(\mu)\gamma^{\text{out}}_{\text{D}}(\mu)}{\Gamma_{\text{tot}}}. \tag{5.7}$$

Capacitive coupling between the gate electrode and the QD causes the mechanical motion of the CNT to modify the electrochemical potential of the dot. In the regime where $\Gamma_{\text{tot}} \gg \omega_0$ the average occupation of the QD can be treated as an instantaneous function of position and is given by

$$p(\mu(z)) = \frac{\gamma^{\text{in}}_{\text{S}}(\mu(z)) + \gamma^{\text{in}}_{\text{D}}(\mu(z))}{\Gamma_{\text{tot}}}, \tag{5.8}$$

where μ is now written as a function of the CNT's displacement z from its equilibrium position z_0. Single-electron tunnelling through the QD modifies the mechanical resonance frequency of the CNT [75,105,116]. An effective resonance frequency $\omega_0^{\text{eff}}/2\pi$, lower than the intrinsic frequency $\omega_0/2\pi$, is observed when μ varies within the bias window defined by $\mu_S - \mu_D$. The effective resonance frequency is given by

$$\omega_{\text{m}}^{\text{eff}}(\mu_0) = \sqrt{\omega_{\text{m}}^2 + 2g_{\text{m}}^2\hbar\omega_{\text{m}}\left.\frac{\partial p}{\partial \mu}\right|_{\mu_0}}, \tag{5.9}$$

where μ_0 is the electrochemical potential of the dot with the CNT at rest.

5.2.2 Self sustained oscillations

The self-oscillating CNTQD system can be understood as an example of a limit cycle. Limit cycles arise in non-linear, dissipative dynamical systems where a balance between energy dissipated and energy supplied to the system lead to the emergence of stable closed trajectories in the system's phase space [107]. Several models exist with the capacity to capture this behaviour in the context of the suspended CNT system [8, 14, 23, 111]. In this work, we focus on the model developed in Ref. [28], whose dynamical analysis of the suspended CNTQD system emphasises the system's applicability to the study of clocks and timekeeping. Here we give a brief overview of the main results of this analysis. A more detailed discussion is presented in Appendix D.

The CNTQD system will exhibit self sustained oscillations when the following condition is met

$$k_B T/\hbar,\ \Gamma_{\text{tot}} \ \gg\ \omega_0,\ g_m. \tag{5.10}$$

When the condition given by 5.10 is met the system is said to be in the *quasiadiabatic* regime. The electronic degrees of freedom relax on a timescale much faster than the characteristic timescale of the oscillator. As a result of the electric field generated by the gate electrode situated below the suspended CNT, in the quasiadiabatic regime, the oscillator experiences an average electrostatic force that depends on its instantaneous position.

When the stochastic nature of electron tunnelling events are taken into account the dynamics of the oscillating CNT can be shown to be governed by the Langevin equation

[28]

$$m\ddot{z} + m\,\gamma(z)\,\dot{z} + m\omega_0^2 z = F\langle\hat{n}\rangle_z + \sqrt{D(z)}\,\xi(t), \tag{5.11}$$

where m is the mass of the CNT, F is the force per unit charge experienced by the CNT, and $\langle\hat{n}\rangle_z$ is the position-dependent average excess charge on the dot. The terms $\gamma(z)$ and $D(z)$ denote the position-dependent damping and diffusion coefficients, respectively, and $\xi(t)$ is a zero-mean Gaussian white-noise process. Self sustained oscillations arise in the above model when a bias V_{SD} is applied between the source and drain electrodes, and the tunnelling rates $\Gamma_{S,D}$ are energy dependent. Energy dependent tunnel barriers are a well established property of CNT devices of the sort discussed in this work [75, 116, 122]. When the above conditions are satisfied, the model predicts that the damping coefficient $\gamma(z)$ becomes negative for small displacements. As the amplitude of oscillation grows, $\gamma(z)$ increases, eventually becoming positive. This balance between negative and positive damping over the course of a full cycle enables results in the formation of a limit cycle, which manifests as self sustained oscillations.

5.3 Experimental Setup

5.3.1 Cryogenic measurement setup

A schematic of the experimental setup is shown in Fig. 5.1. A suspended CNT device of the kind discussed in Section 3.1.7 is wire-bonded to a printed circuit board (PCB) and mounted in a dilution refrigerator with a base temperature of 20 mK.

The electrostatic potential of the CNT can be tuned via gate electrodes G1 to G5 using DC voltages V_{G1} - V_{G5} , supplied by a Delft IVVI rack, which also provides the source drain bias V_{SD}. Low-pass filters are applied to the dc lines at both the room temperature and 20 mK stages of the cryostat to minimize electrical noise and ensure good thermal anchoring of the sample. An AC drive signal, used to excite mechanical motion of the CNT, is delivered to the gate G3 via a bias tee and coaxial line attenuated at the 4 K, 650 mK and 20 mK stages of the cryostat.

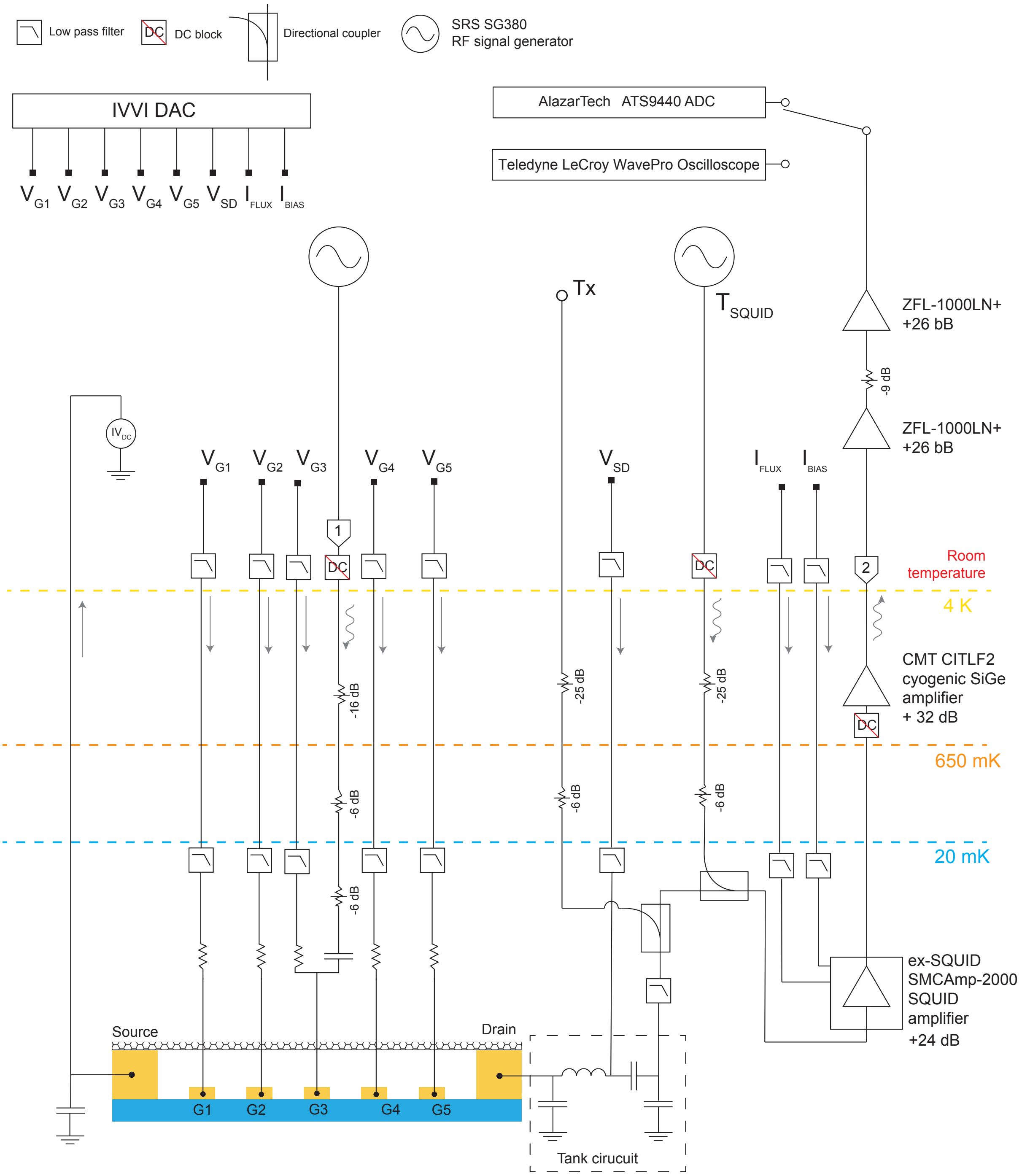

Figure 5.1: Schematic of the experimental setup, as explained in Section 5.3.1

The dc component of the current through the CNT is transduced into a voltage using the IV converter module IV_{dc} of the Delft IVVI rack and subsequently measured using an RS RSDM-906X multimeter. AC current through the CNT is converted into a voltage via a resonant tank circuit, constructed on the PCB using chip inductors and capacitors, and bonded to the drain electrode of the CNT device. The resulting AC voltage is subject to a 1 GHz low pass filter before passing through an amplifier chain consisting of a (super conducting quantum interference device (SQUID)) amplifier mounted on the 20 mK stage of the cryostat, a SiGe low noise cryogenic amplifier at 4 K, and a series of room-temperature amplifiers. The room temperature signal is read out by an AlazarTech ATS9440 analouge to digital converter. A dedicated SQUID tuning line, T_{SQUID}, can be used to apply an RF signal directly to the SQUID amplifier for characterisation. The flux and bias of the SQUID can then be tuned using two low-noise source modules from the Delft IVVI rack (see Section 5.3.3).

5.3.2 Tank Circuit Model

The tank circuit transduces the AC current I_{AC} induced by the oscillating CNT into a voltage V_{out} according to $V_{\mathrm{out}} = I_{\mathrm{AC}} Z_{\mathrm{trans}}$ where Z_{trans} is the transimpedance of the circuit. The circuit exhibits maximum sensitivity to changes in current when driven at its resonance frequency. The frequency of the current generated by the oscillating CNT matches the mechanical resonance frequency of the CNT itself. It is therefore essential that the resonance frequency of the tank circuit closely match that of the CNT. This section presents a model of the tank circuit that can be used to adjust its component values to satisfy this condition.

The tank circuit is modelled using a simple lumped element model. A schematic of the circuit is shown in Fig. 5.2. The self-resonance and loss of the inductor are modelled by including a parasitic capacitance $C_L = 0.091$ pF, and two resistive elements: $R_L = 1.1\,\Omega$ and $R_C = 24\,\Omega25$. These values are taken from the inductor datasheet [24]. Additional capacitive and resistive values are taken from the on-chip components of the PCB to which the device is bonded. Also included in the schematic are a resistance R_{eff} and a

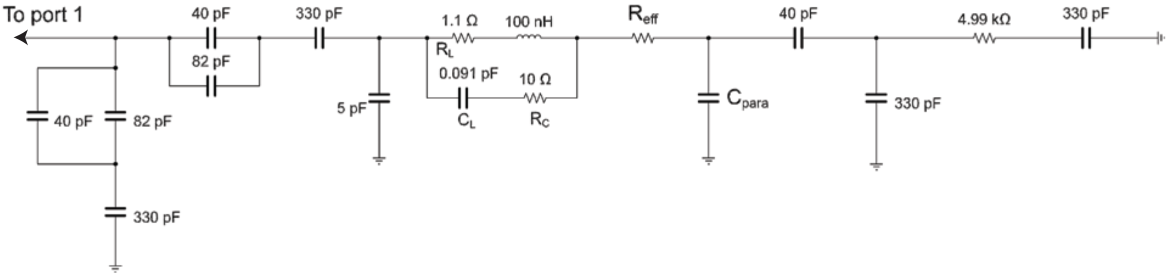

Figure 5.2: Schematic representation of the circuit used to model the tank circuit response. C_L, R_L and R_C are taken from the inductor datasheet. Additional capacative and resistive values are taken from the on-chip PCB components. R_{eff} and C_{para} represent circuit dissipation and parasitic capacitance respectively.

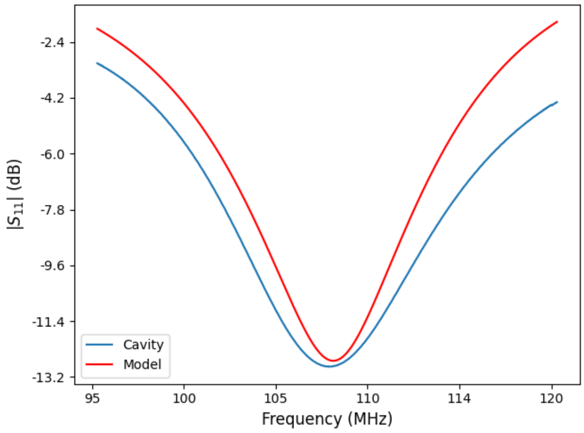

Figure 5.3: Room temperature cavity response and model fit. The blue curve shows the measured reflection coefficient S_{11} of the cavity at room temperature. The red curve represents a simulation using the lumped-element model, with R_{eff} and C_{para} as fitting parameters. The fit yields $R_{\mathrm{eff}} = 5.4\ \Omega$ and $C_{\mathrm{para}} = 400$ pF. Parasitic elements not captured by the model are responsible for the difference between the two curves.

parasitic capacitance C_{para}, which represent circuit dissipation and stray capacitances, respectively. The CNT is not included in the model, as it represents a large parallel resistance and therefore has minimal impact on the overall impedance of the circuit.

The blue curve in Fig. 5.3 shows a room-temperature measurement of the cavity's reflection coefficient S_{11}. The red curve represents a simulation using the lumped-element model, with R_{eff} and C_{para} treated as fitting parameters. The best fit yields values of $R_{\mathrm{eff}} = 5.4\ \Omega$ and $C_{\mathrm{para}} = 400$ pF.

Parasitic elements not captured by the model mean the fit is not perfect; however, it is sufficient for practical purposes. In particular, the model allows the resonance frequency of the tank circuit to be tuned by selecting an inductor with an inductance L that yields the desired response.

5.3.3 SQUID amplifiers

The mechanical amplitude z of driven CNT oscillations in a device with specifications comparable to those discussed here has previously been estimated as $z = 25.2^{+811}_{-24.3}\,\mathrm{pm}$ [121]. The ability of a given measurement setup to resolve small displacements is limited by the noise performance of the primary amplifier in the amplification chain. To optimise displacement sensitivity, we therefore employ a SQUID amplifier as the primary means of amplification.

Compared to semiconductor-based cryogenic amplifiers, such as the one installed at the 4 K stage in the setup shown in Fig. 5.1, SQUID amplifiers typically provide lower noise temperatures and lower power dissipation, particularly at frequencies below 1 GHz, indeed noise temperatures as low as 50 mK have been reported [81]. The SQUID amplifier integrated into our setup has a measured noise temperature of approximately 600 mK when operated under conditions similar to those described here [97]. In contrast, the cryogenic semiconductor amplifier alone is expected to exhibit a noise temperature of < 3 K when operating at a temperature of 12 K [25]. A displacement sensitivity of 144^{+4700}_{-139} fm/$\sqrt{\mathrm{Hz}}$ has been recorded for a measurement setup comparable to the one shown in Fig. 5.1 with a cryogenic amplifier as the primary means of amplification [121]. The incorporation of a SQUID amplifier into the RF measurement chain is expected to enhance this displacement sensitivity. As we shall see in Section 5.6.2, improved displacement sensitivity leads directly to an improvement in the readout of the CNT clock making it an important consideration in the design of the measurement setup.

The central element of the SQUID amplifier is a superconducting loop interrupted by two parallel Josephson junctions. For operation as an amplifier, the SQUID loop should be biased with a current I_B exceeding the critical current of the Josephson junctions. In a typical SQUID amplifier, the input rf signal is first converted into a current I_i, which flows through an input coil inductively coupled to the SQUID loop. The resulting current in the

This image has been removed the publicly available version of this thesis due to copyright restrictions

Figure 5.4: SQUID schematic and response. (a) Schematic of a dc SQUID amplifier configuration. (b) Characteristic voltage-flux response $V(\phi)$ showing the conversion of an input magnetic flux I_i into an output voltage V_o. Figure adapted from Ref. [81].

coil produces a magnetic flux within the SQUID loop, causing a corresponding variation in the SQUID output voltage, V_o (Fig. 5.4(a)). The relationship between the output voltage and the applied flux is periodic, with the period equal to one flux quantum, Φ_0 (Fig. 5.4(b)). To optimize sensitivity, the SQUID must be biased at the point of maximum slope on the curve $V(\Phi)$. This operating point is typically achieved by adding a static flux bias of $(2n-1)\Phi_0/4$ to the input signal. Experimentally, this is achieved by passing a dc current I_Φ through a separate coil that is also tightly coupled to the SQUID loop. The dc current is then tuned to set the SQUID at its optimal sensitivity point [81].

Optimal operation of the SQUID requires appropriate values of I_B and I_Φ to be determined. Our measurement setup includes a dedicated rf line, T_SQUID, specifically for this purpose (Fig. 5.1). Tuning proceeds by sending a low-power signal such that approximately $-120\,\mathrm{dBm}$ reaches the SQUID via T_SQUID. The frequency of this signal should be comparable to the expected frequency of the signal to be measured - the resonance frequency of the CNT. The output of the amplifier chain is connected to a spectrum analyser, and the amplitude of the signal peak is measured as a function of I_B and I_Φ. Tuning proceeds in two stages. First I_B is adjusted to ensure the SQUID is biased above its critical current, then I_Φ is swept to ensure V_o is most sensitive to changes in I_i. Examples of these measurements are shown in Fig. 5.5.

5.4 Measurement Protocol

In order to observe the time dependent nanomechanical current associated with the self-oscillations of a CNT, it is necessary to proceed in four stages: identification of electromechanical coupling, rf detection of driven oscillations, observation of self oscillations and time series measurement of self oscillations. For the reasons detailed in Section 5.5.3 it

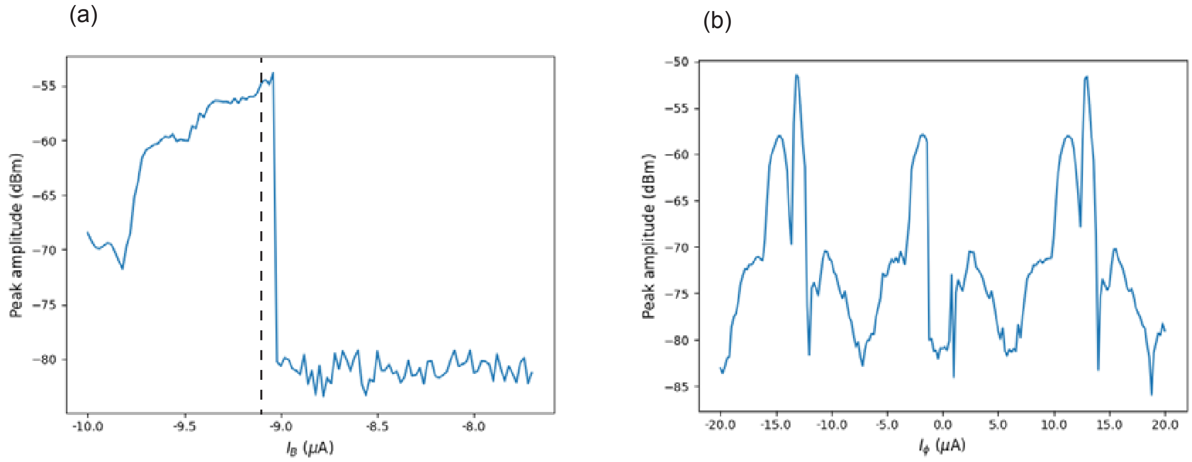

Figure 5.5: SQUID tuning measurements with the SQUID driven with a 200 MHz signal, the power incident on the SQUID being $-120\,\mathrm{dBm}$. (a) Output signal amplitude as a function of bias current I_B. A sharp increase in signal is observed as the SQUID is biased above its critical current. (b) Output signal amplitude as a function of flux bias current I_Φ with the SQUID biased at the dashed line in (a). The periodic modulation reflects the SQUID's characteristic voltage–flux response.

was not possible to proceed beyond the first of these stages. Nevertheless, presented here is the complete methodology that would have been followed, with the aim of establishing a clear protocol for carrying out this experiment in future work.

Identification of electromechanical coupling

We saw in Section 3.1.7 how electromechanical coupling in a CNTQD system manifests as a modulation of the dc current through the CNT at the mechanical resonance frequency, a softening of the resonance frequency as the QD transitions in and out of Coulomb blockade, and a gradual shift in resonance frequency as the gate voltage tensions the CNT. The first stage of the measurement protocol therefore involves tuning the QD to a regime where these features observed. The results of this process are presented in Section 5.5, where the a voltage V_{G3} changes the electrochemical potential of the dot, resulting in a series of Coulomb peaks.

RF detection of driven oscillations

Driven oscillations of the CNT are detected via the rf measurement chain described in 5.3.1 and illustrated in 5.1. A drive tone is applied to gate G3 via port 1 of the rf

This image has been removed the publicly available version of this thesis due to copyright restrictions

Figure 5.6: Detecting self oscillations via using an RF measurement setup. (a), Mechanical resonance detected via the RF measurement chain. To perform this measurement in the setup illustrated in Fig. 5.1, a drive tone would be applied to $G3$ via port 1 with the power of the resulting signal measured via port 2. Peaks in the power occur when the drive signal matches the mechanical resonance frequency of the CNT. (b), Self oscillations detected via the rf measurement chain. Plotted is the power spectral density of the signal from port 2 in the absence of driving. Peaks in the spectrum signify the onset of self oscillations. Figure adapted from Ref. [122]

circuit, with the resulting signal measured through port 2 using a vector network analyser. Driving the CNT on resonance excites its mechanical motion, producing an oscillating current that is transduced into a voltage by the tank circuit. By recording the output power from port 2 while sweeping both the drive frequency and V_{G3}, sharp peaks appear in the transmission spectrum when the CNT vibrates on resonance. These peaks are expected to follow the same trends observed in the dc measurement, confirming their mechanical origin. An example of this measurement taken from [122] is shown in Fig. 5.6a.

Observation of self oscillations

To confirm the presence of self oscillations the output power of the rf measurement chain is measured in the absence of an external drive using a spectrum analyser. If self oscillations are present, the measured power spectral density as a function of V_{G3} should exhibit peaks, the positions of which are expected to follow the same trend observed in the dc and rf measurements. An example of this measurement taken from [122] is shown in Fig. 5.6b.

Time series measurement of self oscillations

Once the presence of self-oscillations has been confirmed, a real-time measurement of the nanomechanical current can be performed. This is achieved by tuning the device to a regime in which self-oscillations are present. The time-dependent current, which forms the basis of the clock's tick record, is then monitored by recording the output signal from port 2 of the rf circuit using a high speed oscilloscope (See Fig. 5.1). The ticks of the clock can subsequently be extracted from this signal using the procedure detailed in Section 5.6.1 below.

5.5 Experimental results

This section presents the experimental results obtained during the first stage of the measurement protocol described above. The challenges that prevented the completion of the experiment are discussed at the end of this section.

5.5.1 Parameter extraction

For the electromechanical model described in Section 5.2.1 to be valid, the system must operate in both the lifetime-broadened and quasiadiabatic regimes, characterized by the conditions $\hbar\Gamma_{\text{tot}} \gg k_B T$ and $\Gamma_{\text{tot}} \gg \omega_0$, respectively. In addition, we saw in Section 5.2.2 that for the CNTQD to exhibit self oscillations the inequality $\Gamma_{\text{tot}} \gg g_m$ must be satisfied. This section presents the measurements used to extract the parameters Γ_{tot}, ω_0 and g_m.

Fig. 5.7 shows a measurement of the differential conductance of the device as a function of gate voltage V_{G3} and the source-drain bias V_{SD}. The presence of a single QD in the CNT is revealed by the characteristic Coulomb diamond pattern visible in the measurement from which a lever arm of $\alpha = 0.026^{+0.0023}_{-0.012}$ is extracted (see Appendix C for a detailed account of this measurement). The lever arm relates variations in gate voltage to changes in the dot's electrochemical potential μ_0 via $\Delta\mu_0 = -e\alpha\Delta V_{\text{G3}}$.

Figure 5.8a shows a measurement of the dc current through the CNT as a function of V_{G3} with a fixed source-drain bias of $V_{SD} = 0.2$ mV. A Coulomb peak is observed as the electrochemical potential of the dot is swept through the bias window. The measurement was taken with the cryostat at a temperature of 300 mK and a source-drain bias of $V_{SD} = 0.2\,\text{mV}$, corresponding to $eV_{SD} \approx 8\ k_B T$. The width of the peak is $\approx 0.02\,\text{V}$. Using the value of the lever arm extracted above this corresponds to $\approx 20\ k_B T$. Given

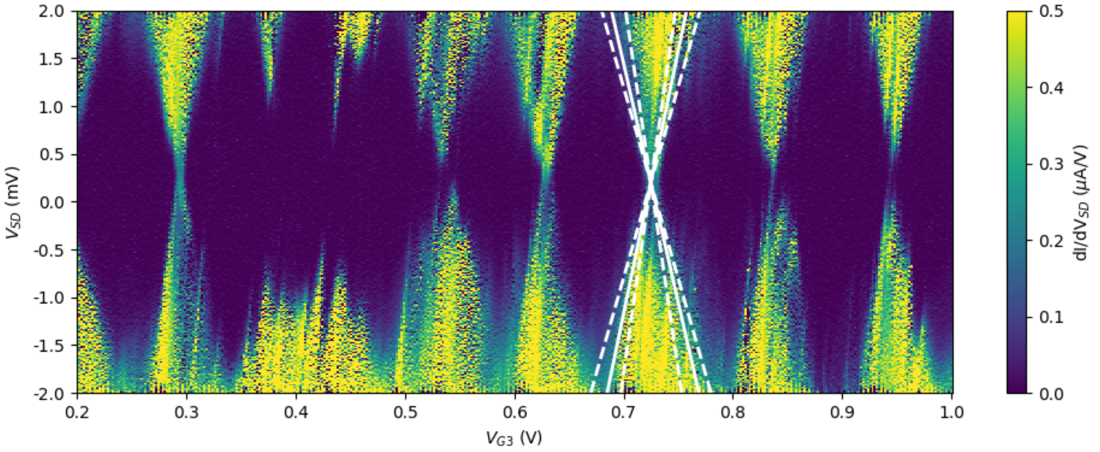

Figure 5.7: Differential conductance computed numerically from a measurement of the dc current through the CNT as a function of V_{G3} and source-drain bias. Solid white lines indicate the estimated edges of a Coulomb diamond and are used to extract the lever arm of gate G3. Dashed lines represent the uncertainty in the position of these edges and are used to quantify the corresponding uncertainty in the lever arm.

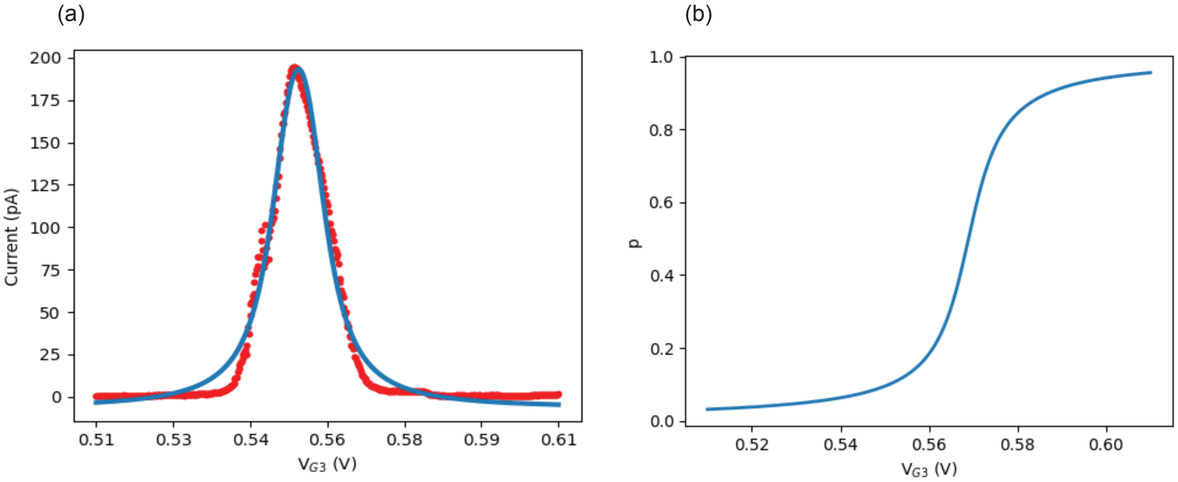

Figure 5.8: Coulomb peak and dot occupation probability. (a) Current as a function of V_{G3} with $V_{SD} = 0.2$ mV. Red dots represent the measured current and the blue curve is a fit to Eq. 5.7. (b) Occupation of the dot as a function of gate voltage estimated using Eq. 5.8 and the tunnelling rates extracted from (a).

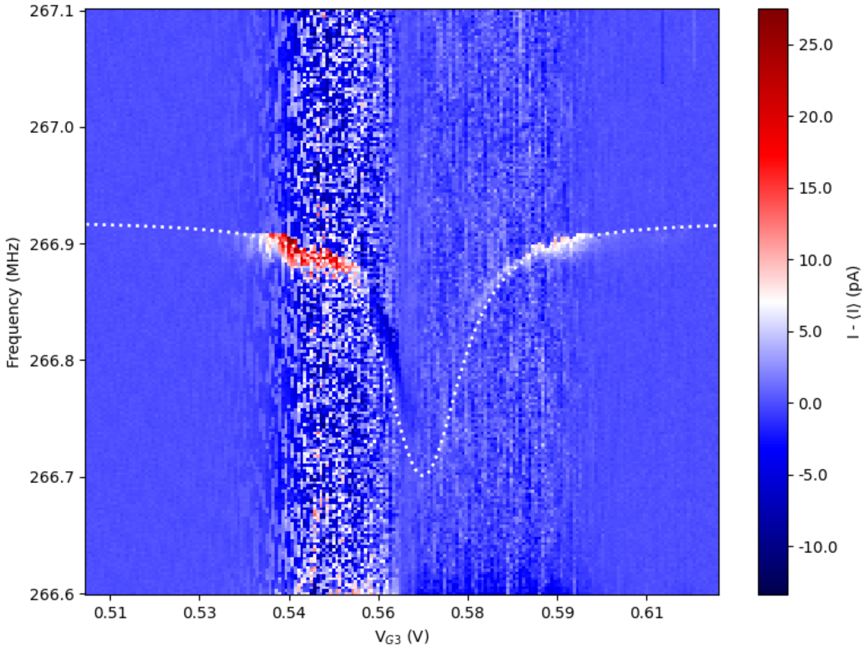

Figure 5.9: Softening of the mechanical resonance frequency of the CNT. The plot shows the deviation of the dc current through the CNT from its average value, measured as a function of drive frequency and V_{G3}. A drive signal was applied to gate $G3$ such that $-81\,\mathrm{dBm}$ reached the gate. The CNT was biased with a source-drain voltage of $V_{\mathrm{SD}} = 1$ mV. The white curve is a fit to Eq. 5.9 using the the estimated occupation probability show in Fig. 5.8(b) and $g_m/2\pi = 0.16 \pm 0.04$ GHz as a fitting parameter.

that the width of the peak is greater than both the thermal energy scale k_BT and the bias window eV_{SD}, neither thermal broadening or the bias window can account entirely for the observed peak width. We therefore assume that the dominant contribution to the peak width arises from lifetime broadening. Under this assumption we are justified in fitting Eq. 5.7 to the observed data with Γ_S and Γ_D treated as free parameters. This fit is shown as the solid curve in Fig. 5.8a and yields $\Gamma_S = 3.23 \pm 0.35$ GHz and $\Gamma_D = 436 \pm 50$ GHz. The uncertainties in these values are estimated by fitting the Coulomb peak using the two extreme values of α, corresponding to the uncertainty in the lever arm. Determining the tunnelling rates enables an estimate of the dot's occupation as a function of its electrochemical potential, using Eq. 5.8. The resulting occupation probability $p(\mu)$ is shown in Fig. 5.8b.

Fig. 5.9 shows the effect of applying a drive signal such that -81 dBm reaches the CNT via gate G3 with $V_{SD} = 1$ mV. The plot displays the deviation in current from its average value $(I - \langle I \rangle)$ as a function of V_{G3} and drive frequency, measured across the

Coulomb peak shown in Fig. 5.8a. A modification of the current is observed when the drive frequency matches the mechanical resonance frequency of the CNT, $\omega_m/2\pi = 266.9$ MHz. The modification is most pronounced at the flanks of the Coulomb peak. This is consistent with Eq. 3.24, where the mechanical motion is shown to modify the current according to a term proportional to $\frac{\partial^2 I}{\partial V_G^2}$. In addition, a softening of the mechanical resonance frequency as V_{G3} is swept across the Coulomb peak is visible. The white curve represents a fit to Eq. 5.9, using the estimated occupation probability shown in Fig. 5.8b. This fit yields an estimate of the electromechanical coupling strength, $g_m/2\pi = 0.16 \pm 0.04$ GHz.

A cryostat temperature of 300 mK corresponds to $k_B T = 0.026$ meV. The estimated tunnel rates yield a total tunnelling rate of $\Gamma_{\text{tot}} = 439$ GHz, corresponding to $\hbar\Gamma_{\text{tot}} = 0.29$ meV such that $\hbar\Gamma_{\text{tot}} \gg k_B T$, confirming our expectation that the device is operating in the lifetime-broadened regime. Furthermore, since $\Gamma_{\text{tot}} \gg \omega_m/2\pi$, the system also satisfies the condition for the quasiadiabatic regime. Lastly, we have $\Gamma_{\text{tot}} \gg g_m/2\pi$ confirming that the conditions for self oscillations are met.

5.5.2 Identification of electromechanical coupling

Fig. 5.10 reproduces the measurement shown in Fig. 5.9, but with V_{G3} swept over a wider range so as to span multiple Coulomb peaks. The lower plot displays the dc current as a function of V_{G3}, showing the Coulomb peaks corresponding to charge transitions in the QD. In addition to the features observed in Fig. 5.9 (the modification of the current when the CNT is driven on resonance and the softening of the mechanical resonance frequency at the Coulomb peaks) a gradual increase in the resonance frequency with decreasing gate voltage is also apparent. The combination of these features confirms the presence of electromechanical coupling in the system and constitutes the completion of the first stage of the measurement protocol described in Section 5.4.

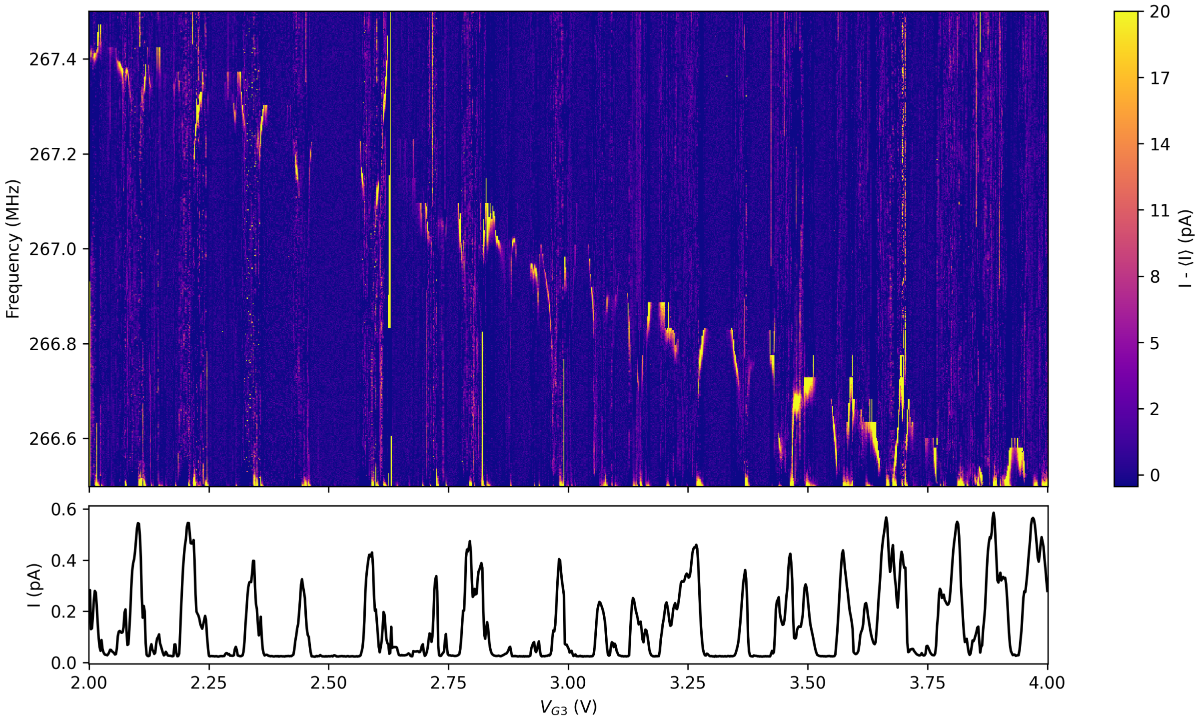

Figure 5.10: Mechanical softening and CNT tensioning. Upper plot: measurement of the dc current through the CNT, shown as the deviation from its average value and plotted as a function of drive frequency and V_{G3}. The drive signal was applied to gate G3 with a power of -81 dBm reaching the gate. The CNT was biased with a source-drain voltage of $V_{SD} = 1$ mV. Lower plot: A cut through the upper plot at a frequency of 266.5 MHz showing dc current as a function of V_{G3}.

5.5.3 RF detection of driven oscillations and challenges

The second stage of the measurement protocol aims to observe driven oscillations of the CNT via the RF measurement chain. In order to achieve this, the resonance frequencies of the CNT and cavity must be closely matched. Given that the resonance frequency of the CNT cannot be determined until it is loaded into the cryostat, this matching necessarily involves a degree of estimation. Previous CNT devices fabricated by the group showed resonance frequencies between 250 and 350 MHz [116, 122]. The device was therefore bonded to a cavity with a room temperature resonance frequency of 325 MHz.

Changes in temperature, along with coupling to the cryostat's RF measurement chain, are expected to shift the resonance frequency of the cavity. With the CNT device installed in the cryostat, an S_{11} measurement was performed to characterize the cavity response indicating that the resonance frequency shifted from 325 MHz at room temperature to 363 MHz at base temperature.

As shown in Fig. 5.9, the mechanical resonance frequency of the CNT was found to be approximately 267 MHz, detuned from the cavity resonance by nearly 100 MHz. To evaluate the RF response of the system without the invasive procedure of removing the CNT device from the cryostat and physically adjusting the cavity, mixing measurements were performed. A simplified schematic of the experimental setup is shown in Fig. 5.11.

Mixing measurements exploit the nonlinearity of the CNT conductance to operate it as a frequency mixer. A low-power voltage signal of frequency ω_S is applied to the source electrode, resulting in an AC current through the CNT at frequency ω_S. Simultaneously, the CNT is driven at its mechanical resonance frequency ω_M. The resulting electromechanical current mixes with the source-driven current, producing sideband signals in the current spectrum at frequencies $\omega_M \pm \omega_S$. The frequency ω_S is chosen such that either $\omega_M + \omega_S$ or $\omega_M - \omega_S$ matches the resonance frequency of the cavity, ω_C, allowing the mixed signal to be coupled to the rf measurement chain. After amplification, the signal is demodulated using a lock-in amplifier referenced to ω_C yielding in-phase, I, and quadrature, Q, components, which are read out using an analogue-to-digital converter. An example

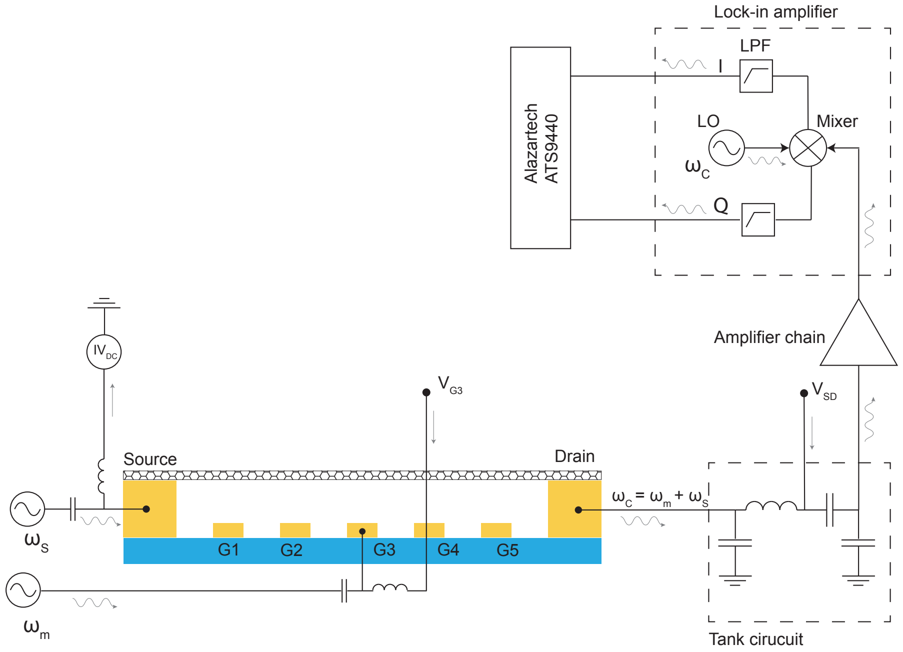

Figure 5.11: Mixing measurement setup, as described in section 5.5.3

of this measurement is shown in Fig. 5.12. The main panel shows the dc current through the CNT, as a function of V_{G3} and drive frequency, with V_{G3} swept across a Coulomb peak. The drive signal was applied with a power of −91 dBm. An electromechanical modulation of the current is visible at approximately 267.6 MHz. To search for a mixing signal, a signal at $\omega_S = 95.4$ MHz with an amplitude of 50 µV was applied to the source electrode, such that the sum frequency $\omega_M + \omega_S = 267.6\text{MHz} + 95.4\text{MHz} = 363\text{MHz}$ matched the cavity resonance frequency ω_C. The inset shows the demodulated signal measured using a lock-in amplifier referenced to $\omega_C = 363$ MHz. The absence of any features in the demodulated output suggests that the mechanically driven current was not being detected by the rf measurement chain. The reason for this was ultimately traced to an issue with the rf measurement setup inside of the cryostat. However, during the troubleshooting process, the CNT device was damaged, meaning it was not possible to proceed with the experiment. The experimental focus of the project therefore needed to revert to the fabrication of devices, as described in Section 3.3.

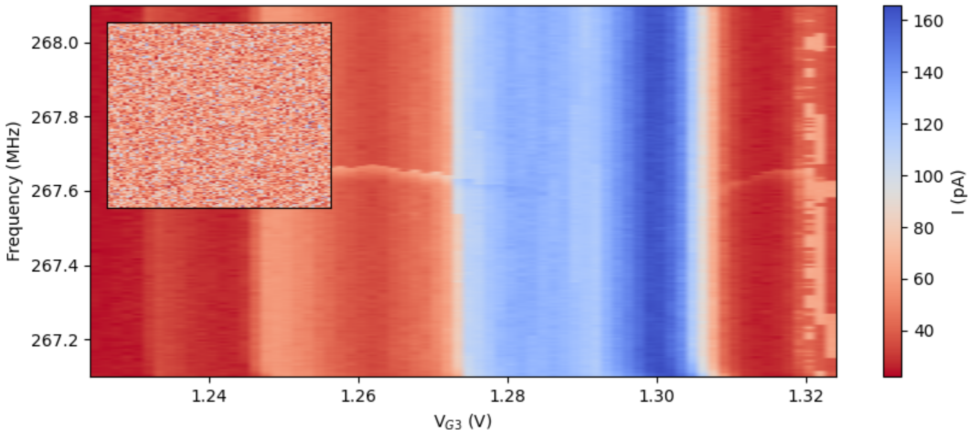

Figure 5.12: Electromechanical mixing measurement. Main panel: dc current through the CNT measured as a function of drive frequency and gate voltage V_{G3}, with V_{G3} swept across a Coulomb peak. The drive power was set to −91 dBm at the gate. A secondary signal at $\omega_S = 95.4$ MHz and amplitude 50 µV was applied to the source electrode, such that the sum frequency $\omega_m + \omega_S = 363$ MHz matched the cavity resonance ω_C. Inset: demodulated signal measured using a lock-in amplifier referenced to ω_C.

5.6 Tick Extraction and Waiting Time Distribution

We saw in Section 2.3 that the performance of a clock can be characterised by its accuracy N and resolution ν defined as

$$\begin{aligned} N &= \left(\frac{t_{\text{tick}}}{\Delta t_{\text{tick}}}\right) \\ \nu &= \frac{1}{t_{\text{tick}}}, \end{aligned} \tag{5.12}$$

where t_{tick} is the mean interval between successive ticks and Δt_{tick} the standard deviation of this interval. To assess the performance of the CNT clock described in the previous sections, it is therefore necessary to determine t_{tick} from the output of the clock's readout mechanism. This section derives a method for optimally performing this analysis, along with an expression for the probability distribution governing the tick-time intervals - the clock's waiting time distribution (WTD).

5.6.1 Optimal tick extraction

The output of the rf measurement chain when the CNT is undergoing self-oscillations is an oscillating voltage that reflects the motion of the CNT. Ticks are extracted from this signal by associating particular events within a cycle, such as zero crossings, with a tick and then identifying the times in the complete signal when this event occurs. The noise inherent in the measured signal means a certain amount of uncertainty is always associated with the identification of ticks. As a result, the choice of tick event as well as the scheme used to extract the ticks affect the accuracy of the clock. Here we show that optimal tick events are zero crossings and that the optimal means of extracting the tick times is a maximum likelihood estimation (MLE).

Optimal tick events

The output of the rf measurement chain is modelled according to

$$y(t) = s(t) + \xi(t), \tag{5.13}$$

where $s(t) = A\sin(\omega t + \phi)$ denotes a clean oscillatory signal, and $\xi(t)$ represents noise introduced as the signal passes through the amplifier chain of the cryostat. We assume that the dominant contribution to the noise is thermal in origin and can be modelled as broadband Johnson noise. We therefore take $\xi(t)$ to be distributed according to

$$\xi(t) \sim \mathcal{N}(0, \sigma^2), \tag{5.14}$$

with a correlation time that is much shorter than the period of the oscillating signal. A tick of the clock occurs when the measured signal satisfies the condition

$$y(t) = L, \tag{5.15}$$

for some reference level L. For instance, if ticks are associated with zero crossings, then $L = 0$. Let t_0 be the time at which the clean signal satisfies this condition, so that $s(t_0) = L$. The actual time t_L at which the noisy signal satisfies 5.15 condition is then given by

$$t_L = t_0 + \delta t, \tag{5.16}$$

where δt is the timing error introduced by the noise. By definition, this means

$$y(t_0 + \delta t) = L. \tag{5.17}$$

Expanding $s(t_0 + \delta t)$ to first order and substituting into Eq. 5.17 gives

$$s(t_0) + \dot{s}(t_0)\delta t + \xi(t_0 + \delta t) = L. \tag{5.18}$$

Since $s(t_0) = L$, Eq. 5.18 yields

$$\delta t \simeq -\frac{\xi(t_0 + \delta t)}{\dot{s}(t_0)}, \tag{5.19}$$

such that

$$|\delta t| \simeq \left|\frac{\xi(t_0)}{\dot{s}(t_0)}\right|, \tag{5.20}$$

where we have assumed that the correlation time of the noise is much shorter than δt. To minimise the timing error, it is therefore necessary to choose L such that the slope of $s(t)$ at t_0 is maximised. The derivation above is only valid to first order in δt causing the timing error to diverge as $\dot{s}(t_0) \to 0$. While this divergence could be removed by including higher-order terms in the Taylor expansion of $s(t)$, the first-order result is sufficient to demonstrate that the timing error is minimised at points of maximal slope. Given the sinusoidal form of $s(t)$, Eq. 5.20 associates optimal tick locations with zero-crossings.

Optimal tick extraction scheme

In order to identify the optimal method for extracting ticks from the noisy signal we realise that the determination of a particular tick event is equivalent to the estimation of the phase of the sinusoid describing the oscillation at the time of the event [86]. The idea is illustrated in Fig. 5.13 using simulated noisy data. The noisy signal is discretised into n windows of time $2t_r$ centred around the n expected tick locations, with the n^{th} window

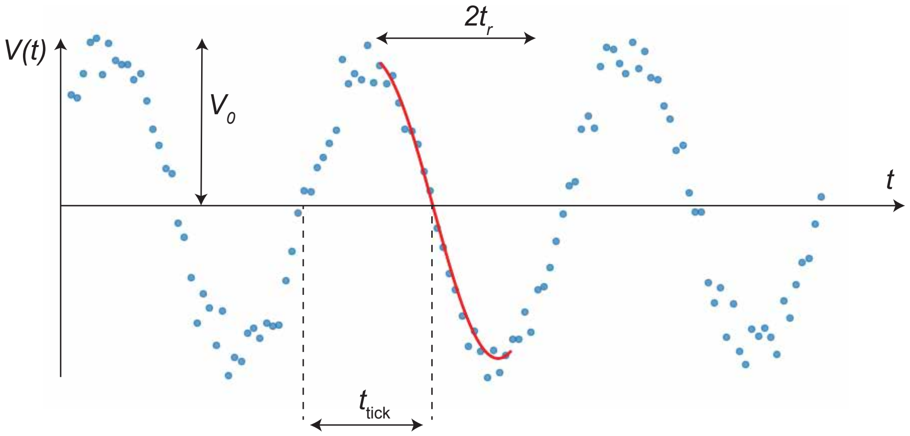

Figure 5.13: Representation of the tick extraction scheme using simulated data. Ticks are extracted from noisy data by fitting a sinusoid around zero crossings. Here, t_{tick} denotes the time between successive ticks, $2t_r$ represents the interval over which the sinusoid is fitted, and V_0 is the amplitude of the oscillation.

described by

$$V(t \mid \phi_n) = V_0 \sin(\omega t + \phi_n) \quad \text{with} \quad n \times t_{\text{tick}} - t_r \leq t \leq n \times t_{\text{tick}} + t_r \quad \text{for } n \in \mathbb{Z}, \tag{5.21}$$

where the ticks have been assigned to both upward and downward zero crossing events and t_{tick} is the time between ticks. The amplitude V_0 and angular frequency ω of the oscillation associated with the n^{th} window vary slowly and can therefore be determined by considering a sequence of oscillations centred around the n^{th} tick, leaveing ϕ_n as the only parameter to be determined. Once this has been achieved it is a simple matter of extracting the time of the n^{th} tick using

$$t^n_{\text{tick}} = \frac{n\pi - \phi_n}{\omega}. \tag{5.22}$$

We now demonstrate that MLE is the optimal method for extracting the phase of the oscillation in the n^{th} window from noisy data. MLE is asymptotically efficient, meaning that in the limit of an infinite number of samples, the variance of the estimator $\hat{\phi_n}$ saturates the Cramér-Rao (CR) bound, which is given by

$$\text{Var}[\hat{\phi_n}] \geq \frac{1}{\mathcal{I}(\phi_n)}, \tag{5.23}$$

where $\mathcal{I}(\phi_n)$ denotes the Fisher information of the parameter ϕ, given by

$$\mathcal{I}(\phi_n) = \mathbb{E}\left[\left(\frac{\partial}{\partial\phi_n}\log\mathcal{L}(\phi_n)\right)^2\right], \tag{5.24}$$

where $\mathcal{L}(\phi_n)$ is the likelihood function associated with the phase of the n^{th} window. By saturating the CR bound, MLE achieves the minimum possible variance among all unbiased estimators, implying that no other method can estimate ϕ with a lower mean squared error. While this saturation strictly occurs in the asymptotic limit, it can be approached in practice with a finite, yet sufficiently large, number of samples. To demonstrate this, we compare the variance of $\hat{\phi}$, obtained from simulated noisy data, with $\mathcal{I}(\phi)^{-1}$ as a function of the sample size. The assumption of Johnson noise with a fast correlation time made above allows us to write the likelihood function for the parameter ϕ_n as

$$\mathcal{L}(\phi_n) = \prod_{i=1}^{M}\frac{1}{\sqrt{2\pi\sigma^2}}\exp\left(-\frac{1}{2\sigma^2}\left(v_i - V_0\sin(\omega t_i + \phi_n)\right)^2\right), \tag{5.25}$$

where v_i is the i^{th} of the M samples of the n^{th} window and σ is the standard deviation of the noise. Discarding constants, the log-likelihood becomes

$$\log\mathcal{L}(\phi_n) = -\frac{1}{2\sigma^2}\sum_{i=1}^{M}\left(v_i - V_0\sin(\omega t_i + \phi_n)\right)^2, \tag{5.26}$$

from which we compute the derivative

$$\frac{\partial\log\mathcal{L}(\phi_n)}{\partial\phi} = \frac{V_0}{\sigma^2}\sum_{i=1}^{M}\left(v_i - V_0\sin(\omega t_i + \phi_n)\right)\cos(\omega t_i + \phi). \tag{5.27}$$

The Fisher information is then given by

$$\mathcal{I}(\phi_n) = \mathbb{E}\left[\frac{V_0}{\sigma^2}\sum_{i=1}^{M}\left(v_i - V_0\sin(\omega t_i + \phi_n)\right)\cos(\omega t_i + \phi)\right]^2. \tag{5.28}$$

To evaluate this expectation value, we model the observed data as

$$v_i = V_0\sin(\omega t_i + \phi_n) + n_i, \quad \text{with} \quad n_i \sim \mathcal{N}(0, \sigma^2). \tag{5.29}$$

Substituting into Eq. 5.28, we obtain

$$\mathcal{I}(\phi_n) = \frac{V_0^2}{\sigma^4}\mathbb{E}\left[\left(\sum_{i=1}^{M} X_i\right)^2\right], \tag{5.30}$$

where

$$\begin{aligned} X_i &= (v_i - V_0 \sin(\omega t_i + \phi_n))\cos(\omega t_i + \phi) \\ &= n_i \cos(\omega t_i + \phi_n). \end{aligned} \tag{5.31}$$

Expanding the squared term in Eq. 5.30 yields

$$\mathcal{I}(\phi_n) = \frac{V_0^2}{\sigma^4}\left(\sum_{i=1}^{M} \mathbb{E}[X_i^2] + \sum_{i \neq j}^{M} \mathbb{E}[X_i X_j]\right). \tag{5.32}$$

Since the noise is uncorrelated, the cross terms vanish, giving

$$\begin{aligned} \mathcal{I}(\phi_n) &= \frac{V_0^2}{\sigma^4}\sum_{i=1}^{M} \mathbb{E}\left[(n_i \cos(\omega t_i + \phi_n))^2\right] \\ &= \frac{V_0^2}{\sigma^4}\sum_{i=1}^{M} \mathbb{E}[n_i^2]\,\mathbb{E}[\cos^2(\omega t_i + \phi_n)] \\ &= \frac{M V_0^2}{2\sigma^2}, \end{aligned} \tag{5.33}$$

so that

$$\mathcal{I}(\phi_n)^{-1} = \frac{2\sigma^2}{M V_0^2} = \frac{1}{M}\cdot\frac{1}{\mathrm{SNR}}, \tag{5.34}$$

where SNR denotes the signal-to-noise ratio of the measured signal. Figure 5.14 compares $\mathcal{I}(\phi_n)^{-1}$ with $\mathrm{Var}(\hat{\phi_n})$ as a function of the number of samples M. The variance $\mathrm{Var}(\hat{\phi_n})$ was computed from simulated noisy data with an SNR of 3 dB, with each estimate based on 100 trials. The figure illustrates that $\mathrm{Var}(\hat{\phi_n})$ converges to $\mathcal{I}(\phi_n)^{-1}$ as the sample size increases, with good agreement observed beyond approximately 50 samples after which fluctuations in $\mathrm{Var}(\phi_n)$ die out. We conclude that 50 samples are sufficient for MLE to achieve near-optimal performance in phase extraction for signals with SNR $\geq$ 3 dB. Should the experimental data exhibit an SNR below this threshold a similar analysis could be carried out to ensure convergence.

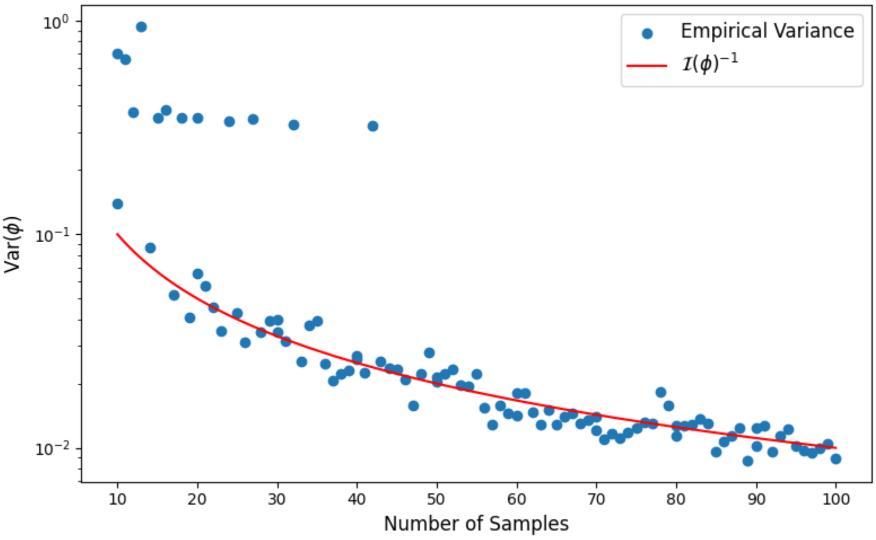

Figure 5.14: Comparison of the variance of the phase estimated from simulated data with an SNR of 3 dB using MLE, against the asymptotic variance computed via $\mathcal{I}(\phi)^{-1}$. The variance at each data point is calculated from 100 trials.

5.6.2 Clock waiting time distribution

The expressions for the accuracy and resolution of a clock, given by Eq. 5.12, are statistical properties of the clock's tick record, constructed to quantify its performance with two real numbers. Whilst these quantities provide meaningful insights into a clock's performance, a full characterisation of the statistical properties of the tick record requires an understanding of the distribution of tick times underlying these two measures. Here we derive an expression for this distribution which we refer to as the clock's WTD.

As described in Section 5.2.2, the self-sustained oscillations observed in suspended CNT devices arise from the formation of a limit cycle, driven by electromechanical coupling. An ideal limit cycle would exhibit time-independent amplitude and phase, with oscillations described by

$$V = V_0 \sin(\psi), \tag{5.35}$$

where $\psi = \omega_0 t + \phi$, with $\omega_0/2\pi$ the frequency of the oscillator. In Section 5.6.1 we saw how amplitude fluctuations, originating from interaction between the oscillating signal emerging from the CNT and the rf measurement chain, cause the measured tick time to deviate from the true tick time t_0 by an amount δt. Additionally, we saw in Section

5.2.2 that the probabilistic nature of electron tunnelling events cause the oscillations of the CNT to have a stochastic component with their dynamics described by a stochastic differential equation (Eq. 5.11). In [28], it is shown that this stochasticity translates to amplitude and phase fluctuations of the limit cycle given by

$$\begin{aligned} \mathrm{d}V &= -\gamma_V (V - V_0)\,\mathrm{d}t + \sqrt{D_V}\,\mathrm{d}W_V, \\ \mathrm{d}\psi &= \omega_0\,\mathrm{d}t + \sqrt{D_\psi}\,\mathrm{d}W_\psi, \end{aligned} \tag{5.36}$$

where, γ_V is the damping coefficient that governs the relaxation of amplitude fluctuations back to the limit cycle, dW_V and dW_ψ are independent Wiener increments, and D_V and D_ψ are the corresponding diffusion coefficients. To derive an expression for the clock's WTD, we must therefore consider both amplitude and phase noise.

Amplitude noise

Two sources of amplitude noise are present in the system: additive Gaussian noise, of the form discussed in Section 5.6.1, and fluctuations originating from the clock dynamics, described by Eq. 5.36. It is shown in Ref. [28] that $\gamma_V \gg D_\psi$ suggesting that amplitude fluctuations originating from the clock's dynamics are fast and short-lived in comparison with the phase fluctuations. We therefore make the assumption that the dominant source of amplitude noise in the tick record is additive Gaussian noise deriving from the signal's interaction with the cryostat's measurement chain.

In order to derive an expression of the WTD of the clock in the presence of amplitude noise alone, we note that, in Section 5.6.1, we reformulated the problem of estimating the time of the n^{th} tick as one of estimating the phase of the n^{th} oscillation. An uncertainty in the phase of the n^{th} oscillation translates into an uncertainty in the time of the n^{th} tick, given by

$$\delta t_n = \frac{\delta\phi_n}{\omega_0}. \tag{5.37}$$

From Eq. 5.34, the variance of $\delta\phi_n$ is

$$\mathrm{Var}[\delta\phi] = \frac{2\sigma^2}{MV_0^2}, \tag{5.38}$$

giving

$$\mathrm{Var}[\delta t] = \frac{2\sigma^2}{M\omega_0^2 V_0^2}. \tag{5.39}$$

If the n^{th} tick occurs at time t_n, given by

$$t_n = t_n^{(0)} + \delta t_n \tag{5.40}$$

where $t_n^{(0)}$ is the true crossing time of the n^{th} tick, then the time between consecutive ticks T_n is given by

$$T_n = t_{n+1} - t_n = (t_{n+1}^{(0)} + \delta t_{n+1}) - (t_n^{(0)} + \delta t_n) = (t_{n+1}^{(0)} - t_n^{(0)}) + (\delta t_{n+1} - \delta t_n). \tag{5.41}$$

With ticks assigned to zero-crossings, true ticks are separated by half an oscillation period such that we can write Eq. 5.41 as

$$T_n = T_0 + (\delta t_{n+1} - \delta t_n), \tag{5.42}$$

where T_0 is the true time between ticks given by π/ω_0. Fluctuations around T_0 are then given by

$$\Delta T_n = \delta t_{n+1} - \delta t_n. \tag{5.43}$$

Given we have assumed the noise $\xi(t)$ to be i.i.d we can write

$$\mathrm{Var}[T_n] = \mathrm{Var}[\delta t_{n+1} - \delta t_n] = \mathrm{Var}[\delta t_{n+1}] + \mathrm{Var}[\delta t_n] = 2\,\mathrm{Var}[\delta t_n]. \tag{5.44}$$

Therefore

$$\mathrm{Var}[T_n] = \frac{2\sigma^2}{MV_0^2\omega_0^2}. \tag{5.45}$$

Eq.5.45 is derived under the assumption that the amplitude noise present in the measured signal is thermal in origin and follows a normal distribution given by

$$\xi(t) \sim \mathcal{N}(0, \sigma^2). \tag{5.46}$$

In the absence of phase noise, the WTD of the clock is therefore given by

$$T_n \sim \mathcal{N}\left(T_0, \frac{2\sigma^2}{MV_0^2\omega_0^2}\right). \tag{5.47}$$

Phase noise

From Eq. 5.36 we see that the evolution of the clock's phase is described by a Weiner process

$$\psi(t) = \omega_0 dt + \sqrt{D_\psi} W_\psi(t). \tag{5.48}$$

With ticks assigned to zero-crossings, in the absence of noise we have

$$\omega_0 t_n^{(0)} = \pi n. \tag{5.49}$$

In the presence of noise from 5.48 this condition becomes

$$\omega t_n + \sqrt{D_\psi} W_\psi(t_n) = n\pi, \tag{5.50}$$

where $t_n = t_n^{(0)} + \delta t_n$ such that

$$\omega_0(t_n^{(0)} + \delta t_n) + \sqrt{D_\psi} W_\psi(t_n^{(0)} + \delta t_n) = n\pi. \tag{5.51}$$

Given that $\omega t_n^{(0)} = n\pi$ we can write Eq. 5.51 as

$$\omega_0 \delta t_n + \sqrt{D_\psi} W_\psi(t_n^{(0)} + \delta t_n) = 0, \tag{5.52}$$

giving

$$\delta t_n = -\frac{\sqrt{D_\psi}}{\omega_0} W_\psi(t_n^{(0)} + \delta t_n) \tag{5.53}$$

Since the variance of a Weiner process $W(t)$ is t, we can write

$$\mathrm{Var}[\delta t_n] = \frac{D_\psi}{\omega_0^2}(t_n^{(0)} + \delta t_n), \tag{5.54}$$

If $t_n^{(0)} \gg \delta t_n$ then we can write

$$\mathrm{Var}[\delta t_n] = \frac{D_\psi}{\omega_0^2} t_n^{(0)}. \tag{5.55}$$

Given that the dynamics of $\psi(t)$ are described by a Weiner process, the variance of the time between ticks T_n is given by

$$\mathrm{Var}[T_n] = \mathrm{Var}[\delta t_{n+1}] + \mathrm{Var}[\delta t_n] - 2\ \mathrm{Cov}[\delta t_{n+1}, \delta t_n], \tag{5.56}$$

where

$$\mathrm{Cov}[\delta t_{n+1}, \delta t_n] = \frac{D_\psi}{\omega_0^2} t_n^{(0)}, \tag{5.57}$$

such that

$$\begin{aligned} \mathrm{Var}[T_n] &= \frac{D_\psi}{\omega_0^2}\left(t_{n+1}^{(0)} + t_n^{(0)} - 2t_n^{(0)}\right) \\ &= \frac{D_\psi}{\omega_0^2}\left(t_{n+1}^{(0)} - t_n^{(0)}\right) \\ &= \frac{D_\psi}{\omega_0^2}\frac{\pi}{\omega_0} \\ &= \frac{\pi D_\psi}{\omega_0^3}. \end{aligned} \tag{5.58}$$

In the absence of amplitude noise, the distribution of tick times becomes a first-passage time distribution for the phase of the oscillation. When ticks are assigned to zero crossings, this corresponds to the first-passage time for the phase to reach π. Given a Weiner process with drift coefficient ω_0 and diffusion coefficient D_ψ

$$\psi(t) = \omega_0 dt + \sqrt{D_\psi} W_t, \tag{5.59}$$

The first passage of time τ_α for a fixed level α is distributed according to an inverse Gaussian distribution with mean μ and shape parameter λ

$$\tau_\alpha \sim \mathrm{IG}\Big(\mu, \lambda\Big), \qquad \mu = \frac{\alpha}{\omega_0}, \quad \lambda = \frac{\alpha^2}{D_\psi}. \tag{5.60}$$

The pdf is given by

$$f_{\tau_\alpha}(t) \;=\; \sqrt{\frac{\lambda}{2\pi t^3}}\, \exp\!\Big[-\frac{\lambda\,(t-\mu)^2}{2\mu^2 t}\Big], \tag{5.61}$$

with variance

$$\mathrm{Var}[\tau_\alpha] = \frac{\mu^3}{\lambda}. \tag{5.62}$$

We therefore have that the phase noise of the oscillator causes the tick times to be distributed according to

$$T_n \sim \mathrm{IG}\left(T_0, \frac{\pi^2}{D_\psi}\right) \tag{5.63}$$

with

$$\mathrm{Var}[T_n] = \frac{\pi^3}{\omega_0^3} \cdot \frac{D_\psi}{\pi^2} = \frac{\pi D_\psi}{\omega_0^3}, \tag{5.64}$$

which matches the expression for the variance derived above.

Full waiting time distribution

Eqs. 5.47 and 5.63 describe the WTDs of the clock arising from amplitude and phase noise respectively, in the absence of the other. To derive the full WTD we assume that amplitude and phase fluctuations are independent. This assumption is justified by the fact that the physical origins of amplitude and phase noise are distinct: amplitude noise arises primarily from interaction between the clock's signal with the cryostat's amplifier chain, while phase noise is a consequence of the stochastic dynamics of the oscillator's phase. We therefore introduce zero-mean fluctuations

$$\Delta T_n^A \sim \mathcal{N}\Big(0, \sigma_A^2\Big), \qquad \Delta T_n^\psi = T_n^\psi - T_0, \quad T_n^\psi \sim \mathrm{IG}\Big(T_0, \lambda_\psi\Big), \tag{5.65}$$

with

$$\sigma_A^2 = \frac{2\sigma^2}{MV_0^2\omega_0^2}, \qquad \lambda_\psi = \frac{\pi^2}{D_\psi}. \tag{5.66}$$

The random variable representing the waiting time of the clock's ticks is then given as

$$T_n = T_0 + \Delta T_n^A + \Delta T_n^\psi, \tag{5.67}$$

which has mean T_0 and variance given by

$$\begin{aligned}\mathrm{Var}[T_n] = \mathrm{Var}[\Delta T_n^A] + \mathrm{Var}[\Delta T_n^\psi] &= \frac{2\sigma^2}{MV_0^2\omega_0^2} + \frac{\pi D_\psi}{\omega_0^3} &(5.68)\\ &= \frac{1}{M\omega_0^2}\cdot\frac{1}{SNR} + \frac{\pi D_\psi}{\omega_0^3}. &(5.69)\end{aligned}$$

The pdf of the clock's WTD is then given by the convolution

$$p_T(t) = \int_{-\infty}^{\infty} p_A(\tau)\, p_\psi(t - T_0 - \tau))\,\mathrm{d}\tau, \tag{5.70}$$

with

$$p_A(\tau) = \frac{1}{\sqrt{2\pi\sigma_A^2}}\exp\Big[-\tfrac{\tau^2}{2\sigma_A^2}\Big], \qquad p_\psi(u) = \sqrt{\frac{\lambda_\psi}{2\pi(u+T_0)^3}}\exp\Big[-\tfrac{\lambda_\psi\left(u\right)^2}{2T_0^2(u+T_0)}\Big]. \tag{5.71}$$

As discussed in 5.1, the CNT clock is distinctive in that its readout mechanism, the oscillating current generated by the self-oscillating CNT, is intimately connected to the clockwork itself. The amplitude of the oscillating current emerging from the CNT is far too small to be measured directly and therefore requires amplification. The amplitude noise added to the clock's signal and its subsequent affect on the performance of the clock is dependent on the specific measurement setup used to carry out this amplification. Ultimately, the ability of the measurement setup to extract information from a signal is constrained by fundamental limits imposed by quantum mechanics. For a continuous phase preserving measurement of a SHO the displacement sensitivity is bounded by the standard quantum limit (SQL) [121]

$$\sqrt{S_{uu}(\mathrm{SQL})} = \sqrt{\frac{\hbar Q_M}{4\pi^2 m f^2}}, \tag{5.72}$$

where Q is the quality factor of the oscillator, m its mass, and f its resonance frequency. In Ref. [121] a displacement sensitivity of roughly 30 times the SQL is achieved with a measurement setup similar to the one described in 5.3.1, but without the SQUID amplifier. Although the addition of a SQUID amplifier will bring the displacement sensitivity closer to the SQL, the ultimate displacement sensitivity will still depend on the specifics of the measurement setup. We therefore choose to focus on how the performance of the clock is limited by the phase noise intrinsic to the clock's dynamics. From a given tick record and a measurement of the clock's SNR we can use Eq. 5.68 to compute $\mathrm{Var}[\Delta T_n^\psi]$. The dependence of the accuracy of the clock on the phase noise alone is then given by

$$N_\psi = \frac{T_0}{\mathrm{Var}[\Delta T_n^\psi]}. \tag{5.73}$$

5.7 Clock Thermodynamics

Section 5.4 described the experimental procedures required to observe self-oscillations in a suspended CNT device and the resulting oscillating current. Section 5.6 outlined how ticks can be optimally extracted from this signal, as well as a method for isolating the fluctuations originating from the clock's dynamics. This section brings these elements together by describing the measurements that can be performed on the CNT clock to investigate its thermodynamic properties, along with the expected outcomes of these measurements.

5.7.1 Entropy production

The primary goal of the experiment is to investigate how the performance of the CNT clock is related to the dissipation associated with its operation. The clock is driven by a bias applied between the source and drain electrodes, with the resulting current playing a key role in the electromechanical mechanism that causes the clock to tick (see Section 5.2.2). The entropy production associated with the clock's operation is proportional to the power dissipated in the circuit containing the QD. For a source drain bias of V_{SD}, the average entropy production rate is given by [28]

$$\dot{\sum} = \frac{\langle I \rangle V_{\mathrm{SD}}}{T}, \tag{5.74}$$

where T is the temperature of the electrons in the electrodes (assumed to be the same for source and drain) and $\langle I \rangle$ is the average current through the CNT. As we saw in Section 5.7 the suspended CNT device cannot operate as a clock in isolation; to provide a useful reference for measuring time it must be coupled to readout mechanism. For the setup described here the readout mechanism consists of the cavity to which the CNT is coupled as well as the amplifier of the cryostat. Clearly, the readout mechanism will introduce further sources of dissipation. This dissipation depends on the specifics of the measurement setup and, for small systems, tends to dominate over the dissipation associated with clock's clockwork [117]. We therefore ignore these sources of dissipation and focus exclusively on the dissipation described by Eq. 5.74.

5.7.2 Measurements

We aim to investigate how the performance of the clock is related to the dissipation associated with its operation. From Eq. 5.74, we see that the rate of entropy production is proportional to V_{SD} and $\langle I \rangle$. The appropriate approach is therefore to measure tick records as a function of V_{SD} via the rf measurement chain, while simultaneously recording the average current through the CNT using the dc measurement setup described in Section 5.3.1. An indication of the outcomes of these measurements can be obtained from the model developed in Ref. [28] and outlined in Section 5.2.2. Figure 5.15, taken from Ref. [28], shows the WTD generated from data simulated using this model for three different values of V_{SD}. Dots represent simulated data and solid curves show best fits to inverse Gaussian distributions described by Eq. 5.61 with λ and μ as fitting parameters.

This image has been removed the publicly available version of this thesis due to copyright restrictions

Figure 5.15: WTD for the clock described by the model of Ref. [28]. The figure is taken from [28]. Dots represent the distribution with data obtained via numerical simulation. Solid curves are lines of best fit to inverse Gaussian distributions described by Eq. 5.61 with fitting parameters λ and μ.

This image has been removed the publicly available version of this thesis due to copyright restrictions

Figure 5.16: Thermodynamic trade-offs present in the clock described by the model of Ref. [28]. Accuracy (red line) and resolution (blue line) of the clock described by the model of Ref. [28] as a function of entropy production per tick. Figure adapted from Ref. [28]

Notably, increasing V_{SD} causes the variance of the distribution to decrease, indicating an increase in the accuracy of the clock. To understand this relationship between V_{SD} and the clock's accuracy, we note that the self oscillations of the CNTQD system are driven by the bias across the CNT. As a result, increasing V_{SD} causes the amplitude of the oscillations to increase [122]. Increasing the amplitude of the oscillations increases the SNR of the measured signal, which, via Eq. 5.34 decreases in the variance in the estimated phase of the oscillation increasing the accuracy of the clock. Figure 5.16, also taken from Ref [28], shows accuracy and resolution of the clock as a function of entropy production per tick. An approximately linear relationship between accuracy and entropy production is initially visible as V_{SD} increases; however, as V_{SD} continues to rise, the growth in accuracy slows and eventually saturates suggesting that a value of V_{SD} exists beyond which the amplitude of the oscillations no long increases. The clock's resolution decreases with increasing entropy and eventually saturates. The change in resolution is minimal however, which is to be expected given the clock's period is fixed by the oscillator's frequency.

Assuming the model presented in Section 5.2.2 effectively captures the dynamics of the self-oscillating CNT system, figures 5.15 and 5.16 demonstrate that the accuracy of the CNT clock can only be improved at the cost of increased dissipation. Experimental verification of this trade-off would align with previous studies [86, 117], contributing to a growing body of work that establishes a fundamental connection between thermodynamics and timekeeping [38,76,79,98,126].

5.8 Conclusion

In this chapter, we have introduced a nanomechanical clock based on a suspended CNTQD system and established an experimental platform capable of reading out the ticks of the clock whilst simultaneously measuring the dissipation associated with its operation.

Unfortunately, the failure of the CNT device used in the experiment meant that the clock could not be fully realised. This chapter has therefore presented a summary of the progress made to date toward its implementation. Experimentally, this included the development of the experimental platform, along with measurements of key device parameters such as tunnelling rates and electromechanical coupling strength. These measurements confirmed that the device operated in the quasiadiabatic regime demonstrating that, in principle, the self-oscillations, which form the basis of the clock's operation, could be observed. A complete measurement protocol was presented for observing real-time self oscillations of the CNT and measuring the thermodynamic trade-offs associated with the operation of the CNTQD system as a nanomechanical clock, thereby establishing a clear methodology for future experiments.

In support of this experimental work, a set of theoretical results were also derived. It was shown that the optimal method for extracting ticks from the measured tick record involves assigning ticks to zero-crossing events and then using an MLE to extract the phase of the oscillation associated with each zero crossing. Additionally, an expression was derived for the clock's WTD. It was shown that the variance of the WTD could be decomposed into contributions from phase and amplitude fluctuations, originating from the clock's dynamics and amplifier noise respectively.

Finally, a framework for quantifying the dissipation associated with the clock's operation was outlined, with the entropy production proportional to the power dissipated in circuit containing the QD. Importantly, the decomposition of the variance of the clock's WTD into contributions from the intrinsic clock dynamics and external amplifier noise allows the clock's performance to be assessed solely in terms of the physical processes responsible for this dissipative behaviour.

Taken together the work presented in this chapter lays the groundwork for the first experimental study of a truly autonomous quantum electromechanical clock and establishes a clear methodology for quantifying the connection between its performance and the thermodynamic resources it consumes.

6

Conclusion

In Chapter 4 we saw how the work cost required to erase a bit of information instantiated in the occupancy of a QD is affected by the application of bias across the QD. In the context of LE this amounted to performing erasure in the presence of two reservoirs with different electrochemical potentials, a deviation from the conventional approach where a single reservoir is considered. By varying the relative electrochemical potentials of the two reservoirs, we were able to measure how the work cost of erasure is modified as erasure is performed in the context of a non-equilibrium system. We saw that, not only is the work cost modified, but that the introduction of a second reservoir to the erasure process introduces an asymmetry in the work cost to erase to zero and work cost to erase to one. In addition, we saw how the two-fold degeneracy of the energy level of the QD introduced a further asymmetry between the work to erase to zero and one, which became manifest when the rate at which erasure was carried out deviated from the quasistatic limit. Taken together, these results show how the physical properties of the QD system influence the work required to erase information as the idealised constraints underlying the LB (a single reservoir and quasistatic erasure) are relaxed.

The QD system discussed in this thesis may not represent a practical platform for the large scale information processing required for today's digital technologies. In his 1961 paper Landauer sought to place fundamental thermodynamic limits on all of computation [71]. Here, by accounting for the effect of an additional reservoir on the work cost of erasure, we have shown how limits can be placed on the work cost of erasure in a system whose architecture more closely resembles existing digital technologies than those studied by Landauer and in previous experimental works. In doing so we have shown that additional considerations may need to be made as information processing technologies approach their fundamental limits. For example, we saw that the two fold degeneracy of our system played an important role in the erasure process and that asymmetries developed between the work cost to erase to zero and one as erasure in our system departed from equilibrium. But perhaps more importantly we have shown that fundamental limits can, in principle, be established for systems with relevance to present technologies. Establishing such limits provides a target for future technologies to aim toward and may ultimately guide the development of more efficient devices.

In Chapter 5, we presented a complete framework for the experimental realisation of a nanomechanical clock. The proposed clock would be novel for several reasons: it would represent the first nanomechanical clock whose theoretical description requires a quantum mechanical element; the clockwork and readout mechanism, normally distinct physical systems, are combined into a single mechanism; and it would be the first truly autonomous clock to be studied in the context of the thermodynamics of timekeeping. Although technical limitations prevented the completion of the experiment, a full investigation into the thermodynamics associated with the clock's operation represents, for the reasons outlined above, a valuable addition to the literature on the thermodynamics of timekeeping.

The goal of this thesis was to leverage the properties of semiconducting nanoscale devices to investigate the thermodynamics of information erasure and timekeeping. With respect to information erasure, this goal was achieved, resulting in the findings summarised above. With respect to timekeeping, only a partial completion of the goal could be realised. Despite this, the work presented here advances our understanding of the thermodynamic limits of these processes and identifies opportunities for further investigation in the future.

Appendices

A

Matching Derivation

Here we demonstrate the equivalence between the circuit described by Eq. 3.27 and a series LCR circuit. Writing Eq. 3.27 in terms of its real an imaginary parts we have

$$Z_{\text{load}} = \frac{R_S}{1+\omega^2 C_S^2 R_S^2} + j\omega L - \frac{j\omega C_S R_S^2}{1+\omega^2 C_S^2 R_S^2}. \tag{A.1}$$

Using the condition $\omega R_S C \gg 1$ Eq. A.1 reduces to

$$Z_{\text{load}} = \frac{1}{\omega^2 C_S^2 R_S} + j\omega L + \frac{1}{j\omega C_S}. \tag{A.2}$$

At the angular resonance frequency $\omega_0 = \frac{1}{\sqrt{LC_S}}$ we have

$$Z_{\text{load}} = \frac{L}{R_S C_S}, \tag{A.3}$$

such that on resonance we can treat Eq. 3.27 a series LCR circuit with and effective resistance

$$R_{\text{eff}} = \frac{L}{R_S C_S}. \tag{A.4}$$

B

Recipes For Carbon Nanotube Fabrication

Here we provide details of the recipes used in the fabrication of CNTs, as outlined in Section 3.3.

B.1 Lithography

B.1.1 Photolithography

Bonding pads and global markers were fabricated using photolithography according to the following recipe

1. Clean the silicon chip with Piranha (3:1 mixture of H_2SO_4 and H_2O_2)
2. Spin coat a layer of MICOPOSIT S1813 photoresist at 150 rpm for 15 seconds then 4000 rpm for 30 seconds
3. Soft bake at 110°C for 45 seconds

4. Expose to UV light at 14 mW/ cm^2 for 15 seconds
5. Develop the photoresist in MF319 developer for 2 minutes
6. *Descum*[1] using oxygen plasma at 200 W for 2 minutes
7. Deposit metals using ebeam evaporator Ti/Au (10/20 nm)
8. Perform lift off by soaking in acetone warmed to 50°C for 2 minutes then sonicating on low power for 30 seconds

B.1.2 Electron beam lithography

Gates were fabricated according to the following recipe

1. Spin-coat a layer of PMMA 950 A2 photoresist at 1000 rpm for 1 minute
2. Soft-bake the sample at 180°C for 2 minutes
3. Pattern the resist using the EBL system in EOS mode 4, aperture 1 (beam current: 100 pA)
4. Expose the resist with a dose of 300 $\mu C/cm^2$
5. Develop the exposed resist in H_2O:IPA (3:7) for 30 seconds, followed by a rinse in IPA
6. Deposit metals using ebeam evaporator Ti/Au (5/35 nm)
7. Perform lift off by soaking in acetone warmed to 50°C for 2 minutes then sonicating on low power for 30 seconds

Source and drain electrodes were fabricated accoring to the following recipe

1. Spin-coat a layer of PMMA 495 A4 photoresist at 3000 rpm for 1 minute
2. Soft-bake the sample at 180°C for 2 minutes

---

[1] Descumming refers to the process of removing residual resist and organic materials that could inhibit metal adhesion.

3. Spin-coat a layer of PMMA 950 A4 photoresist at 5000 rpm for 1 minute
4. Soft-bake the sample at 180°C for 2 minutes
5. Pattern the resist using the EBL system in EOS mode 4, aperture 1 (beam current: 100 pA)
6. Expose the resist with a dose of 340 μC/cm^2
7. Develop the exposed resist in H_2O:IPA (3:7) for 45 seconds, followed by a rinse in IPA
8. Deposit metals using ebeam evaporator Ti/Au (5/95 nm)
9. Perform lift off by soaking in acetone warmed to 50°C for 2 minutes then sonicating on low power for 30 seconds

B.2 Bi-layer Lift-off

We found the following recipe significantly reduced the damage to chips during the lift-off process. The process is described here for patterning the pads and global markers, but can easily adapted to pattern the source/ drain and gates.

1. Clean the silicon chip with Piranha (3:1 mixture of H_2SO_4 and H_2O_2)
2. Spin-coat a layer of LOR photoresist at 150 rpm for 15 seconds then 4000 rmp for 30 seconds
3. Soft-bake at 150°C for 5 minutes
4. Spin-coat a layer of MICROPOSIT S1813 photoresist at 150 rpm for 15 seconds then 4000 rpm for 30 seconds
5. Soft-bake at 110°C for 45 seconds
6. Expose with a dose of 210 mJ/cm^2

7. Develop the resist in MF319 for 2 minutes

8. Plasma clean

9. Deposit metals using ebeam evaporator Ti/Au (10/20 nm)

10. Perform lift off by soaking in warm acetone 50°C for 2 minutes then sonicating on low power for 30 seconds

B.3 Quartz Pillars

Quartz pillars were fabricated using reactive ion etching according to the following recipe, with the etching parameters chosen according to standard recipes developed in the clean room facility in which the ICP-RIE machine was based.

1. Clean the wafer by sonicating in acetone then IPA for five minutes then dry with N_2

2. Spin coat a layer of Ti Prime at 3000 rpm for 30 seconds then bake for 120 seconds at 110°C - creating an adhesion layer for the photoresist

3. Spin coat a layer of AZ15NXT (450 CPS) photoresist for 30 seconds then bake for 180 seconds at 110°C

4. Expose the wafer through the photomask in mask aligner for 60 seconds with an iLine filter using

5. Bake for 60 seconds at 120°C

6. Develop the photoresist in AZ726 developer for four minutes, rinse with DI water and dry with N_2

7. Hardbake at 150°C for 15 minutes

8. ICP etch the wafer using the following parameters:

    - Etch time: 25 minutes,

- RF Power: 250 W,
- ICP power: 600 W,
- Pressure: 10 mTorr,
- He backing pressure: 10 mTorr,
- Table temperature 7°C,
- Gas flow: 25 SCCM Ar/CHF_3

9. Use REM700 resist remover to remove the resist, rinse with acetone then IPA and dry with N_2

B.4 Catalyst Deposition

Catalyst was deposited on the quartz pillars according to the following recipe

1. Sonicate the catalyst at maximum power for at least 30 minutes
2. Clean the quartz chip with Piranha (3:1 mixture of H_2SO_4 and H_2O_2)
3. Spin coat a layer of PMMA 495 A5 photoresist at 6000 rpm for 30 seconds
4. Bake at 150°C for 3 minutes
5. Cool the catalyst to room temperature
6. Deposit $\sim$ 20 uL of catalyst on top of the quartz chip then dry in air for 10 minutes
7. Dry out remaining catalyst using N_2
8. Bake at 150°C for 10 minutes
9. Gently cool the quartz chip to room temperature using N_2
10. Immerse the quartz chip in a beaker of Acetone warmed to 50°C, sonicate for 1 minute at minium power then transfer to fresh acetone
11. Remove the quartz chip from the acetone and dry with N_2

B.5 Carbon Nanotube Growth

CNTs were grown between pillars using CVD according to the following recipe

1. **Load:** Place the quartz chip into the furnace, ensuring correct alignment.
2. **Line Flush:** Flush the lines to remove residual gases using the following flow rates:
    - Ar: 2000 sccm
    - H_2: 1000 sccm
    - CH_4: 1000 sccm
3. **Warm-Up:** Gradually increase the furnace temperature from room temperature ($\sim 25°C$) to 950°C over 45 minutes. Use:
    - Ar: 200 sccm
4. **Reduction:** Maintain the temperature at 950°C and flow:
    - Ar: 145 sccm
    - H_2: 25 sccm
    - Duration: 10 minutes
5. **Growth:** Introduce methane to initiate CNT growth:
    - H_2: 800 sccm
    - CH_4: 220 sccm
    - Duration: 1 hour
6. **Cool Down:** Cool the system from 950°C to room temperature while maintaining:
    - Ar: 200 sccm

C

Lever Arm Derivation

In Section 4.3.2 the lever arm α of a QD was related to the slopes of the Coulomb diamonds via the expression

$$\alpha = \frac{m_1 m_2}{m_1 - m_2}, \tag{C.1}$$

where m_1 and m_2 are the slopes of the Coulomb diamonds as shown in Figures 4.10 and 5.7 of the main text. Here we give a derivation of Eq. C.1. In Section 3.1.2 we saw that the electrochemical potential μ of a QD is given by

$$\mu(N) = E_C\,(2N+1) - eV_{\text{ext}} + E_N, \tag{C.2}$$

where

$$V_{\text{ext}} = (C_S V_S + C_D V_D + C_G V_G)/C. \tag{C.3}$$

From Eq. C.1 we see that, for fixed N a change in the gate voltage V_G results in a change in $\mu(N)$ given by

$$\Delta\mu = -e\alpha\Delta V_G. \tag{C.4}$$

where $\alpha = \frac{C_G}{C}$. The slopes m_1 and m_2 are given by [49]

$$m_1 = -\frac{C_G}{C - C_S}, \quad m_2 = \frac{C_G}{C_S}, \tag{C.5}$$

from which we see that

$$\frac{m_1 m_2}{m_1 - m_2} = \frac{C_G}{C}. \tag{C.6}$$

D

Powering an Autonomous Clock with Quantum Electrodynamics

Here we present an overview of a model for an autonomous clock, developed in Ref. [28], consisting of a nanomechanical system driven onto a limit cycle by single electron tunnelling which maps well onto the suspended CNTQD system considered in this work.

As described in Section 2.3, clocks are bipartite systems consisting of a clockwork mechanism and a register. In the model considered here, the clockwork consists of a QD coupled to a simple harmonic oscillator (SHO) with resonant frequency $\omega_0/2\pi$, as well as to source and drain electrodes characterised by chemical potentials $\mu_{L,R}$ and temperatures $T_{L,R}$. Tunnelling in and out of the dot is characterised by tunnelling rates $\Gamma_{L,R}$. The motion of the SHO drives position-dependent current $I(z)$, which generates a sequence of ticks recorded by the register. A schematic of the clock is shown in Fig. D.1. The

This image has been removed the publicly available version of this thesis due to copyright restrictions

Figure D.1: Schematic of the autonomous clock described by the model of Ref. [28]. The clockwork consists of a QD coupled to electrodes whose relative electrochemical potentials μ_L and μ_R can be control by the application of voltage. The QD is coupled to a SHO, which, under appropriate conditions can exhibit self sustained oscillations. The measurement of the resulting oscillating current forms the basis of the clocks register. Figure adapted from Ref. [28]

Hamiltonian for the clockwork is given by a sum of the following terms

$$\begin{aligned}
\hat{H}_S &= \epsilon \hat{b}^\dagger \hat{b}, \\
\hat{H}_B &= \sum_k \left(\Omega_{kL} \hat{c}^\dagger_{kL} \hat{c}_{kL} + \Omega_{kR} \hat{c}^\dagger_{kR} \hat{c}_{kR} \right), \\
\hat{H}_T &= \sum_k \left(\lambda_{kL} \left[\hat{b}^\dagger \hat{c}_{kL} + \hat{c}^\dagger_{kL} \hat{b} \right] + \lambda_{kR} \left[\hat{b}^\dagger \hat{c}_{kR} + \hat{c}^\dagger_{kR} \hat{b} \right] \right), \\
\hat{H}_V &= \frac{\hat{p}^2}{2m} + \frac{m\omega_0^2 \hat{z}^2}{2} - F\hat{n}\hat{z}.
\end{aligned} \tag{D.1}$$

The QD is modelled as a single fermionic level with energy ϵ, represented by the Hamiltonian $\hat{H}_S$, where $\hat{b}$ and $\hat{b}^\dagger$ are the annihilation and creation operators, respectively. The leads, described by $\hat{H}_B$, are modelled as continua of non-interacting fermionic modes with energies $\Omega_{k\alpha}$, where $\alpha = L, R$ denotes the left and right leads. Each mode is associated with an annihilation operator $\hat{c}_{k\alpha}$. Tunnelling between the leads and the QD is captured by the Hamiltonian $\hat{H}_T$, where $\lambda_{k\alpha}$ is the coupling strength for mode k in lead α. The SHO is described by the Hamiltonian $\hat{H}_V$, with momentum $\hat{p}$, position $\hat{z}$, effective mass m, and resonant frequency ω_0. The term $F\hat{n}\hat{z}$ in $\hat{H}_V$ accounts for electromechanical coupling between the oscillator and the QD, where F is the force per unit charge and $\hat{n}$ the excess charge $\hat{n}$ on the dot, defined as $\hat{n} = \hat{b}^\dagger \hat{b} - N_0$. Here, $N_0 = \langle \hat{b}^\dagger \hat{b} \rangle_{F=0}$ represents the average occupation in the absence of the coupling force. This coupling can be physically realized by a nearby gate electrode that applies a static potential, producing a position-dependent force on the oscillator proportional to the charge occupation of the dot. The electronic leads are assumed to be in thermal equilibrium, each characterized by the same inverse temperature β but different chemical potentials, $\mu_L \neq \mu_R$, resulting in a bias V

across the device given by

$$V = \frac{1}{e}(\mu_L - \mu_R), \tag{D.2}$$

where e is the charge of an electron. The mechanical motion of the oscillator is assumed to be slow in comparison with the rate at which electrons tunnel through the QD. This *quasiadiabatic* regime is reached when

$$k_B T/\hbar,\ \Gamma_{\text{tot}} \gg \omega_0,\ g_m, \tag{D.3}$$

For the electromechanical model described in Section 5.2.1, it was sufficient that the condition $\Gamma_{\text{tot}} \gg \omega_0$ be satisfied for the system to operate in the quasiadiabatic regime. The condition for reaching the quasiadiabatic regime described by Eq. D.3 is more restrictive. From the results of Section 5.5.1, we have $k_B T/\hbar = 40$ GHz, $\Gamma_{\text{tot}} = 439$ GHz, $\omega_0 = 1.7$ GHz, and $g_m = 1$ GHz, indicating that this more restrictive condition can be satisfied in a physical device.

In the quasiadiabatic regime, the electronic subsystem relaxes to its local steady state on a timescale much shorter than that of the mechanical motion. As a result, the oscillator experiences an average electrostatic force $F\langle\hat{n}\rangle_z$ that depends on its instantaneous position z. Rapid electron tunnelling events give rise to stochastic charge fluctuations, which both damp the oscillator and contribute a stochastic term to the force felt by the oscillator. Combining these effects, the dynamics of the oscillator are governed by the Langevin equation

$$m\ddot{z} + m\,\gamma(z)\,\dot{z} + m\omega_0^2 z = F\langle\hat{n}\rangle_z + \sqrt{D(z)}\,\xi(t), \tag{D.4}$$

where $\gamma(z)$ and $D(z)$ are position-dependent damping and diffusion coefficients, respectively, and $\xi(t)$ is a zero-mean Gaussian white-noise process. For a detailed derivation of this equation see [29]. Self sustained oscillations arise in the above model when the leads are out of equilibrium with each other and the tunnelling rates $\Gamma_{L,R}$ are energy dependent. The first of these conditions is achieved experimentally through the application of a voltage bias V. The second is a well established property of CNT devices of the sort discussed in this work [75, 116, 122].

When these conditions are satisfied, the model predicts that the damping coefficient $\gamma(z)$ becomes negative for small displacements. As the amplitude of oscillation grows, $\gamma(z)$ increases, eventually becoming positive. This balance between negative and positive damping over the course of a full cycle enables results in the formation of a limit cycle, which manifests as self sustained oscillations.

The resulting oscillating current can be computed using Landauer-Büttiker theory via

$$\langle I \rangle_z = \frac{1}{\pi} \int \mathrm{d}E \, \tau_z(E) \left[f_L(E) - f_R(E) \right], \tag{D.5}$$

where $\langle I \rangle_z$ is the time average current at the position x, $\tau_z(E)$ an energy dependent transmission function and $f_{L,R}(E)$ the fermi functions of the left and right leads.

Bibliography

[1] Paolo Abiuso, Harry JD Miller, Martí Perarnau-Llobet, and Matteo Scandi. Geometric optimisation of quantum thermodynamic processes. *Entropy*, 22(10):1076, 2020.

[2] Christoph Adami. What is information? *Philosophical Transactions of the Royal Society A: Mathematical, Physical and Engineering Sciences*, 374(2063):20150230, 2016.

[3] Kushagra Aggarwal, Alberto Rolandi, Yikai Yang, Joseph Hickie, Daniel Jirovec, Andrea Ballabio, Daniel Chrastina, Giovanni Isella, Mark T Mitchison, Martí Perarnau-Llobet, et al. Rapid optimal work extraction from a quantum-dot information engine. *Physical Review Research*, 7(3):L032017, 2025.

[4] Markus Aspelmeyer, Tobias J Kippenberg, and Florian Marquardt. Cavity optomechanics. *Reviews of Modern Physics*, 86(4):1391–1452, 2014.

[5] Julian Barbour. The nature of time. *arXiv preprint arXiv:0903.3489*, 2009.

[6] Julian Barbour. A history of thermodynamics. *Free PDF download accessed December*, 2020.

[7] Carlo WJ Beenakker. Theory of coulomb-blockade oscillations in the conductance of a quantum dot. *Physical Review B*, 44(4):1646, 1991.

[8] SD Bennett and AA Clerk. Laser-like instabilities in quantum nanoelectromechanical systems. *Physical Review B—Condensed Matter and Materials Physics*, 74(20):201301, 2006.

[9] Avishai Benyamini, Assaf Hamo, S Viola Kusminskiy, Felix von Oppen, and Shahal Ilani. Real-space tailoring of the electron–phonon coupling in ultraclean nanotube mechanical resonators. *Nature Physics*, 10(2):151–156, 2014.

[10] Antoine Bérut, Artak Arakelyan, Artyom Petrosyan, Sergio Ciliberto, Raoul Dillenschneider, and Eric Lutz. Experimental verification of landauer's principle linking information and thermodynamics. *Nature*, 483(7388):187–189, 2012.

[11] Antoine Bérut, Artyom Petrosyan, and Sergio Ciliberto. Detailed jarzynski equality applied to a logically irreversible procedure. *Europhysics Letters*, 103(6):60002, 2013.

[12] Antoine Bérut, Artyom Petrosyan, and Sergio Ciliberto. Information and thermodynamics: experimental verification of landauer's erasure principle. *Journal of Statistical Mechanics: Theory and Experiment*, 2015(6):P06015, 2015.

[13] Michael J Biercuk, Shahal Ilani, Charles M Marcus, and Paul L McEuen. Electrical transport in single-wall carbon nanotubes. *Carbon Nanotubes: Advanced Topics in the Synthesis, Structure, Properties and Applications*, pages 455–493, 2008.

[14] Ya M Blanter, O Usmani, Nazarov, and Yu V. Single-electron tunneling with strong mechanical feedback. *Physical review letters*, 93(13):136802, 2004.

[15] Marc Bockrath, David H Cobden, Paul L McEuen, Nasreen G Chopra, Alex Zettl, Andreas Thess, and Richard E Smalley. Single-electron transport in ropes of carbon nanotubes. *Science*, 275(5308):1922–1925, 1997.

[16] Chase P Broedersz and Pierre Ronceray. Twenty-five years of nanoscale thermodynamics, 2022.

[17] Lawrence D Brown, T Tony Cai, and Anirban DasGupta. Interval estimation for a binomial proportion. *Statistical science*, 16(2):101–133, 2001.

[18] Carlos Bustamante, Jan Liphardt, and Felix Ritort. The nonequilibrium thermodynamics of small systems. *Physics today*, 58(7):43–48, 2005.

[19] Craig Callender. Thermodynamic Asymmetry in Time. In Edward N. Zalta and Uri Nodelman, editors, *The Stanford Encyclopedia of Philosophy*. Metaphysics Research Lab, Stanford University, Fall 2024 edition, 2024.

[20] Jien Cao, Qian Wang, and Hongjie Dai. Electron transport in very clean, as-grown suspended carbon nanotubes. *Nature materials*, 4(10):745–749, 2005.

[21] Jae Hong Choi, Junghyun Lee, Seung Min Moon, Yun-Tae Kim, Hyesung Park, and Chang Young Lee. A low-energy electron beam does not damage single-walled carbon nanotubes and graphene. *The Journal of Physical Chemistry Letters*, 7(22):4739–4743, 2016.

[22] Sergio Ciliberto. Experiments in stochastic thermodynamics: Short history and perspectives. *Physical Review X*, 7(2):021051, 2017.

[23] Aashish A Clerk and Steven Bennett. Quantum nanoelectromechanics with electrons, quasi-particles and cooper pairs: effective bath descriptions and strong feedback effects. *New Journal of Physics*, 7(1):238, 2005.

[24] Coilcraft, Inc. *SPICE Model for Coilcraft 0402HP Chip Inductors*. Coilcraft, Inc., February 2015. Document 158-23, Revised 02/26/15.

[25] Cosmic Microwave Technology, Inc. *CITLF2 Cryogenic SiGe Low Noise Amplifier: Technical Datasheet*. Lawndale, CA, USA, October 2024. Revision 10/31/2024.

[26] Gavin E Crooks. Entropy production fluctuation theorem and the nonequilibrium work relation for free energy differences. *Physical Review E*, 60(3):2721, 1999.

[27] T Cubaynes, LC Contamin, MC Dartiailh, MM Desjardins, Audrey Cottet, MR Delbecq, and T Kontos. Nanoassembly technique of carbon nanotubes for hybrid circuit-qed. *Applied Physics Letters*, 117(11), 2020.

[28] Oisín Culhane, Michael J Kewming, Alessandro Silva, John Goold, and Mark T Mitchison. Powering an autonomous clock with quantum electromechanics. *New Journal of Physics*, 26(2):023047, 2024.

[29] Oisín Culhane, Mark T Mitchison, and John Goold. Extractable work in quantum electromechanics. *Physical Review E*, 106(3):L032104, 2022.

[30] Salambô Dago, Jorge Pereda, Nicolas Barros, Sergio Ciliberto, and Ludovic Bellon. Information and thermodynamics: Fast and precise approach to landauer's bound in an underdamped micromechanical oscillator. *Physical Review Letters*, 126(17):170601, 2021.

[31] Hongjie Dai. Carbon nanotubes: opportunities and challenges. *Surface science*, 500(1-3):218–241, 2002.

[32] Suman Datta, Wriddhi Chakraborty, and Marko Radosavljevic. Toward attojoule switching energy in logic transistors. *Science*, 378(6621):733–740, 2022.

[33] Supriyo Datta. *Quantum transport: atom to transistor.* Cambridge university press, 2005.

[34] Giovanni Diana, G Baris Bagci, and Massimiliano Esposito. Finite-time erasing of information stored in fermionic bits. *Physical Review E—Statistical, Nonlinear, and Soft Matter Physics*, 87(1):012111, 2013.

[35] Raoul Dillenschneider and Eric Lutz. Memory erasure in small systems. *Physical review letters*, 102(21):210601, 2009.

[36] Joe Dunlop, Federico Cerisola, Juliette Monsel, Sofia Sevitz, Jorge Tabanera-Bravo, Jonathan Dexter, Federico Fedele, Natalia Ares, and Janet Anders. Extra cost of erasure due to quantum lifetime broadening. *arXiv preprint arXiv:2410.02546*, 2024.

[37] Nina Emery, Ned Markosian, and Meghan Sullivan. Time. In Edward N. Zalta and Uri Nodelman, editors, *The Stanford Encyclopedia of Philosophy.* Metaphysics Research Lab, Stanford University, Fall 2024 edition, 2024.

[38] Paul Erker, Mark T Mitchison, Ralph Silva, Mischa P Woods, Nicolas Brunner, and Marcus Huber. Autonomous quantum clocks: does thermodynamics limit our ability to measure time? *Physical Review X*, 7(3):031022, 2017.

[39] Denis J Evans and Debra J Searles. Equilibrium microstates which generate second law violating steady states. *Physical Review E*, 50(2):1645, 1994.

[40] Michael R Falvo, Greg J Clary, Russell M Taylor, Vernon Chi, FP Brooks Jr, Sean Washburn, and Richard Superfine. Bending and buckling of carbon nanotubes under large strain. *Nature*, 389(6651):582–584, 1997.

[41] M Field, CG Smith, Michael Pepper, DA Ritchie, JEF Frost, GAC Jones, and DG Hasko. Measurements of coulomb blockade with a noninvasive voltage probe. *Physical Review Letters*, 70(9):1311, 1993.

[42] LEF Foa Torres, CH Lewenkopf, and HM Pastawski. Coherent versus sequential electron tunneling in quantum dots. *Physical review letters*, 91(11):116801, 2003.

[43] Michael P Frank. Introduction to reversible computing: motivation, progress, and challenges. In *Proceedings of the 2nd Conference on Computing Frontiers*, pages 385–390, 2005.

[44] Michael Patrick Frank and Thomas F. Knight Jr. *Reversibility for efficient computing.* PhD Thesis, Massachusetts Institute of Technology, Dept. of Electrical Engineering and . . . , 1999.

[45] Giovanni Gallavotti and Ezechiel Godert David Cohen. Dynamical ensembles in nonequilibrium statistical mechanics. *Physical review letters*, 74(14):2694, 1995.

[46] Geoffrey Grimmett and David Stirzaker. *Probability and random processes.* Oxford university press, 2020.

[47] Udit Gupta, Young Geun Kim, Sylvia Lee, Jordan Tse, Hsien-Hsin S Lee, Gu-Yeon Wei, David Brooks, and Carole-Jean Wu. Chasing carbon: The elusive en-

vironmental footprint of computing. In *2021 IEEE International Symposium on High-Performance Computer Architecture (HPCA)*, pages 854–867. IEEE, 2021.

[48] R Hanson, IT Vink, DP DiVincenzo, LMK Vandersypen, JM Elzerman, LH van Beveren, and LP Kouwenhoven. Determination of the tunnel rates through a few-electron quantum dot. *arXiv preprint cond-mat/0407793*, 2004.

[49] Ronald Hanson, Leo P Kouwenhoven, Jason R Petta, Seigo Tarucha, and Lieven MK Vandersypen. Spins in few-electron quantum dots. *Reviews of modern physics*, 79(4):1217–1265, 2007.

[50] Xin He, Prasanna Pakkiam, Adil A Gangat, Michael J Kewming, Gerard J Milburn, and Arkady Fedorov. Effect of measurement backaction on quantum clock precision studied with a superconducting circuit. *Physical Review Applied*, 20(3):034038, 2023.

[51] Andrea Hofmann, Ville F Maisi, Clemens Rössler, Julien Basset, Tobias Krähenmann, Peter Märki, Thomas Ihn, Klaus Ensslin, Christian Reichl, and Werner Wegscheider. Equilibrium free energy measurement of a confined electron driven out of equilibrium. *Physical Review B*, 93(3):035425, 2016.

[52] Jordan M Horowitz and Todd R Gingrich. Thermodynamic uncertainty relations constrain non-equilibrium fluctuations. *Nature Physics*, 16(1):15–20, 2020.

[53] AK Hüttel, HB Meerwaldt, GA Steele, M Poot, B Witkamp, LP Kouwenhoven, and HSJ van der Zant. Single electron tunnelling through high-q single-wall carbon nanotube nems resonators. *physica status solidi (b)*, 247(11-12):2974–2979, 2010.

[54] Thomas Ihn. *Semiconductor Nanostructures: Quantum states and electronic transport*. OUP Oxford, 2009.

[55] Atike İnce. Growth and characterization of carbon nanotubes over co-mo/mgo catalysts. Master's thesis, Izmir Institute of Technology (Turkey), 2010.

[56] Christopher Jarzynski. Equilibrium free-energy differences from nonequilibrium measurements: A master-equation approach. *Physical Review E*, 56(5):5018, 1997.

[57] Christopher Jarzynski. Nonequilibrium equality for free energy differences. *Physical Review Letters*, 78(14):2690, 1997.

[58] Christopher Jarzynski. Equalities and inequalities: Irreversibility and the second law of thermodynamics at the nanoscale. In *Time: Poincaré Seminar 2010*, pages 145–172. Springer, 2012.

[59] Jianfeng Jiang, Lin Xu, Chenguang Qiu, and Lian-Mao Peng. Ballistic two-dimensional inse transistors. *Nature*, 616(7957):470–475, 2023.

[60] Daniel Jirovec, Andrea Hofmann, Andrea Ballabio, Philipp M Mutter, Giulio Tavani, Marc Botifoll, Alessandro Crippa, Josip Kukucka, Oliver Sagi, Frederico Martins, et al. A singlet-triplet hole spin qubit in planar ge. *Nature materials*, 20(8):1106–1112, 2021.

[61] Yonggun Jun, Momčilo Gavrilov, and John Bechhoefer. High-precision test of landauer's principle in a feedback trap. *Physical review letters*, 113(19):190601, 2014.

[62] K Kalaichelvan et al. Synthesis of carbon nanotubes using fe-mo/al 2 o 3 bimetallic catalyst by cvd method. In *IEEE-International Conference On Advances In Engineering, Science And Management (ICAESM-2012)*, pages 429–433. IEEE, 2012.

[63] Kayaku Advanced Materials, Inc. Lor/pmgi technical data sheet. Technical report, Kayaku Advanced Materials, Inc., April 2024. Revision D.

[64] Charles Kittel and Herbert Kroemer. Thermal physics. *American Journal of Physics*, 39(1):126–127, 1971.

[65] Jing Kong, C Zhou, A Morpurgo, HT Soh, CF Quate, C Marcus, and H Dai. Synthesis, integration, and electrical properties of individual single-walled carbon nanotubes. *Applied Physics A*, 69:305–308, 1999.

[66] Jonne V Koski, Ville F Maisi, Jukka P Pekola, and Dmitri V Averin. Experimental realization of a szilard engine with a single electron. *Proceedings of the National Academy of Sciences*, 111(38):13786–13789, 2014.

[67] Leo P Kouwenhoven, DG Austing, and Seigo Tarucha. Few-electron quantum dots. *Reports on progress in physics*, 64(6):701, 2001.

[68] Leo P Kouwenhoven, Charles M Marcus, Paul L McEuen, Seigo Tarucha, Robert M Westervelt, and Ned S Wingreen. Electron transport in quantum dots. *Mesoscopic electron transport*, pages 105–214, 1997.

[69] Edward A Laird, Ferdinand Kuemmeth, Gary A Steele, Kasper Grove-Rasmussen, Jesper Nygård, Karsten Flensberg, and Leo P Kouwenhoven. Quantum transport in carbon nanotubes. *Reviews of Modern Physics*, 87(3):703–764, 2015.

[70] Emmanuel Lamouroux, Philippe Serp, and Philippe Kalck. Catalytic routes towards single wall carbon nanotubes. *Catalysis reviews*, 49(3):341–405, 2007.

[71] Rolf Landauer. Irreversibility and heat generation in the computing process. *IBM journal of research and development*, 5(3):183–191, 1961.

[72] Rolf Landauer. Information is physical. *Physics Today*, 44(5):23–29, 1991.

[73] Benjamin Lassagne, Yury Tarakanov, Jari Kinaret, Daniel Garcia-Sanchez, and Adrian Bachtold. Coupling mechanics to charge transport in carbon nanotube mechanical resonators. *Science*, 325(5944):1107–1110, 2009.

[74] Nadya Mason, MJ Biercuk, and CM Marcus. Local gate control of a carbon nanotube double quantum dot. *Science*, 303(5658):655–658, 2004.

[75] Harold B Meerwaldt, Giorgi Labadze, Ben H Schneider, Ahmet Taspinar, Ya M Blanter, Herre SJ van der Zant, and Gary A Steele. Probing the charge of a quantum dot with a nanomechanical resonator. *Physical Review B—Condensed Matter and Materials Physics*, 86(11):115454, 2012.

[76] Florian Meier, Yuri Minoguchi, Simon Sundelin, Tony JG Apollaro, Paul Erker, Simone Gasparinetti, and Marcus Huber. Precision is not limited by the second law of thermodynamics. *arXiv preprint arXiv:2407.07948*, 2024.

[77] Florian Meier, Yuri Minoguchi, Simon Sundelin, Tony JG Apollaro, Paul Erker, Simone Gasparinetti, and Marcus Huber. Precision is not limited by the second law of thermodynamics. *Nature Physics*, pages 1–6, 2025.

[78] Denis Melanson, Mohammad Abu Khater, Maxwell Aifer, Kaelan Donatella, Max Hunter Gordon, Thomas Ahle, Gavin Crooks, Antonio J Martinez, Faris Sbahi, and Patrick J Coles. Thermodynamic computing system for ai applications. *arXiv preprint arXiv:2312.04836*, 2023.

[79] GJ Milburn. The thermodynamics of clocks. *Contemporary Physics*, 61(2):69–95, 2020.

[80] Joel Moser, Alexander Eichler, Johannes Güttinger, Mark I Dykman, and Adrian Bachtold. Nanotube mechanical resonators with quality factors of up to 5 million. *Nature nanotechnology*, 9(12):1007–1011, 2014.

[81] Michael Mück and Robert McDermott. Radio-frequency amplifiers based on dc squids. *Superconductor Science and Technology*, 23(9):093001, 2010.

[82] Takashi Nakajima, Yohei Kojima, Yoshihiro Uehara, Akito Noiri, Kenta Takeda, Takashi Kobayashi, and Seigo Tarucha. Real-time feedback control of charge sensing for quantum dot qubits. *Physical Review Applied*, 15(3):L031003, 2021.

[83] Yuli V Nazarov and Yaroslav M Blanter. *Quantum transport: introduction to nanoscience*. Cambridge university press, 2009.

[84] Badr Omrane. *Controlled growth and assembly of single-walled carbon nanotubes for nanoelectronics*. PhD thesis, 2009.

[85] Ji-Yong Park, Sami Rosenblatt, Yuval Yaish, Vera Sazonova, Hande Üstünel, Stephan Braig, TA Arias, Piet W Brouwer, and Paul L McEuen. Electron- phonon

scattering in metallic single-walled carbon nanotubes. *Nano letters*, 4(3):517–520, 2004.

[86] Anna N Pearson, Yelena Guryanova, Paul Erker, Edward A Laird, G Andrew Davidson Briggs, Marcus Huber, and Natalia Ares. Measuring the thermodynamic cost of timekeeping. *Physical Review X*, 11(2):021029, 2021.

[87] Karel Proesmans, Jannik Ehrich, and John Bechhoefer. Finite-time landauer principle. *Physical Review Letters*, 125(10):100602, 2020.

[88] Karel Proesmans, Jannik Ehrich, and John Bechhoefer. Optimal finite-time bit erasure under full control. *Physical Review E*, 102(3):032105, 2020.

[89] Eugenia Pyurbeeva and Jan A Mol. A thermodynamic approach to measuring entropy in a few-electron nanodevice. *Entropy*, 23(6):640, 2021.

[90] Sandra Ranković, Yeong-Cherng Liang, and Renato Renner. Quantum clocks and their synchronisation-the alternate ticks game. *arXiv preprint arXiv:1506.01373*, 2015.

[91] DJ Reilly, CM Marcus, MP Hanson, and AC Gossard. Fast single-charge sensing with a rf quantum point contact. *Applied Physics Letters*, 91(16), 2007.

[92] Alberto Rolandi and Martí Perarnau-Llobet. Finite-time landauer principle beyond weak coupling. *Quantum*, 7:1161, 2023.

[93] O-P Saira, Y Yoon, T Tanttu, Mikko Möttönen, DV Averin, and Jukka P Pekola. Test of the jarzynski and crooks fluctuation relations in an electronic system. *Physical review letters*, 109(18):180601, 2012.

[94] Matteo Scandi and Martí Perarnau-Llobet. Thermodynamic length in open quantum systems. *Quantum*, 3:197, 2019.

[95] Giordano Scappucci, Christoph Kloeffel, Floris A Zwanenburg, Daniel Loss, Maksym Myronov, Jian-Jun Zhang, Silvano De Franceschi, Georgios Katsaros, and

Menno Veldhorst. The germanium quantum information route. *Nature Reviews Materials*, 6(10):926–943, 2021.

[96] RJ Schoelkopf, P Wahlgren, AA Kozhevnikov, P Delsing, and DE Prober. The radio-frequency single-electron transistor (rf-set): A fast and ultrasensitive electrometer. *science*, 280(5367):1238–1242, 1998.

[97] FJ Schupp, F Vigneau, Y Wen, A Mavalankar, J Griffiths, GAC Jones, I Farrer, DA Ritchie, CG Smith, LC Camenzind, et al. Sensitive radiofrequency readout of quantum dots using an ultra-low-noise squid amplifier. *Journal of Applied Physics*, 127(24), 2020.

[98] Emanuel Schwarzhans, Maximilian PE Lock, Paul Erker, Nicolai Friis, and Marcus Huber. Autonomous temporal probability concentration: Clockworks and the second law of thermodynamics. *Physical Review X*, 11(1):011046, 2021.

[99] Udo Seifert. Stochastic thermodynamics, fluctuation theorems and molecular machines. *Reports on progress in physics*, 75(12):126001, 2012.

[100] Ken Sekimoto and Shin-ichi Sasa. Complementarity relation for irreversible process derived from stochastic energetics. *Journal of the Physical Society of Japan*, 66(11):3326–3328, 1997.

[101] Edith M Sevick, Ranganathan Prabhakar, Stephen R Williams, and Debra J Searles. Fluctuation theorems. *Annu. Rev. Phys. Chem.*, 59(1):603–633, 2008.

[102] Claude E Shannon. A mathematical theory of communication. *The Bell system technical journal*, 27(3):379–423, 1948.

[103] Alan D. Sokal. Monte carlo methods in statistical mechanics: Foundations and new algorithms, 1996. Lectures at the Cargèse Summer School on *Functional Integration: Basics and Applications*, September 1996. Updated version of lectures given at the Cours de Troisième Cycle de la Physique en Suisse Romande, Lausanne, June 1989.

[104] Richard E. Spinney and Ian J. Ford. Fluctuation relations: a pedagogical overview, 2012.

[105] Gary A Steele, Andreas K Hüttel, Benoit Witkamp, Menno Poot, Harold B Meerwaldt, Leo P Kouwenhoven, and Herre SJ van der Zant. Strong coupling between single-electron tunneling and nanomechanical motion. *Science*, 325(5944):1103–1107, 2009.

[106] M Ştefănescu, O Ştefănescu, M Stoia, and C Lazau. Thermal decomposition of some metal-organic precursors: Fe 2 o 3 nanoparticles. *Journal of Thermal Analysis and Calorimetry*, 88(1):27–32, 2007.

[107] Steven H Strogatz. *Nonlinear dynamics and chaos: with applications to physics, biology, chemistry, and engineering (studies in nonlinearity)*, volume 1. Westview press, 2001.

[108] Sander J Tans, Michel H Devoret, Hongjie Dai, Andreas Thess, Richard E Smalley, LJ Geerligs, and Cees Dekker. Individual single-wall carbon nanotubes as quantum wires. *Nature*, 386(6624):474–477, 1997.

[109] Joseph M Thijssen and Herre SJ Van der Zant. Charge transport and single-electron effects in nanoscale systems. *physica status solidi (b)*, 245(8):1455–1470, 2008.

[110] Carlos Urgell, Wei Yang, Sergio Lucio De Bonis, Chandan Samanta, Maria José Esplandiu, Quan Dong, Yong Jin, and Adrian Bachtold. Cooling and self-oscillation in a nanotube electromechanical resonator. *Nature Physics*, 16(1):32–37, 2020.

[111] O Usmani, Ya M Blanter, and Yu V Nazarov. Strong feedback and current noise in nanoelectromechanical systems. *Physical Review B—Condensed Matter and Materials Physics*, 75(19):195312, 2007.

[112] Suriyanarayanan Vaikuntanathan and Christopher Jarzynski. Dissipation and lag in irreversible processes. *Europhysics Letters*, 87(6):60005, 2009.

[113] Wilfred G Van der Wiel, Silvano De Franceschi, Jeroen M Elzerman, Toshimasa Fujisawa, Seigo Tarucha, and Leo P Kouwenhoven. Electron transport through double quantum dots. *Reviews of modern physics*, 75(1):1, 2002.

[114] Tan Van Vu and Keiji Saito. Finite-time quantum landauer principle and quantum coherence. *Physical review letters*, 128(1):010602, 2022.

[115] Florian Vigneau, Federico Fedele, Anasua Chatterjee, David Reilly, Ferdinand Kuemmeth, M Fernando Gonzalez-Zalba, Edward Laird, and Natalia Ares. Probing quantum devices with radio-frequency reflectometry. *Applied Physics Reviews*, 10(2), 2023.

[116] Florian Vigneau, Juliette Monsel, Jorge Tabanera, Kushagra Aggarwal, Léa Bresque, Federico Fedele, Federico Cerisola, GAD Briggs, Janet Anders, Juan MR Parrondo, et al. Ultrastrong coupling between electron tunneling and mechanical motion. *Physical Review Research*, 4(4):043168, 2022.

[117] Vivek Wadhia, Florian Meier, Federico Fedele, Ralph Silva, Nuriya Nurgalieva, David L Craig, Daniel Jirovec, Jaime Saez-Mollejo, Andrea Ballabio, Daniel Chrastina, et al. Entropic costs of the quantum-to-classical transition in a microscopic clock. *arXiv preprint arXiv:2502.00096*, 2025.

[118] Jonah Waissman, Maayan Honig, Sharon Pecker, Avishai Benyamini, Assaf Hamo, and Shahal Ilani. Realization of pristine and locally tunable one-dimensional electron systems in carbon nanotubes. *Nature nanotechnology*, 8(8):569–574, 2013.

[119] Sean Wallis. Binomial confidence intervals and contingency tests: mathematical fundamentals and the evaluation of alternative methods. *Journal of quantitative linguistics*, 20(3):178–208, 2013.

[120] Yutian Wen. *Back-action and coherent oscillation in a suspended nanotube resonator*. PhD thesis, University of Oxford, 2020.

[121] Yutian Wen, N Ares, T Pei, GAD Briggs, and Edward Alexander Laird. Measuring carbon nanotube vibrations using a single-electron transistor as a fast linear amplifier. *Applied Physics Letters*, 113(15), 2018.

[122] Yutian Wen, N Ares, FJ Schupp, T Pei, GAD Briggs, and EA Laird. A coherent nanomechanical oscillator driven by single-electron tunnelling. *Nature physics*, 16(1):75–82, 2020.

[123] Mischa P Woods. Autonomous ticking clocks from axiomatic principles. *Quantum*, 5:381, 2021.

[124] Chung Chiang Wu, Chang Hua Liu, and Zhaohui Zhong. One-step direct transfer of pristine single-walled carbon nanotubes for functional nanoelectronics. *Nano letters*, 10(3):1032–1036, 2010.

[125] Qianru Wu, Hao Zhang, Chen Ma, Dong Li, Liantao Xin, Xueting Zhang, Nan Zhao, and Maoshuai He. Sio2-promoted growth of single-walled carbon nanotubes on an alumina supported catalyst. *Carbon*, 176:367–373, 2021.

[126] J Xuereb, P Erker, F Meier, MT Mitchison, and M Huber. The impact of imperfect timekeeping on quantum control, arxiv e-prints. *arXiv preprint arXiv:2301.10767*, 2023.

[127] CH Yang, WH Lim, FA Zwanenburg, and AS Dzurak. Dynamically controlled charge sensing of a few-electron silicon quantum dot. *AIP advances*, 1(4), 2011.

[128] Yi-Zheng Zhen, Dario Egloff, Kavan Modi, and Oscar Dahlsten. Universal bound on energy cost of bit reset in finite time. *Physical Review Letters*, 127(19):190602, 2021.

[129] Xinjian Zhou, Ji-Yong Park, Shaoming Huang, Jie Liu, and Paul L McEuen. Band structure, phonon scattering, and the performance limit of single-walled carbon nanotube transistors. *Physical Review Letters*, 95(14):146805, 2005.